Analysis of the Point Pleasant/Lexington/Trenton Formations: Sulfides, Mineralogy, and Trace Elements as Geochemical Proxies

Graduate Thesis

Presented in partial fulfillment of the requirements for the degree
Master of Science in the graduate school of
The Ohio State University

By

Derek Jordan Foley

Graduate Program in Geological Science

The Ohio State University

2016

Thesis Committee

David Cole, Adviser

Michael Barton

Thomas Darrah

Copyright by

Derek Jordan Foley

Abstract

Petrophysical, mineralogical, and geochemical aspects determine the productivity of a gas producing shale. The Point Pleasant, Lexington, and Trenton Formations in Southeastern Ohio have not been studied extensively in this area. This study attempts to define the mineralogical, petrophysical, and geochemical characters of the Point Pleasant/Lexington/Trenton formations in Eastern Ohio. In addition, how redox states vary with the character of the formations. Particular study of sulfide morphology and sulfur isotopes, principally in pyrite, and how they correlate with $^{34}S/^{32}S$ partitioning is explored along with its relation to redox state. Lastly, sulfur isotope partitioning and organic preservation are compared to evidence of biogenic production and alteration. Carbonate is found to determine rock fabric. Clays and organic content are found to contain the bulk of connected porosity, as the majority of porosity is contained in <100 nm diameter pores. Pyrite morphology and location affects $^{34}S/^{32}S$ partitioning and sulfate reducing bacteria are suspected to play a mediating role in the partitioning. This study concludes the Point Pleasant, Lexington, and Trenton Formations formed in variable redox conditions, with oxygenated bottom waters followed by abrupt reducing, anoxic conditions.

Acknowledgements

Great thanks to Stuart Maier and Gulfport Energy for providing funding and samples for the project. I would like to sincerely thank my advisor, Dr. Dave Cole, for his guidance and mentorship throughout this project. Additionally, I would like to thank Dr. Julie Sheets and Dr. Sue Welch for their assistance in data collection as well as instruction. Special thanks to Edwin Buchwalter for his support in XCT and MICP data collection and the company during countless lunches. Thanks to Dan Ardrey for his assistance in XRF preparation and data collection. My gratitude goes out to all of the SEMCAL team for their collaboration, facilities, and knowledge.

Appreciation goes to my committee members, Dr. Mike Barton and Dr. Tom Darrah, for their helpful insight and feedback. Thank you for challenging me to be a better geologist.

I express my gratitude for everyone in the School of Earth Sciences at Ohio State who has helped me better understand earth science and shaping me into the geologist that I am.

I would like to thank my loving family for their continual support and encouragement. Mom and Dad, I love you dearly and could not have accomplished this without you. To brothers, Justin and Dylan, thank you for always sending me kind words and bringing me back down to Earth when I found myself swamped. Your constant love and inspiration means the world to me.

Lastly, thanks to best friend Jon Lunger for helping me clear my head and pushing me through to the end.

I could not have done it without you, I love you all.

- Derek

Vita

2012…….B.A Geological Science, Ohio State University

Fields of Study

Major Field: Geological Science

Table of Contents

Abstract …….ii

Acknowledgements ……iii

Vita …….……v

Table of Contents ……vi

List of Figures ……ix

1. Introduction …….……1

2. Basin formation and formation deposition …….……5

3. Regional Geology …….……7

4. Characterization and Data Collection …….……9

4.1 Petrophysical assessment – MICP; XCT …….……...……11

4.1.1 Mercury Porosimetry …….……...11

4.1.2 X-ray computed tomography (XCT) …….……...11

4.2 Bulk geochemistry – XRF; TOC …….……...11

4.2.1 X-ray fluorescence (XRF) …….……...11

4.2.2 Total organic carbon (TOC) …….……...12

4.3 Mineralogy and fabric – Light Optical Microscope

SEM; QEMSCAN; Fossils; XRD; SIMS …….……...12

4.3.1 Light Optical Microscopy ……12

4.3.2 Scanning electron microscopy (SEM) ……..……...13

4.3.3 SEM with Quantitative Evaluation of Mineralogy by SCANning Electron Microscope (QEMSCAN) ……13

4.3.4 Fossils ……14

4.3.5 X-ray diffraction (XRD) ……14

4.3.6 Sulfides ……15

4.3.6.1 Sulfur isotopes (SIMS) ……15

5. Methodology ……16

5.1 MICP ……16

5.2 XCT ……17

5.3 XRF ……17

5.4 TOC ……18

5.5 XRD ……19

5.6 Light Optical Microscopy ……20

5.7 SEM ……20

5.7 Secondary ion Mass Spectrometry (SIMS)/Ion Microprobe (S isotopes) ……21

6. Results ……22

6.1 Optical descriptions ……22

6.2 Light and Electron Optical and comparisons ……39

6.3 QEMSCAN ……43

6.4 XRD ……46

6.5 XRF ……48

6.6 SIMS ……50

6.7 MICP ……55

6.8 XCT ……58

6.9 TOC ……59

7. Discussion ……60

7.1 Mineralogy ……60

7.2 SIMS ……64

7.3 Trace elements, XRF, and TOC ……69

7.4 MICP ……73

8. Future work ……76

9. Conclusions ……78

References ……80

Appendix: Additional Figures ……84

List of Figures

Figure 1. Map of Ohio with study area marked (Source: Ohio Geological Survey) 7

Figure 2. Sample list with descriptions 9

Figure 3. Sample locations and logs from Wagner 4 well along with depths and corresponding formations. Green log is gamma ray, Red log is resistivity. Maroon log is density, pink log is neutron porosity. Five samples are in the Pt. Pleasant formation, two are in the Lexington, and one is in the Trenton. 10

Figure 4. 1B 8478.8 thick section showing skeletal carbonate and matrix 22

Figure 5. 1B 8478.8 4X, reflected light. Skeletal carbonate region with clay sized matrix between fossils. Pyrite replacement of carbonate 22

Figure 6. 2B 8481.9 thick section with distinguishable bryozoan fossils 24

Figure 7- 2B 8481.9 40X, reflected light. Various pyrite morphologies in clay sized matrix of clay, quartz, and carbonate 24

Figure 8. 2B 8481.9 4X, reflected light. Bryozoan with pyrite replacing carbonate 25

Figure 9. 8492.4 thick section showing matrix dominated sample and fractures.....26

Figure 10. 8492.4 40X, reflected light showing pyrite in matrix and weathering of sulfides 27

Figure 11. 8492.4 40X, reflected light showing carbonate, pyrite, and clay in matrix. Center white grain is marcasite 27

Figure 12. 8492.4 40X, reflected light. Weathered pyrite grains in matrix 28

Figure 13. 8528.83 thick section showing matrix dominated sample 29

Figure 14. 8528.83 4X and 40X, reflected light showing semi-euhedral pyrite in interpreted fluid conduits.....30

Figure 15. 8B 8549.13 thick section with skeletal carbonate layers and crinoid visible....31

Figure 16. 8B 8549.13 4X, PPL. Crinoid stem and other skeletal carbonate....31

Figure 17. 8B 8549.13 10X, reflected light. Skeletal carbonate layer with framboidal pyrite occupying clay-rich space between fossils....32

Figure 18. 8B 8549.13 4X, reflected light. Bioturbation and skeletal carbonate in matrix....32

Figure 19. 9B 8555.84 thick section with matrix ominated sample with a couple layers of skeletal carbonate....33

Figure 20. 9B 8555.84 4X, reflected light. Skeletal carbonate and pyrite replacing carbonate....33

Figure 21. 9B 8555.84 40X, reflected light. Pyrite replacing carbonate in matrix....34

Figure 22. 9B 8555.84 4X, cross-polarized light. Carbonate healed fracture and mineral inclusion....34

Figure 23. 8585.81 thick section with skeletal carbonate layers....35

Figure 24. 11B 8585.81 40X, reflected. Framboidal pyrite aggregate between fossiliferous carbonate....35

Figure 25. 11B 8585.81 4X, reflected light. Skeletal carbonate and matrix showing change in rock fabric....36

Figure 26. 8605.42 thick section showing matrix dominated sample....36

Figure 27. 8B 8549.13 10X, reflected light. Bryozoan and organic in matrix....37

Figure 28. 8605.42 40X, reflected light. Organic and pyrite in matrix....37

Figure 29. 8605.42 40, 4X reflected light. Carbonate healed fracture with included pyrite, surrounding matrix....38

Figure 30. 8605.42 40, 40X reflected light. Carbonate healed fracture with included pyrite, surrounding matrix....38

Figure 31. Typical rock fabric, defined by increasing and decreasing carbonate content and grain size. 9B 8555.41 4X, reflected light 39

Figure 32. 11B 8585.81 40X reflected light and BSE SEM image. Framboidal pyrite and euhedral pyrite in skeletal carbonate layer 40

Figure 33. 1B 8478.8 BSE SEM image. Phosphatic clay sized grains 41

Figure 34. 1B 8478.8 BSE SEM image, carbonate and pyrite replacing skeletal phosphate 41

Figure 35. 8492.4 SEM BSE image showing fine grained matrix and clay wrap.....42

Figure 36. 8528.8 BSE SEM image, celestite replacing carbonate 42

Figure 37. 8492.2 QEMSCAN, mineral key and percentages 45

Figure 38. 9B 8555.81 QEMSCAN fossiliferous section, mineral key and percentages.....45

Figure 39. Mineral concentrations by depth and lithology 47

Figure 40. Aluminum vs Thorium concentrations with linear regression and coefficient of determination 49

Figure 41. Redox sensitive trace elements normalized to Al, ppm 49

Figure 42. Example of large euhedral pyrite, 8B 8549.13 10X, reflected light 50

Figure 43. Example of framboidal pyrite, 8B 8549.13 10X, reflected light.....50

Figure 44. SIMS data by depth and location, Euhedral pyrite. Yellow = carbonate replacement, Red = in matrix, Orange = weathered, Blue = in organic/clay, Gray = large euhedral grain.....51

Figure 45. Interpreted framboid in carbonate in 8605.12, 40X reflected light 53

Figure 46. SIMS data by depth and location, Framboidal pyrite. Yellow = in carbonate, Red = large aggregate of framboids, Blue = individual framboids in matrix.....53

Figure 47. Cumulative porosity by pore diameter 55

Figure 48. Carbonate content vs porosity 57

Figure 49. Clay content vs porosity 57

Figure 50. XCT of 11B 8585.51, yellow is higher density (carbonate), red is lower density (clays, organics, fracture) 58

Figure 51. 8605.42 4X and 40X, reflected light. Carbonate filled fracture with pyrite replacing carbonate.....61

Figure 52. BSE SEM image of 8528.83 showing celestite replacing carbonate with phosphate and clay in matrix.....64

Figure 53. BSE SEM image of 11B 8585.51 showing framboidal pyrite (white) beween fossiliferous carbonate and along a fracture.....67

Figure 54. V(V+Ni) by depth showing estimated redox conditions at time of deposition.....69

Figure 55. Al (%) to U (ppm) correlation with coefficient of determination 71

Figure 56. Clay concentration vs TOC with coefficient of determination 72

Figure 57. SEM BSE 8492.4 showing clay nanoporosity 73

Figure 58. TOC vs porosity suggesting organics contain a portion of porosity 75

Figure 59. All eight Gulfport thick sections and depths, Leica optical microscope 84

Figure 60- QEMSCAN, Gulfport 1-B, with mineral legend. Noticeable features include bryozoan fossil in bottom right corner (calcite and pyrite), large calcitic mollusk fossils spanning the top half of the field, and quartz/clay/calcite matrix with noticeable 30 micron round pyrite in bottom left corner.....85

Figure 61. 11B Highlighted in yellow is a high density hummocky band that is likely fossiliferous and carbonate in origin, indicating a change in the depositional conditions across this zone 86

Figure 62. 1B showing irregular clay and organic layers (red) and high density minerals (yellow) 86

Figure 63. SEM BSE. Framboidal pyrite in organic, calcite and quartz matrix, Gulfport 1B. 87

Figure 64. Framboidal pyrite in organic matter between fossiliferous carbonate, Gulfport 8B 8549.13, Leica optical microscope, reflected light, 10X and 40X. 88

Figure 65. Raw SIMS data.....89

Figure 66. 1B SIMS spot locations.....92

Figure 67- 8B SIMS spot locations.....94

Figure 68- 8605 SIMS spot locations 95

Figure 69- 2B SIMS spot locations.....96

Figure 70- Raw XRF, TOC, Porosity, and XRD data 99

Figure 71- Mineral concentrations by depth.....100

Figure 72- Raw TOC data.....101

1. Introduction

The Point Pleasant/Lexington/Trenton Formations (PPLT) have received significant attention in the past decade due to enhanced recovery techniques and their significance as economically producing gas shales. Despite this interest there has not been systematic study of the Ohio PPLT mineralogy, geochemistry, and redox conditions during deposition. This study aims to characterize and define mineralogy, trace element geochemistry, and paleodepositional conditions of the PPLT as they relate to hydrocarbon generation. Using samples provided by Gulfport Energy, this study will characterize the mineralogical, structural, and geochemical aspects of the PPLT.

The PPLT, while extensively drilled for hydrocarbons over the past five years, have received less geochemical and mineralogical characterization due to their recent exploration and exploitation compared to the geologically younger and more extensively produced Marcellus shale in Pennsylvania and West Virginia (Wickstrom et. al., 2011). In order for a gas shale to be economical, it must have significant organic content, thermal maturity, low to modest clay content, sufficient connected porosity and a volume that makes drilling economical. A gas shale is its own complete hydrocarbon system: source, reservoir, and trap. As such it must be deposited with sufficient organic content to be able to produce hydrocarbons, undergo high enough thermal maturity to generate

hydrocarbons, and contain sufficient porosity to hold hydrocarbons. It must also contain low to moderate clay content as the clay fraction limits frackability and therefore recovery (Boyer et. al., 2011). To understand the initial conditions of the basin as well as diagenesis post-deposition of a black shale, mineralogy, depositional history, and geochemical proxies are studied. Understanding the evolutionary history of both formations can help determine the viability of a gas shale.

Organic carbon burial and preservation and mineral assemblages in gas shales are determined, in part, by redox states and anoxia/euxinic conditions as well as sedimentological setting of the basin during deposition. Organic material has long been thought to be preserved under anoxic bottom water conditions (Tyson, 1995). Geochemical proxies for redox, detrital input (sedimentation), and biogenic productivity have been used to determine redox states and anoxia/euxinic conditions of gas shales. Redox sensitive elements such as U, V, Co, Cu, Zn, and Ni are used to determine anoxia/euxinia (Algeo and Maynard, 2003). Elements indicative of detrital input such as Al and Th are used as proxies for clay input; for example, strong correlations between Al and other elements such as Th suggest significant terrigenous source for the clay as opposed to being authigenic (Croudace, 2015). In addition, sulfides have been used to determine bottom water conditions of anoxia. Reducing (anoxic) bottom waters favor organic preservation where the organic matter is microbially metabolized. In this process, microbes use sulfate as an electron acceptor, reducing it leading to sulfide formation (Sageman et. al., 2003). This reduction of sulfate to sulfide is controlled by specific microbial communities. The presence of organic matter and the anoxic bottom water conditions contribute to sulfide formation as they increases this metabolic rate

(Glombitza et. al., 2013). Authigenic pyrite framboids may form in the water column during anoxic conditions and after reaching a size of 5 μm, the framboids sink and are buried in sediment (Hawkins and Rimmer, 2001). Their presence in the mudstone fabric can suggest anoxic bottom water conditions or redox after deposition.

Complicated mineralogies and structures within microfabrics of these clay and carbonate-rich mudstones make their study difficult and conclusions of their origins elusive. Mineralogy contributes significantly to frackability as well as connected porosity, thereby influencing recovery factors for gas shales. Redox states, detrital sediment influx, and organic productivity in the water column and sediment during and after burial all contribute to the phase assemblages and their morphologies, along with sediment dynamics, compaction and fluid expulsion. As noted above, microbial communities also contribute to controlling the redox states during burial and diagenesis, leading to modification of the mineralogy and microtextures. The magnitude and timing of sedimentological, depositional and diagenetic conditions are critical for the determination of the viability and productivity of a given gas shale.

The overarching goal of this study is to determine these conditions, with the following questions in mind:

i.) What are the mineralogical, petrophysical, and geochemical characteristics of the Point Pleasant/Lexington/Trenton formations in Eastern Ohio?

ii.) How do redox states in the PPLT and adjacent units correlate with organic preservation and detrital sediment influx? If changes with depth are observed, what factors could be the source of the variations?

iii.) How do sulfide morphology and sulfur isotopes, principally in pyrite, correlate with

$^{34}S/^{32}S$ partitioning? How does sulfide morphology correlate with redox conditions?

iv) What role does biogenic production and alteration have on sulfide mineralogy and organic presence?

In order to answer these questions this project focuses on characterization of petrophysical properties (4.1), bulk geochemistry (4.2), and mineralogy and rock fabric (4.3).

Particular attention is paid to sulfide minerals, such as pyrite, as indicators of redox, fluid flow, microbial metabolization, and ion presence. Pyrite grains representing each morphology at selected depths are studied with ion microprobe to determine $^{34}S/^{32}S$ ratios ($\delta^{34}S$). This ratio indicates whether the sulfides are formed authigenically or microbially, and may be related to location (e.g. in matrix versus in fossiliferous carbonate). Framboidal pyrite is expected to have lower $\delta^{34}S$ than euhedral pyrite due to its microbial origin. Further, in relation to this ratio, the individual sulfide grains' location in the rock fabric can determine relative age of its formation, and as a consequence the existence of fluid migration (or lack thereof) (Judd and Hovland, 2009).

Samples are comprised of two thick section suites, billets for additional thin and thick sections, and eight vertical core plugs (see Appendix for full sample list).

2. Basin formation and formation deposition

During the middle to late Ordovician, 460 Mya, a volcanic mountain island arc subducted under the ancestral North American contentinent (Laurentia), closed the Iapetus ocean and produced a foreland basin. The PPLT are thought to have been deposited in a subbasin of this foreland basin (Roy, et. al. 1993). The basin was bounded by the Trenton platform of carbonates to the north, running from northeastern Ohio towards modern day Lake Ontario in upstate New York. To the south, bounding the subbasin, was the Lexington platform composed of argillaceous carbonates. Sediment from surrounding areas settled into the basin, along with organic matter from the inland sea, to make the shale. Significant carbonate was deposited within the basin along with the organics due to the prevailing greenhouse conditions (Willan, et. al. 2012).

The basin featured low energy waters that limited circulation, allowing for organic-rich sediment to be deposited and preserved (Willan, et. al. 2012). Cycles of reducing conditions and anoxia allowed for the preservation of this organic material, producing the organic-rich shales observed in the PPLT. The thickening of shale sequences upward and decreasing carbonate sequences from the Point Pleasant up through the Utica suggest deepening of ocean waters in the area and subsidence of the Lexington carbonate platform (Patchen, et. al. 2006). The creation of these subbasins was due to the collision of an island arc during the Taconic orogeny, producing a foreland

basin to the south-east and the PPLT subbasin to the north-west, with the subsiding Lexington platform separating the two.

3. Regional geology

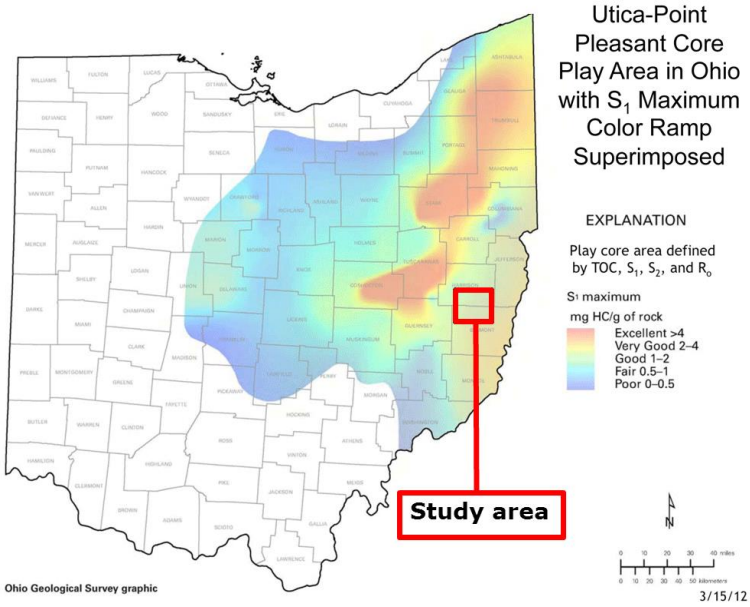

Figure 1- Map of Ohio with study area marked (Source: Ohio Geological Survey)

The Utica Shale depth ranges from less than 2000 feet in central Ohio to more than 14000 feet at its deepest in southwestern Pennsylvania. In the study area (Figure 1), depth to the top of the Utica is roughly 8200 feet and the depth to the top of the Point Pleasant is approximately 8460 feet, and produce natural gas, condensates, and wet gas. It is thickest in southwestern Pennsylvania, with a thickness of over 500 feet, and thins to the west and south. The thickness of the Utica/Point Pleasant formations in the study area is about 250 feet, which is also the average thickness in Ohio. The Lexington Limestone averages 100 feet in Ohio, but is only 40 feet in the study area. The Trenton Limestone is even thinner with a thickness of only 25 feet in the study area. Thicknesses across the Utica/Point Pleasant formations range from 0 to 340 feet (Schumacher, 2013). Maturity decreases up-dip, or

from the southeast to central and northwest Ohio. Due to the decreasing depth and decreasing maturity to the west, wells produce almost exclusively dry gas in southeast Ohio, wet gas and condensates are common in eastern and northern Ohio, and oil in central and northern Ohio. The Utica and Point Pleasant overlie the Lexington and Trenton Limestones, and underlies the coarser Queenston sandstone. The Utica boundary with the Point Pleasant is marked by a significant decrease in carbonate content upsection (Patchen, et. al. 2006).

4. Characterization and data collection

Samples for this study are comprised of two thick section suites, billets for additional thin and thick sections, and eight 1 inch diameter cores (Figures 2 and 3).

ID	Well	Core Depth	Log Depth	Sample descriptions	Formation
1-B	Wagner 4	8478.8	8473	vertical core plug, two thick section suites, billets	Point Pleasant
2-B	Wagner 4	8481.95	8476	vertical core plug, two thick section suites, billets	Point Pleasant
8-B	Wagner 4	8549.13	8541	vertical core plug, two thick section suites, billets	Point Pleasant
9-B	Wagner 4	8555.84	8549	vertical core plug, two thick section suites, billets	Lexington
11-B	Wagner 4	8585.51	8577	vertical core plug, two thick section suites, billets	Lexington
Cuttings	Wagner 4	NA	range	4-15 grams unwashed cuttings per 30 foot interval.	Point Pleasant
1	Wagner #1H	8492.4	8492.2	vertical core plug, two thick section suites, billets	Point Pleasant
2	Wagner #1H	8528.83	8528.83	vertical core plug, two thick section suites, billets	Point Pleasant
3	Wagner #1H	8605.42	8605.42	vertical core plug, two thick section suites, billets	Trenton

Figure 2- Sample list with descriptions

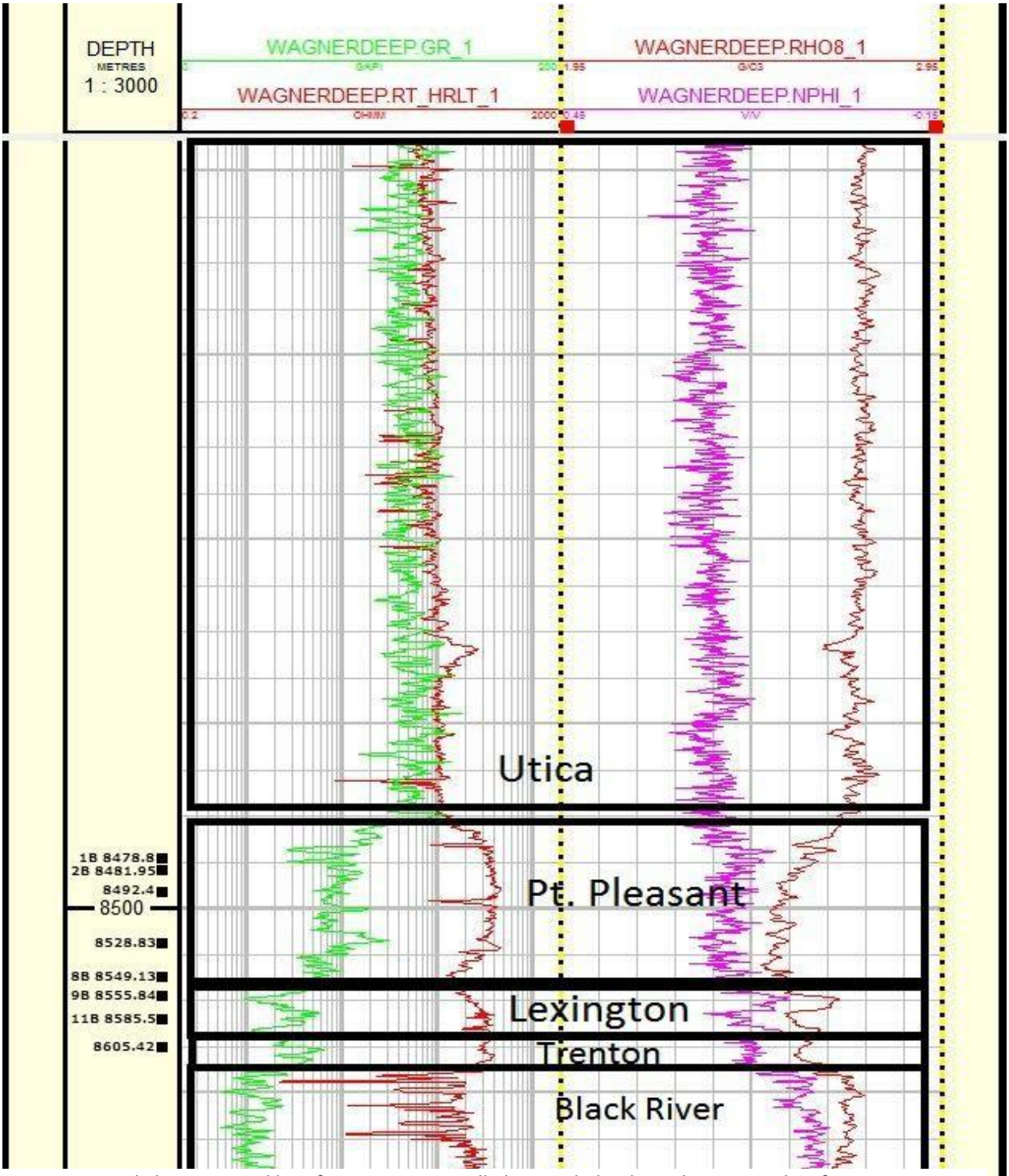

Figure 3- Sample locations and logs from Wagner 4 well along with depths and corresponding formations. Green log is gamma ray, Red log is resistivity. Maroon log is density, pink log is neutron porosity. Five samples are in the Pt. Pleasant formation, two are in the Lexington, and one is in the Trenton.

4.1 Petrophysical assessment – MICP; XCT

4.1.1 Mercury porosimetry

High pressure mercury injection capillary pressure (MICP; up to 60,000 psi) was used to determine total porosity, pore throat size and distribution and pore connectivity. The PPLT contains sequences of argillaceous mudstones with significant carbonate clastics. Within gas-producing black shales, complex micro and nanoscale porosities comprise the majority of total porosity, with narrow pore throats connecting pores. The structure and geometry of these pores greatly influences the migration of fluids, including hydrocarbons, through shales and argillaceous mudstones, affecting recovery factors and frackability.

4.1.2 X-ray computed tomography (XCT)

XCT of the eight core samples will be used to determine macroscopic density contrasts (features greater than about 4 mm), fractures and larger fossils.

4.2 Bulk geochemistry –XRF; TOC

4.2.1 X-ray fluorescence (XRF)

XRF will be used to determine bulk chemical composition of the samples, with special focus on redox-sensitive elements that may be correlated to redox conditions. X-ray fluorescence used high energy X-rays to bombard a sample with radiation which is then absorbed, exciting electrons of the material. The electrons then drop energy levels, re-emit the radiation, hence *fluorescence*. This re-emitted radiation is analyzed to determine elemental concentration as each

element has orbitals of characteristic energy. Trace elements will be normalized to aluminum due to its detrital and immobile nature to determine relative concentrations and therefore redox states. To confirm its detrital origin, Al will used to test for a positive correlations against Sc, Th, or Zr (Pi et. al., 2011). Redox sensitive elements (U, V, Zn) will be used to determine paleoredox sequences within the basin as well as to constrain euxinic versus anoxic conditions. In addition to U, V, and Zn; Co, Cu, and Cr are used to constrain redox conditions (Algeo and Maynard, 2003) during diagenesis

4.2.2 Total organic carbon (TOC)

Defined as the weight percent of organic material in a rock, total organic content (TOC) is measured from core using the Costech elemental analyzer. Using gas chromatography, each gas is measured to determine the weight percentages of nitrogen, carbon, hydrogen, and sulfur to obtain TOC.

4.3 Mineralogy and fabric –Light Optical Microscopy; SEM; QEMSCAN; Fossils; XRD; Sulfides; SIMS

4.3.1 Light Optical Microscopy

Detailed mineralogy and bulk characterization are conducted on the eight thick sections from different depths using both a digital Leica binocular microscope and an Olympus light microscope, also with digital image capture capability. Images from these two microscopes are used to select key regions for the higher resolutions studies based on SEM observations. Fabric, mineralogy, grain sizes, fossils, sulfide morphologies, organic presence, and fractures were

characterized for each thick section. Mineral textural associations are determined based on apparent replacements, proximity, and common sequences observed throughout all of the samples.

4.3.2 Scanning electron microscopy (SEM)

SEM is used to characterize rock samples on a finer scale (down to 100's of nm) and allows for an in-depth assessment of the association of mineralogy, pore features and organic matter. The Everhart-Thornley detector **(**ETD) and Backscattered electron detector (BSE) images of the eight thick sections are acquired through use of a FEI Quanta 250 field emission gun (FEG) SEM.

4.3.3 SEM with Quantitative Evaluation of Mineralogy by SCANning Electron Microscopy (QEMSCAN)

In addition to ETD and BSE image acquisition, geochemical and mineralogical determinations are made using the FEI QEMSCAN® analytical platform (hardware and software). QEMSCAN® generates mineral maps using backscattered electron (BSE) signal intensity in combination with characteristic X-ray emission. The BSE signal yields average atomic number contrast, utilizing gray scale values from quartz, gold, and copper standards. This in combination with 1000 characteristic X-ray counts per point analyzed allows for a comparison with a list of mineral standards acquired by FEI under the same experimental conditions. QEMSCAN can also be used to help determine pore space from non-pore space, yielding information on pore-mineral associations as well as

approximate pore geometry. [Figure 3] X-ray elemental mapping will also be used for smaller fields to help determine mineralogy and elemental distributions.

4.3.4 Fossils

Basic fossil classifications are based on observations using the Leica and Olympus microscopes in reflected, plane-polarized, and cross polarized light modes. Fossil classifications are valuable for determining the paleoclimate and local conditions at the time of the formation of the basin. Sea level depth and energy can be estimated from the fossils present (or absent) as well. The goal of this section is not to cladistically classify the fossilized organisms but to identify the general conditions in which each fossil lived and relate it to the paleoconditions during formation of the PPLT

4.3.5 X-ray diffraction (XRD)

Due to the argillaceous nature of the shales, clay mineralogy and bulk mineral characterization can be incredibly difficult. For an accurate measure of the percent clay composition as well as the mineralogical characterization of the matrix, XRD allows for a more precise chemical analysis of minerals present, down to about 2% accuracy, given that particles in a sample are randomly oriented. This is especially helpful for complex argillaceous mudstones and shales such as the Point Pleasant as it can help distinguish phyllosilicates and other complex mineral assemblages. The quantity of clay minerals present influence the permeability of the shales (Morris and Sheppard, 2013), and low content results in higher frackability (Sondergeld et. al. 2010)

4.3.6 Sulfides

Sulfides, primarily pyrite (FeS_2) are critical to understand the redox and depositional history of shales. Euhedral pyrite can form diagenetically or from reworked framboids, often replacing carbonate. Framboids can form both microbially as well as inorganically which can be determined by Sulfur isotope ratios (see 4.3.7.1 Sulfur isotopes). The presence of microbial pyrite versus euhedral pyrite can explain bottom-water currents, nutrient availability, and redox conditions. For example, larger framboidal pyrite clusters tend to form in oxic/dysoxic conditions and are more readily preserved than smaller (< 5 micron) framboidal pyrite formed in euxinic conditions (Wilkin and Barnes, 1997).

4.3.6.1 Sulfur isotopes (SIMS)

Particular attention was be paid to sulfides, such as pyrite, are indicators of redox, fluid flow, microbial metabolization, and metallic ion presence (e.g. ferrous iron) (Jørgensen, 1977). Using Secondary ion Mass Spectrometry (SIMS or Ion Microprobe), $\delta^{34}S$ was used to determine mechanisms of sulfide formation (authigenic vs microbial) and redox states for individual pyrite grains or grain clusters (Nishizawa et al., 2010; Marin-Carbonne et al., 2014). The power of SIMS measurements is this ability to target single grains or grain cluster that may exhibit varying textural characteristics down to dimensions approaching 20 microns. Measurements were made on a Cameca 7f Geo instrument at the University of Manitoba in Prof. Mostafa Fayek's lab.

5. Methodology

5.1 MICP

Quantitative measurements of connected porosity and pore size were made using Micrometrics Autopore mercury porosimeter. Subsamples of bulk, carbonate, and matrix were cut from core using low speed diamond bit saw and subsequently dried in vacuum oven to remove water. The samples were weighed, then weighed again with the assembled penetrometer. First low pressure injection of mercury stepwise up to 28 psi filled the penetrometer cup with mercury. Upon completion of the low pressure run, the penetrometer filled with mercury is then weight again to determine the weight of the additional mercury, allowing for the calculation of grain density. The loaded penetrometer is then installed into the high pressure port of the porosimeter and pressurized stepwise to 60,000 psi, each step being allowed to equilibrate for a minimum of 500 seconds. The porosimeter measures the amount of mercury intruded by amount of mercury injected into stem using Washburn's equation to determine pore volume distribution by pore size, pore area, and number of pores (Webb, 2001).

$$D = -4\gamma\cos\theta/P$$

with D = pore diameter, P = pressure, θ = wetting angle, γ = surface tension, for spherical pore shapes. This is an oversimplification, especially in the case of these argillaceous shale samples as the phyllosilicates have more slit and triangular pore throats and shapes.

The modified Washburn's Equation becomes:

$$W = -2\gamma\cos\theta/P$$

with W being the diameter between plates.

Due to the very high contact angle of mercury (>140 degrees) mercury is resistant to entering the sample pore system, unlike water which moves freely into confined spaces due to its high-wettability. As pressure increases in the system, the mercury is forced into progressively smaller pores/pore throats, allowing for the measurement of the pore throat diameters intruded at given pressure steps. At the highest pressure of nearly 60000 psi, the dry rock samples, non-wetting mercury, and mercury vapor create a system where mercury can intrude pores as small as 3 nm in diameter.

5.2 XCT

Core plugs from vertical core (approximately 40mm in diameter) were wrapped in fabric to center the cores inside of a 3mm tubular aluminum pre-filter assembly to reduce the appearance of beam-hardening artifacts. Samples were scanned using a CERETOM helical X-Ray Computed Tomography scanner at an accelerating voltage of 120 KeV with a resolution of .625 mm. Utilizing the AVIZO FIRE software suite, three-dimensional datasets were analyzed for density contrasts parallel to bedding, indicating changes in matrix mineralogies as well as identifying carbonate banding, fossiliferous layers, and disruption of parallel layers indicating some degree of bioturbation.

5.3 XRF

First samples were subsampled using a low speed diamond bit saw to acquire bulk

sample, not strictly carbonate or matrix. Then samples were ground to fine uniform powder while wearing gloves and weighed. Samples were split and preserved for XRD analysis. Adsorbed and pore waters were removed by heating ground samples in an oven overnight at 105°C. Samples were weighed again, then heated at 550°C in a muffle furnace for four hours to remove organic carbon. Samples were weighed again, then heated at 950°C for two hours to remove carbonate minerals. Samples were weighed then cooked at 1025°C for one hour to remove mineral bound water then weighed once more. Samples were then weighed into 2.5 gram portions and 10 grams of lithium tetraborate flux was added to create a 4:1 ratio. Beads were then made through fusion in a perlx bead maker and subsequently stored in a desiccator to prevent any further water imbibition.

Samples were run with USGS AVG-2 standard to check accuracy which showed average values within 3% (see Appendix for standard values).

5.4 TOC

Samples were to be ground with mortar and pestle to a fine uniform powder. Next, inorganic carbon, from carbonate and other minerals, was removed through acidification using methodology adapted from Schumacher (2002), using hydrochloric acid to convert the mineral carbonate to CO_2. The process was repeated to remove all inorganic carbon from the samples which are then dried in an oven at 80°C. After being loaded into the analyzer, the samples are flash combusted at temperatures 1700-1800°C, breaking down into nitrogen gas, carbon dioxide, water vapor, and sulfur dioxide. Samples were run with acetanilide standards to obtain weight to area and peak intensity regression. With this regression, peak values from samples can be translated into percent

weight carbon.

5.5 XRD

Samples were first selected as matrix, bulk, or carbonate subsamples of the rock. If necessary, samples were cut from core using a low speed diamond bit saw to ensure precise albeit imperfect selection of lithological type. Three to six grams of each sample is to a uniform powder in a mortar and pestle wearing gloves to avoid introducing contamination.

After grinding to a fine uniform powder, samples are placed into sample holders and into a magazine which is placed in the XRD. The samples were analyzed with a PANalytical X'Pert Pro X-ray diffractometer at the Subsurface Energy Materials Characterization and Analysis Laboratory (SEMCAL), School of Earth Sciences, The Ohio State University. This instrument is equipped with a high speed X-Celerator detector. All runs were at 45 keV voltage and 40 mA tube current, from 4 to 70 degrees with 2-theta step of 0.02 degrees. After run is completed, using PANalytical HighScore Plus background is determined then manually checked, adding or removing peaks as necessary. Peaks in the diffractogram are selected first by the software then checked manually, using a minimum significance of 1.00, a minimum tip width of 0.10, a maximum tip width of 1.00 and a peak base width of 2.00. The method applied used a minimum 2nd derivative. They are then investigated to determine mineralogy us the pattern matching algorithm in HighScore Plus, using the PDF 4+ mineral database. Minerals deemed like or relevant to the samples were selected while less likely or non-relevant minerals were rejected. Pattern lines were checked to ensure the highest intensity

lines and therefore most likely mineral being selected.

Semi-quantitative mineral concentrations (% total mass) were determined by restricting mineral selections to those with reference intensity ratio (RIR) values. RIR are defined as the strongest peak of a sample to the strongest line of a reference phase (in this case, corundum (113) intensity) in a 1:1 mixture. RIR are a scaling factor that can be used to convert intensity of peak intensities into weight percentages. Using these values, the HighScore Plus software can calculate approximate mineral abundaces based on the reference intensity ratios.

5.6 Light Optical Microscopy

Using an Olympus BX53 polarizing light microscope, thick sections were viewed and categorized under plain-polarized light (PPL), cross polarized light (XPL), and reflected light. 4x, 10x, and 40x objective lenses were utilized. Using the Olympus software and reflective light attachment mineral measurements were made. Thick section images were taken using a Leica xxx and stitched together using Adobe Photoshop software's autostitch function.

5.7 SEM

All thick sections were carbon-coated to reduce charging. The methodology used for the carbon coat is to place sample in vacuum, then run a current for 30 seconds at 3 kEV through a carbon thread to evacuate the sample and chamber then 10-15 seconds at 5-5.5 kEV to achieve a sufficient carbon coat. Sample were handled with gloves to prevent contamination and placed in a FEI Quanta 250 FEG SEM at high vacuum. All

samples were analyzed and imaged using 15 KeV voltage, with a spot size 4 to 5 microns. The Everhart-Thornley Detector (ETD) was used primarily for texture and morphology. The back-scattered electron detector (BSE) was used primarily for density contrasts and chemical data. All chemical data were taken at 13 mm working distance, the preferred working distance for the Bruker software and chemical data. Fine detailed imaging was taken at a working distance of 10 mm. The FEI Quanta 250 SEM is equipped with QEMSCAN mineral mapping software which can be used for mineral identification and create images of pore/grain boundary microtextures.

5.8 Secondary ion Mass Spectrometry (SIMS)/Ion Microprobe (S isotope)

Sulfides were selected on polished thick sections using reflected light microscopy to create a map for the microprobe. The analysis was completed on a Cameca 7f Geo instrument at the University of Manitoba in Prof. Mostafa Fayek's lab. The spot-to-spot reproducibility on the pyrite standard (Balmat pyrite, 15.1‰ relative to Canyon Diablo troilite) was 0.3‰ to 0.4‰. A wide range of sulfide morphologies, sizes, and locations were selected to better constrain the variables' effects on δ^{34}S values.

6. Results

6.1 Optical descriptions

GP 1-B 8478.8 (Figure 4)

GP 1-B exhibits heavily fossilized carbonate rich laminae with thin sequences of clay-sized matrix. Fossils include bryozoans (Figure 5), mollusk, brachiopods, trilobite fragments, and crinoids. Fractures are present and are parallel to bedding. Numerous morphologies of sulfides are present. Euhedral sulfide replacing carbonate and individual crystals range in size from micron to larger than 130 microns are present, with cubic and carbonate replacement being most common (Figure 5). Some areas have significant framboidal pyrite, often near organic-rich or areas with obvious pore space suggesting formation

Figure 4- 1B 8478.8 thick section showing skeletal carbonate and matrix

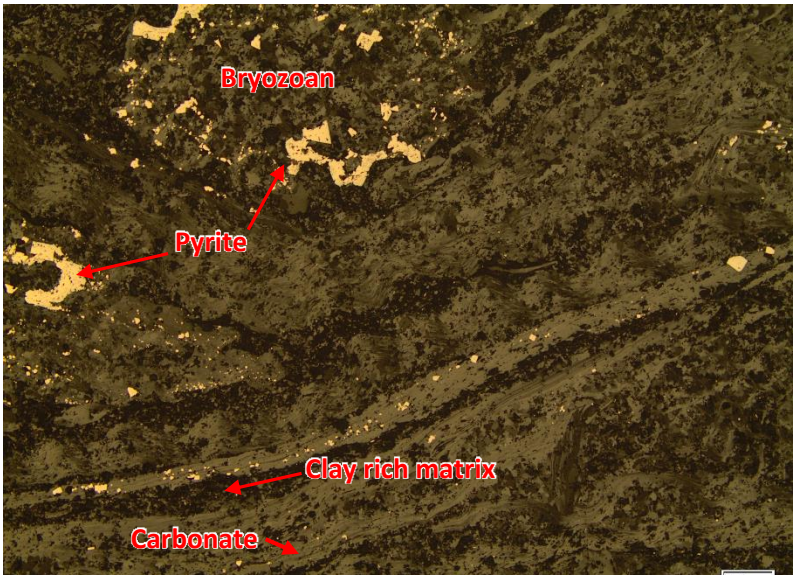

Figure 5- 1B 8478.8 4X, reflected light. Skeletal carbonate region with clay sized matrix between fossils. Pyrite replacement of carbonate.

through bacterial sulfate reduction. One interesting morphology presented is “snowball” pyrite, a circular 27-micron diameter pyrite ball.

GP 2-B 8481.9 (Figure 6)

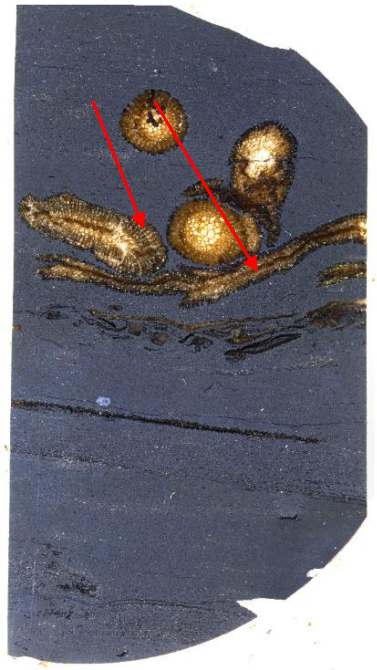

Figure 6- 2B 8481.9 thick section with distinguishable bryozoan fossils

GP 2-B is mainly fine grained argillaceous clay, quartz, and carbonate matrix with a few areas of increased grain size and carbonate presence. There are abundant bryozoan fossils, each measuring >600 microns, with numerous bryozoan, bivalve, and trilobite fragments in the same sequence (Figure 8). Bryozoans and other carbonates are heavily pyritized, with sulfides replacing carbonate. Framboidal and circular morphologies of pyrite are also present (Figure 7). Fractures occur parallel to bedding, often along skeletal carbonate or highly carbonate-rich boundaries.

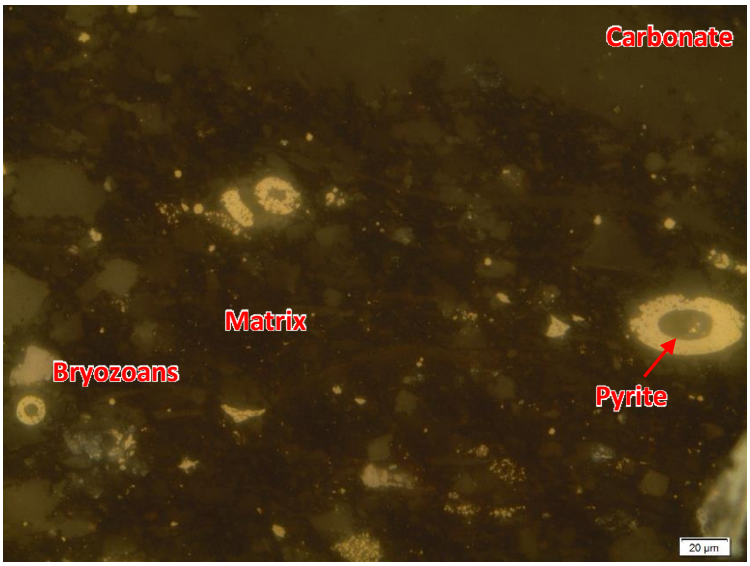

Figure 7- 2B 8481.9 40X, reflected light. Various pyrite morphologies in clay sized matrix of clay, quartz, and carbonate.

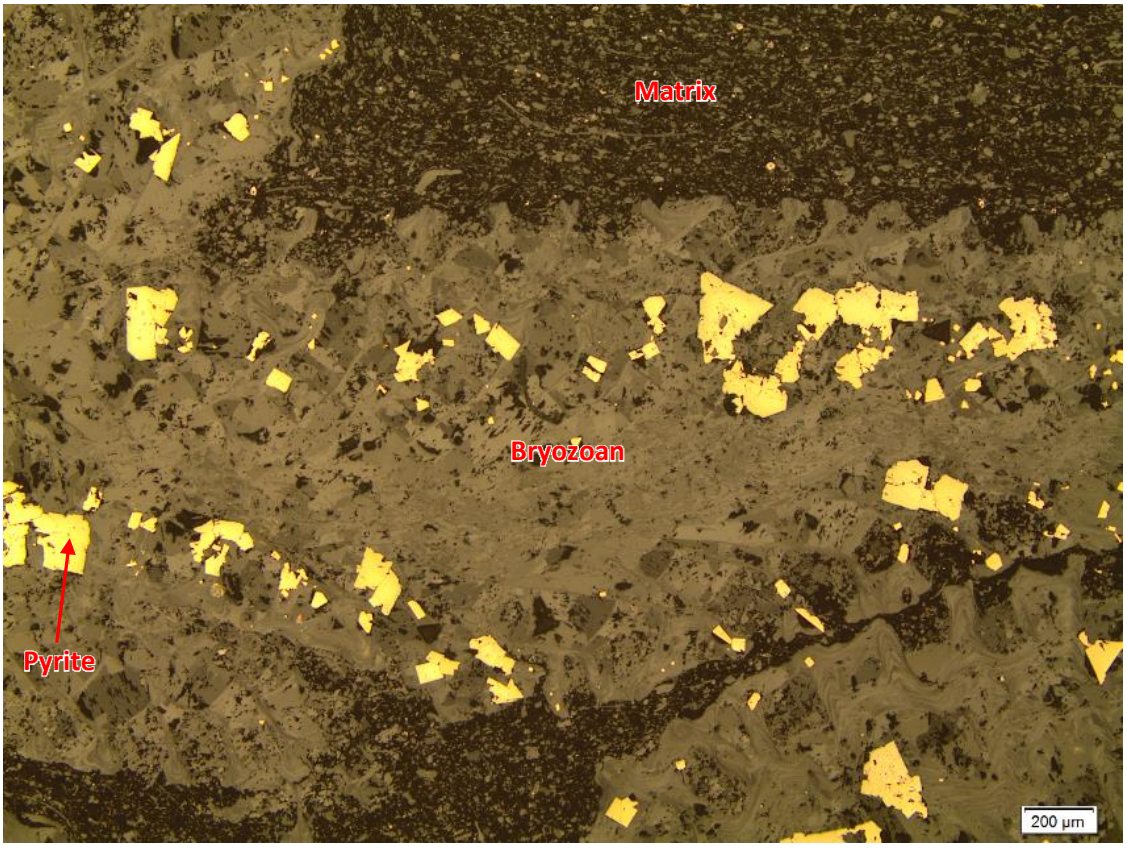

Figure 8- 2B 8481.9 4X, reflected light. Bryozoan with pyrite replacing carbonate.

GP 8492.4 (Figure 9)

Figure 9- 8492.4 thick section showing matrix dominated sample and fractures.

GP 8492.4 contains a few fractures of widths up to 15 microns oriented parallel to bedding. Pyrite appears as circlular crystals (tasmanite cysts or gas bubble or Liesegang rings) caused possibly by bacterial sulfate reduction, as well as euhedral (cubic and carbonate replacement) and framboidal morphologies (Figure 10). The matrix is comprised of fine grained, quartz, phosphates, clay, and carbonate with an average grain size less than 4 microns. There is some marcasite replacing carbonate mixed in with the pyrite suggesting possible pyrite weathering and lower pH (Figures 11 and 12). Marcasite can be identified by its orthorhombic crystal structure and chalk-white color. The entire slide is clay rich with little to no carbonate-dominated zones, unlike other depths.

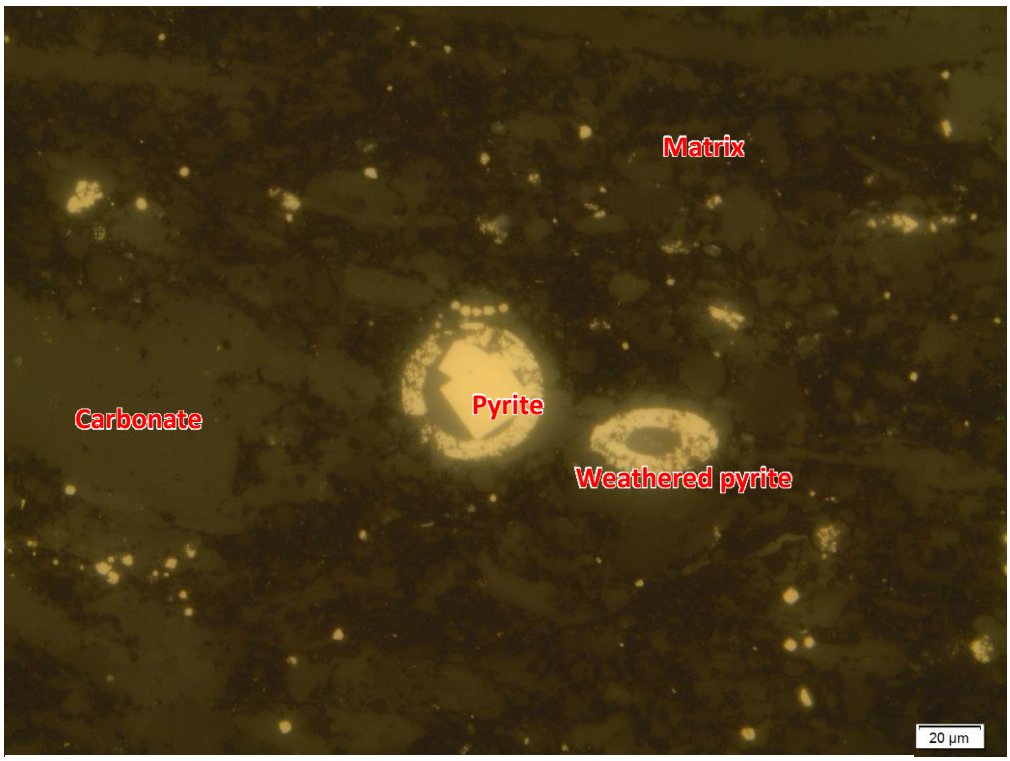

Figure 10- 8492.4 40X, reflected light showing pyrite in matrix and weathering of sulfides.

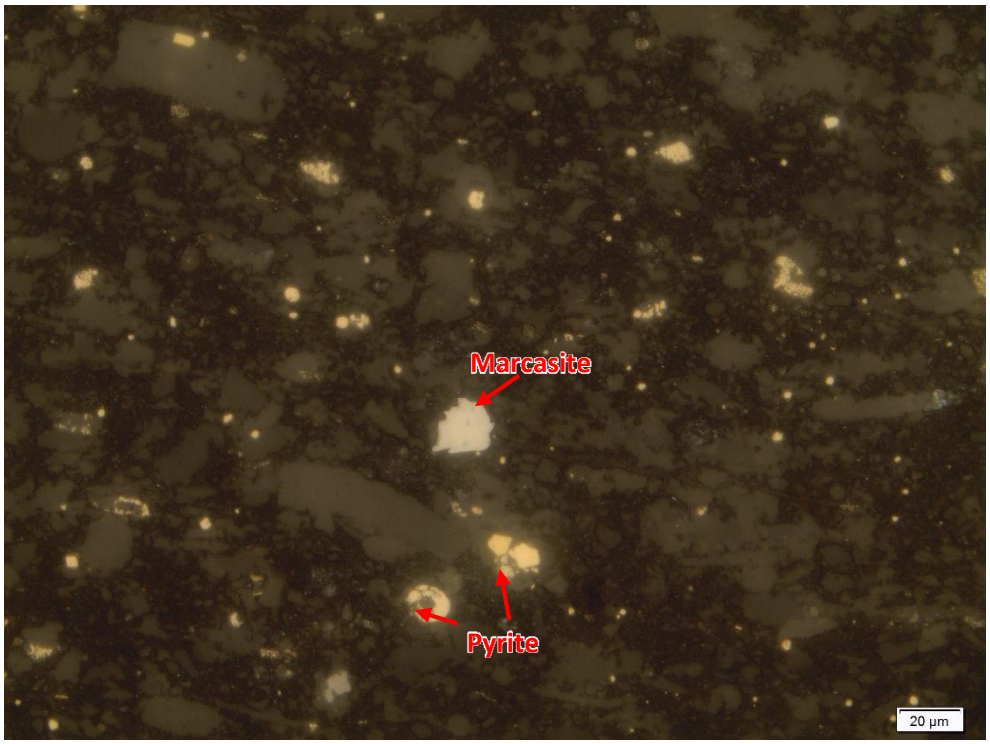

Figure 11- 8492.4 40X, reflected light showing carbonate, pyrite, and clay in matrix. Center white grain is marcasite.

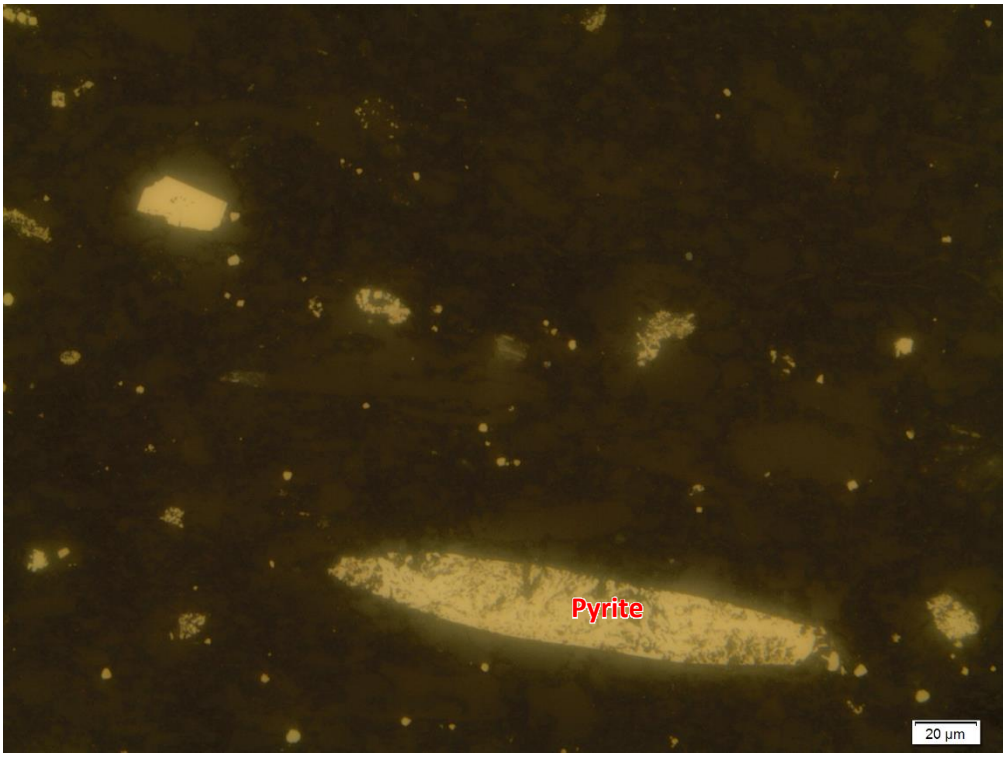

Figure 12- 8492.4 40X, reflected light. Weathered pyrite grains in matrix.

GP 8528.83 (Figure 13)

Matrix is fine grained clay, carbonate, quartz, and pyrite. Matrix contains a few fractures that run parallel to bedding. Fossils are present in the form of bivalves, brachiopods, crinoids, and trilobite fragments. Carbonate is pyritized frequently, with euhedral pyrite replacing carbonate. Some areas are heavily pyritized while areas less than 1 mm away are not. Numerous areas have semi-euhedral pyrite crystals that appear in clay and organic rich sections. These could be relict framboids that were formed into euhedral pyrite through dissolution and recrystallation (Figure 14) (Krajewski, 2013).

Figure 13- 8528.83 thick section showing matrix dominated sample.,

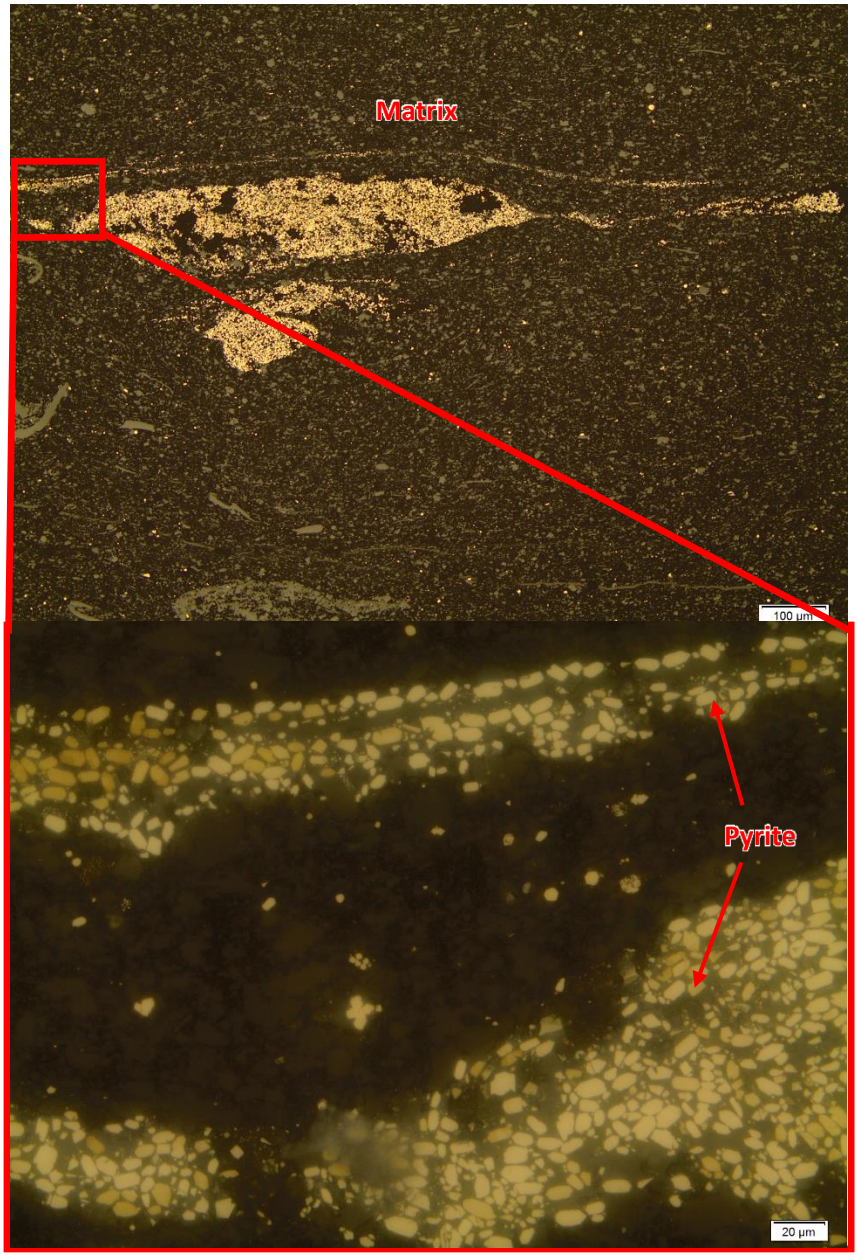

Figure 14- 8528.83 4X and 40X, reflected light showing semi-euhedral pyrite in interpreted fluid conduits.

GP 8-B 8549.13 (Figure 15)

GP 8-B is carbonate-rich argillaceous mudstone with sequences of fine grained to coarse grained matrix. The coarse grained sequences contain abundant skeletal carbonate from brachiopods, mollusks, bivalves, crinoids, and trilobite skeletal fragments (Figures 16 and 17). Significant bed-form disruption due to bioturbidation occur in these fossiliferous sections. Carbonate veins and fractures occur parallel to bedding (Figure 18). Sulfides are present in the form of euhedral replaced carbonate and framboids. GP 8-B contains significant framboidal pyrite and less euhedral pyrite in skeletal carbonate (Figure 17).

Figure 15- 8B 8549.13 thick section with skeletal carbonate layers and crinoid visible.

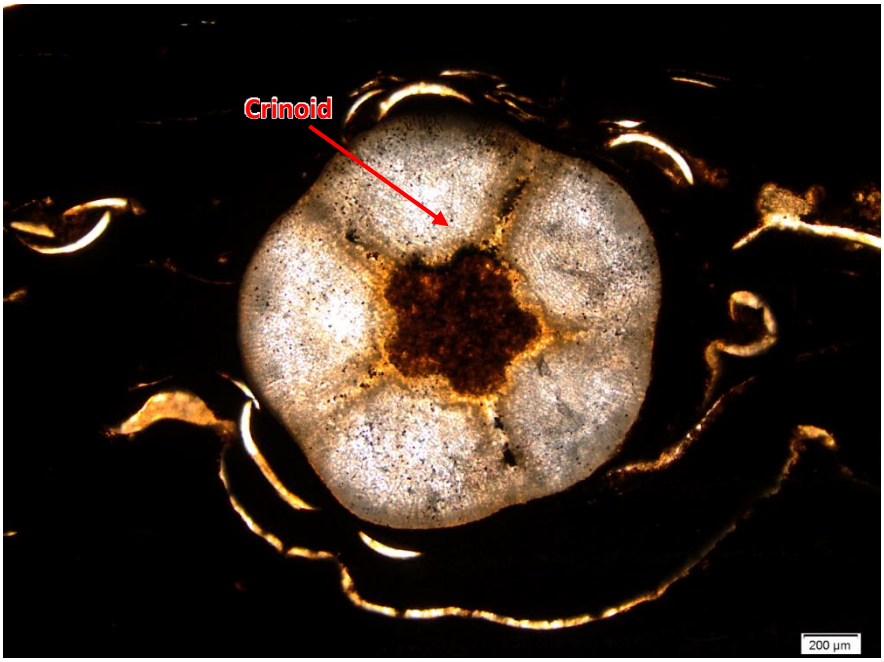

Figure 16- 8B 8549.13 4X, PPL. Crinoid stem and other skeletal carbonate.

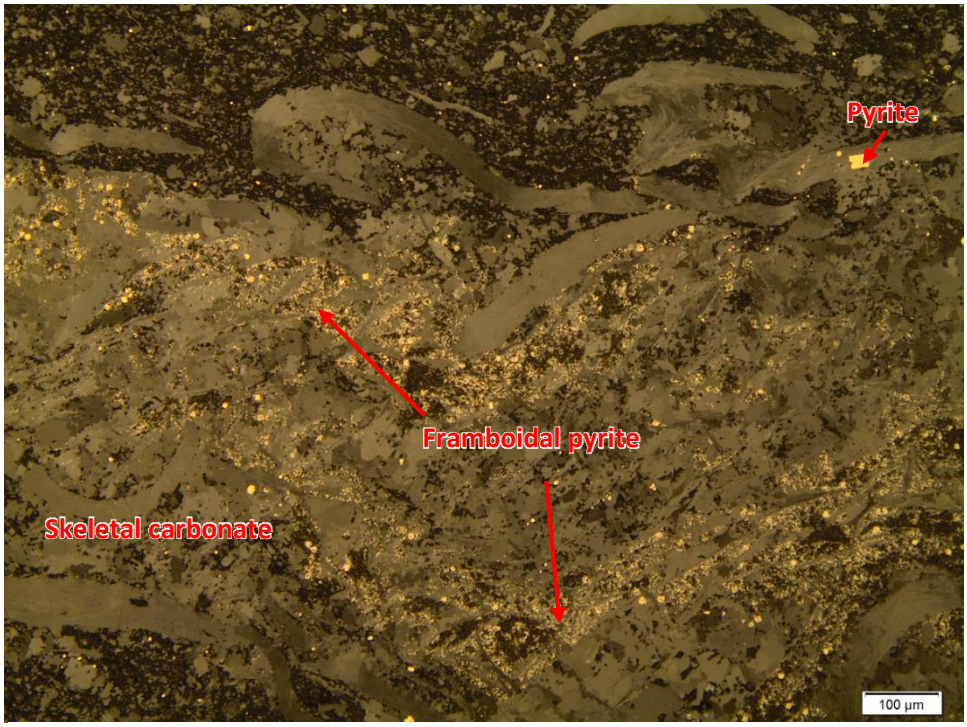

Figure 17- 8B 8549.13 10X, reflected light. Skeletal carbonate layer with framboidal pyrite occupying clay-rich space between fossils.

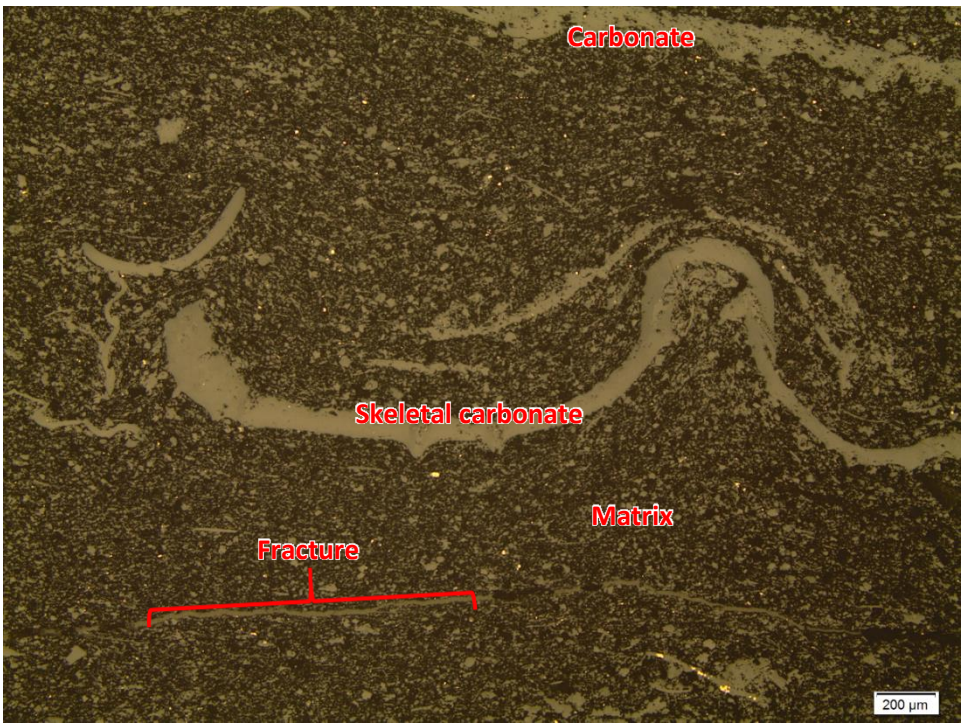

Figure 18- 8B 8549.13 4X, reflected light. Bioturbation and skeletal carbonate in matrix

GP 9-B 8555.84 (Figure 19)

GP 9-B is mostly comprised of clay, carbonate, and sulfide. Some fabric is visible within matrix due to changes in carbonate concentration and grain size varying from clay to silt. Some large-grained carbonate-rich layers are between 350-500 microns thick (Figure 20). Matrix-bound carbonate grains range from 25-50 microns. Euhedral and framboidal pyrite are present. Euhedral sulfides ranging from 5-40 microns (Figure 21). Some fractures are infilled with carbonate while others are open, noticeable in XPL and the inclusion of minerals within the fracture (Figure 22).

Figure 19- 9B 8555.84 thick section with matrix ominated sample with a couple layers of skeletal carbonate.

Skeletal material from bivalves, brachiopods, and crinoids, and pellets are also present.

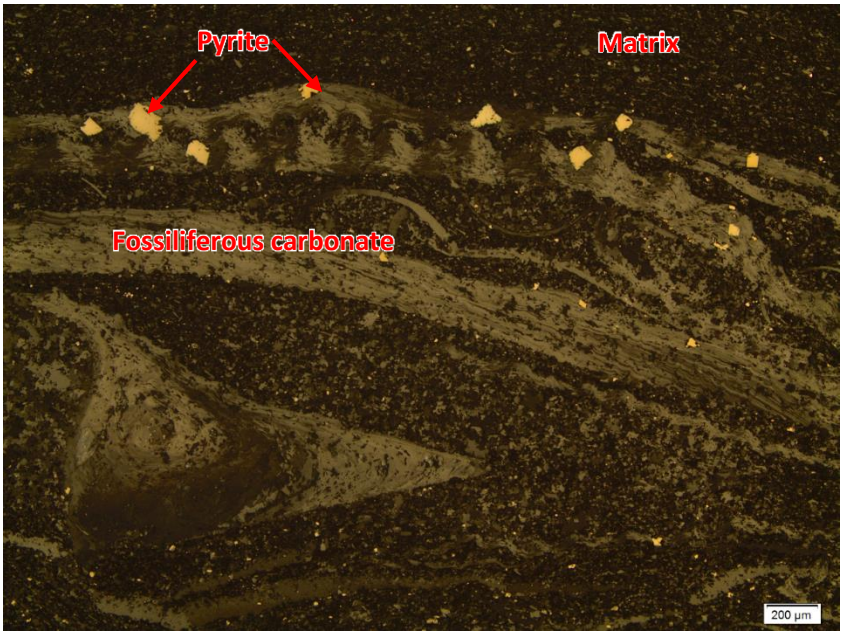

Figure 20- 9B 8555.84 4X, reflected light. Skeletal carbonate and pyrite replacing carbonate.

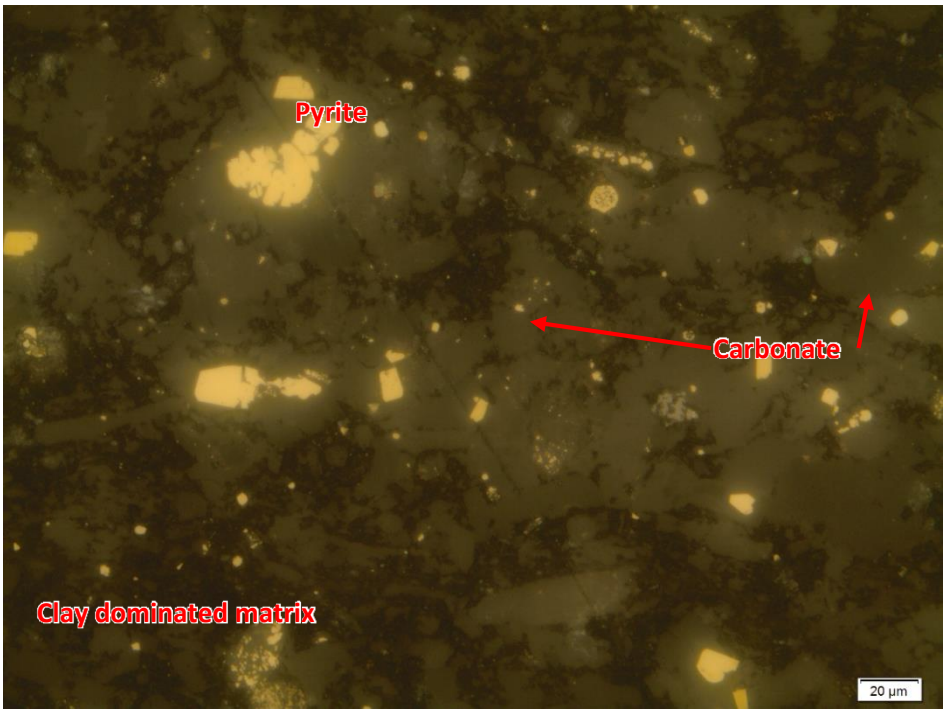

Figure 21- 9B 8555.84 40X, reflected light. Pyrite replacing carbonate in matrix.

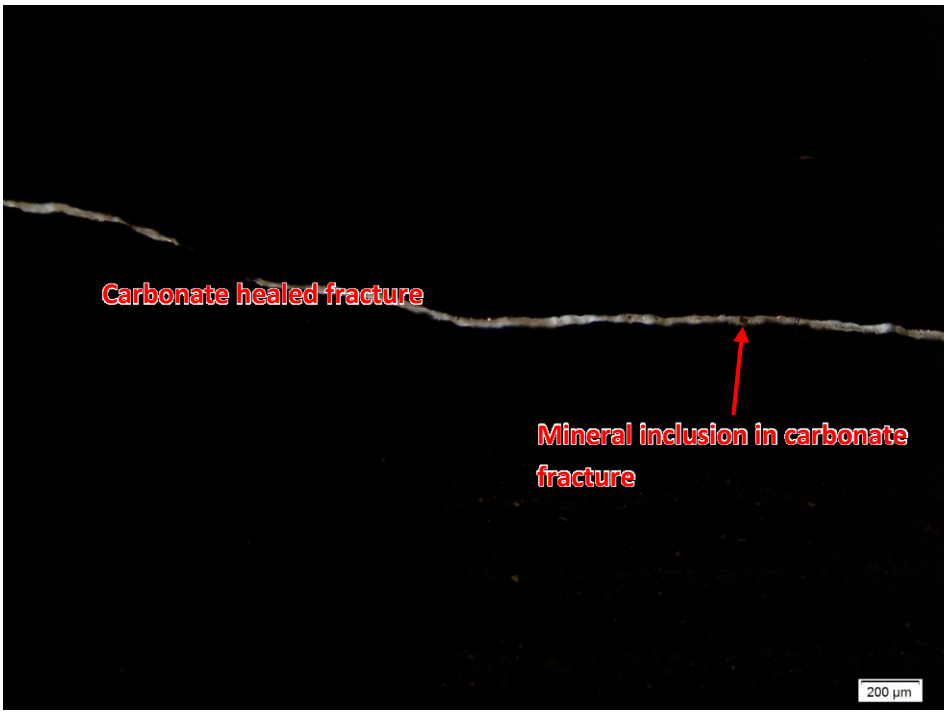

Figure 22- 9B 8555.84 4X, cross-polarized light. Carbonate healed fracture and mineral inclusion.

GP 11-B 8585.81 (Figure 23)

GP 11-B contains carbonate sequences with abundant bioturbidation and fossils followed by clay rich argillaceous regions with much less abundant carbonates (Figure 25). Fractures run parallel to bedding, ranging from 15 microns to 400 microns with some sealed with carbonate. Numerous iron sulfides are present, primarily consisting of pyrite replacing carbonate but also in the form of framboids. Some matrix regions between fossiliferous carbonate contain abundant clusters of framboids hundreds of microns long (Figure 24). Although it is rare, marcasite was observed replacing carbonate indicated by its chalk-white appearance and orthorhombic crystal habit.

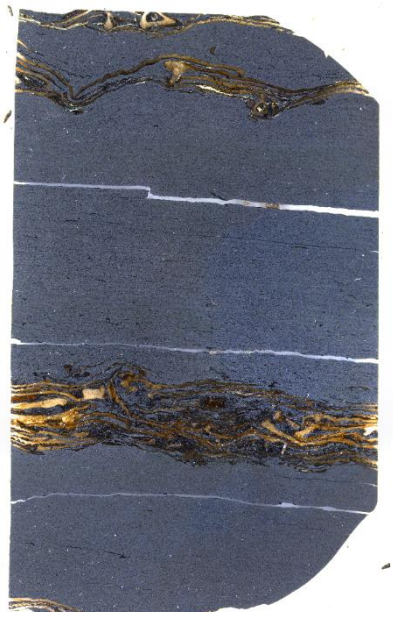

Figure 23- 8585.81 thick section with skeletal carbonate layers.

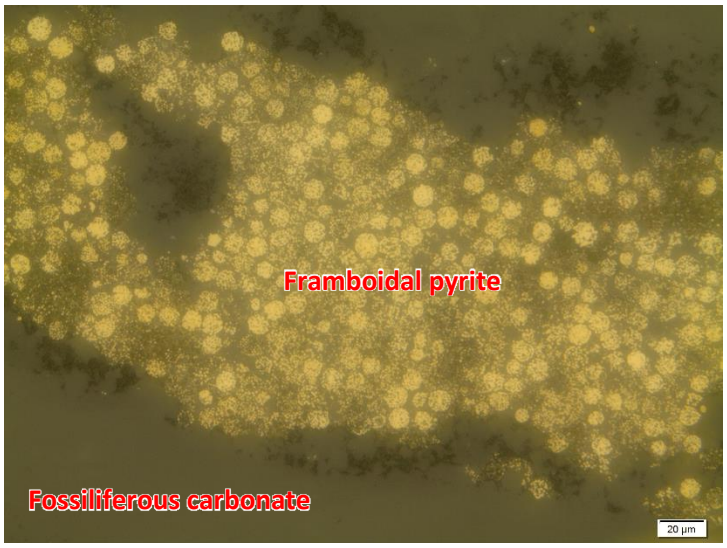

Figure 24- 11B 8585.81 40X, reflected. Framboidal pyrite aggregate between fossiliferous carbonate.

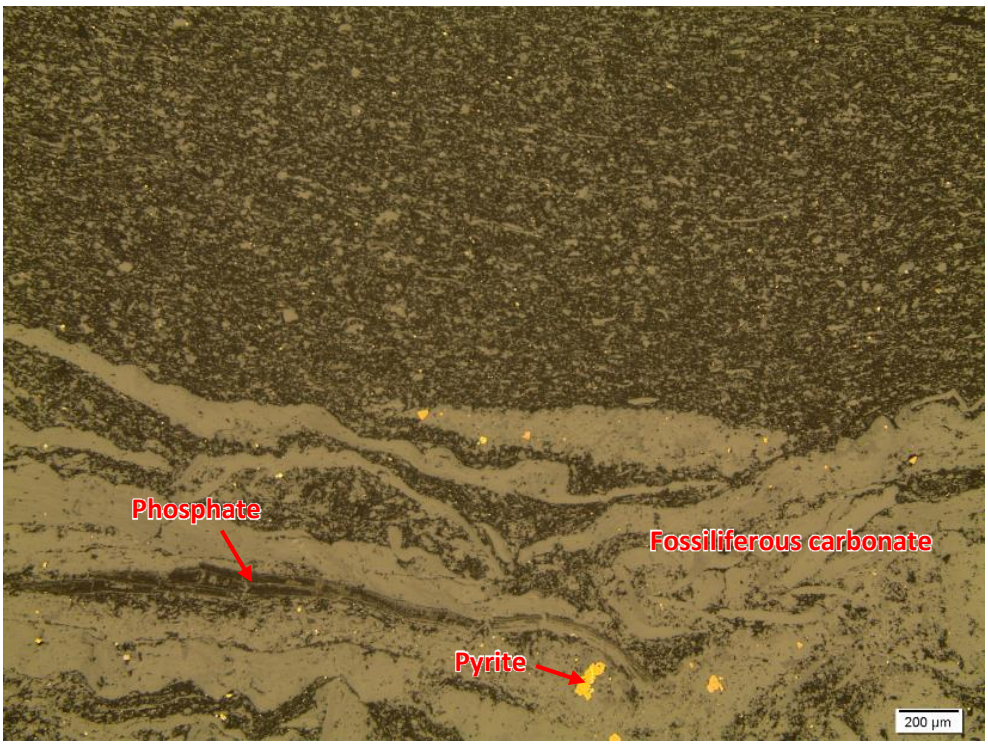

Figure 25- 11B 8585.81 4X, reflected light. Skeletal carbonate and matrix showing change in rock fabric.

GP 8605.42 (Figure 26)

GP 8605.42 consists of organic rich argillaceous matrix of clay, quartz, and carbonates with a few zones of bioturbidation and fossils consisting of bryozoans, bivalves, brachiopods, crinoids, and pellets (Figure 27). GP 8605.42 contains significantly more organic matter than other samples as seen by the 5 to 80 micron wide lenses of kerogen (Figures 27 and 28). There are some fractures, a few carbonate infilled (Figures 29 and 30). Sulfides are present in the form of euhedral grains and

Figure 26- 8605.42 thick section showing matrix dominated sample.

framboids. The framboids are often found adjacent to clay and/or organic matter.

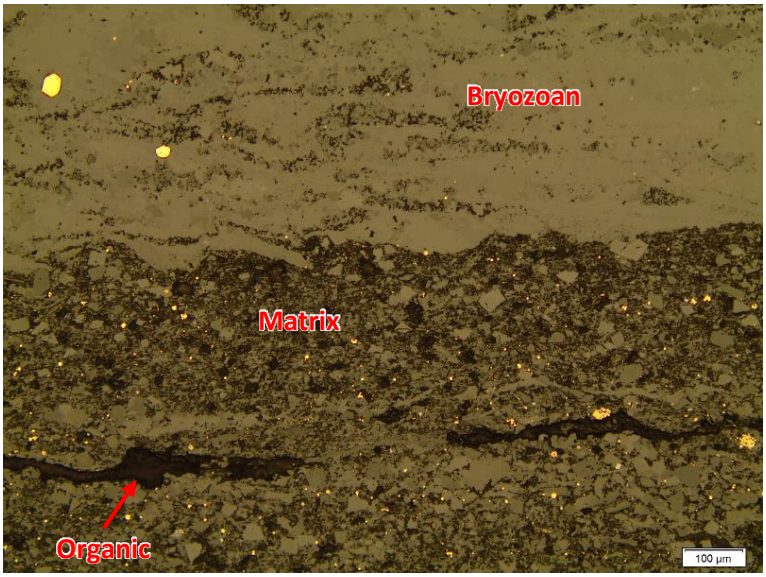

Figure 27- 8B 8549.13 10X, reflected light. Bryozoan and organic in matrix.

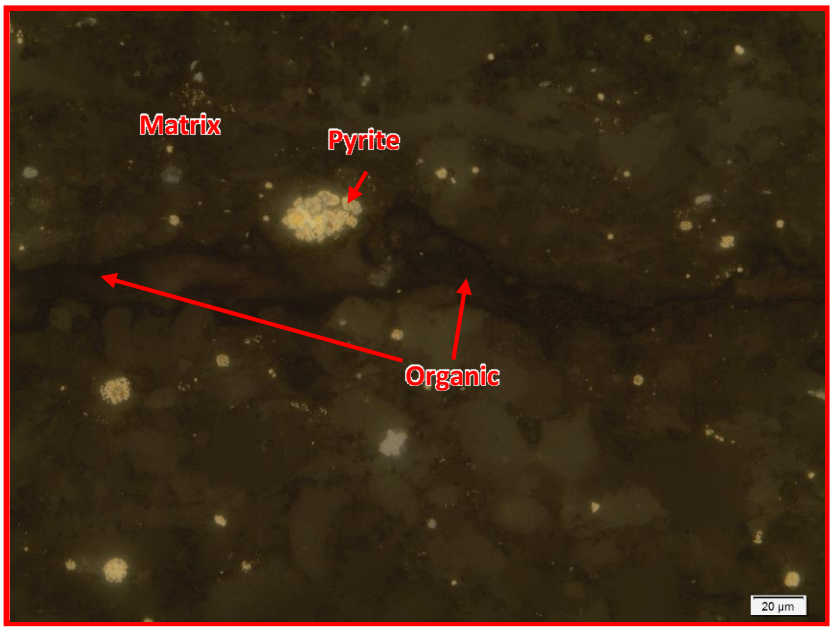

Figure 28- 8605.42 40X, reflected light. Organic and pyrite in matrix.

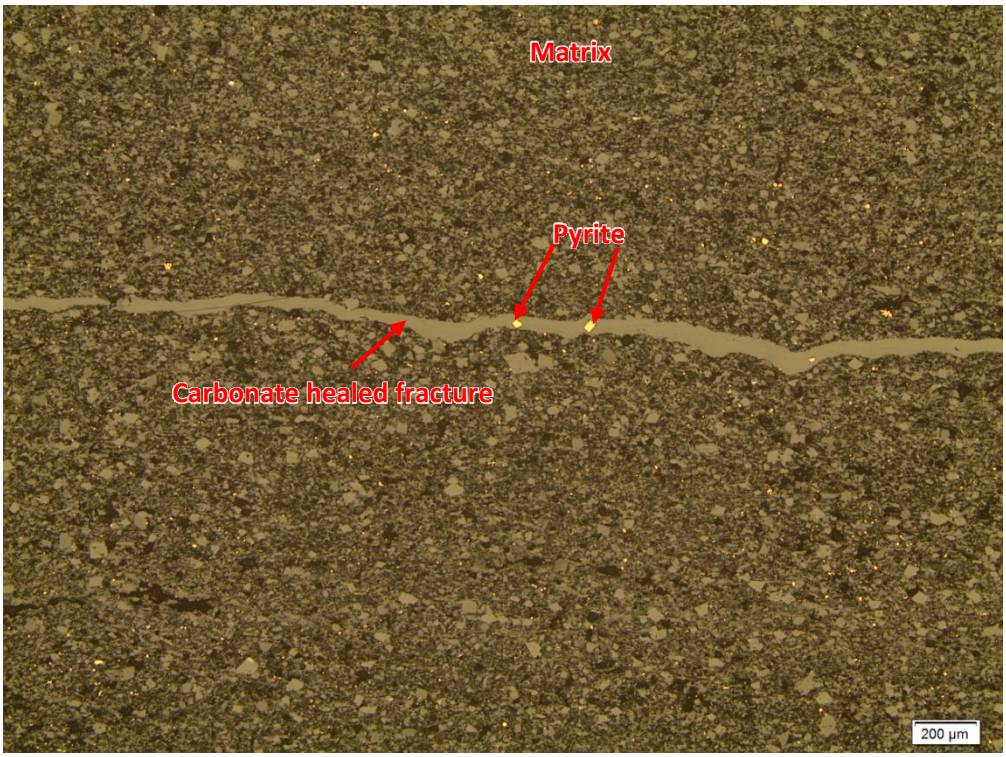

Figure 29- 8605.42 40, 4X reflected light. Carbonate healed fracture with included pyrite, surrounding matrix

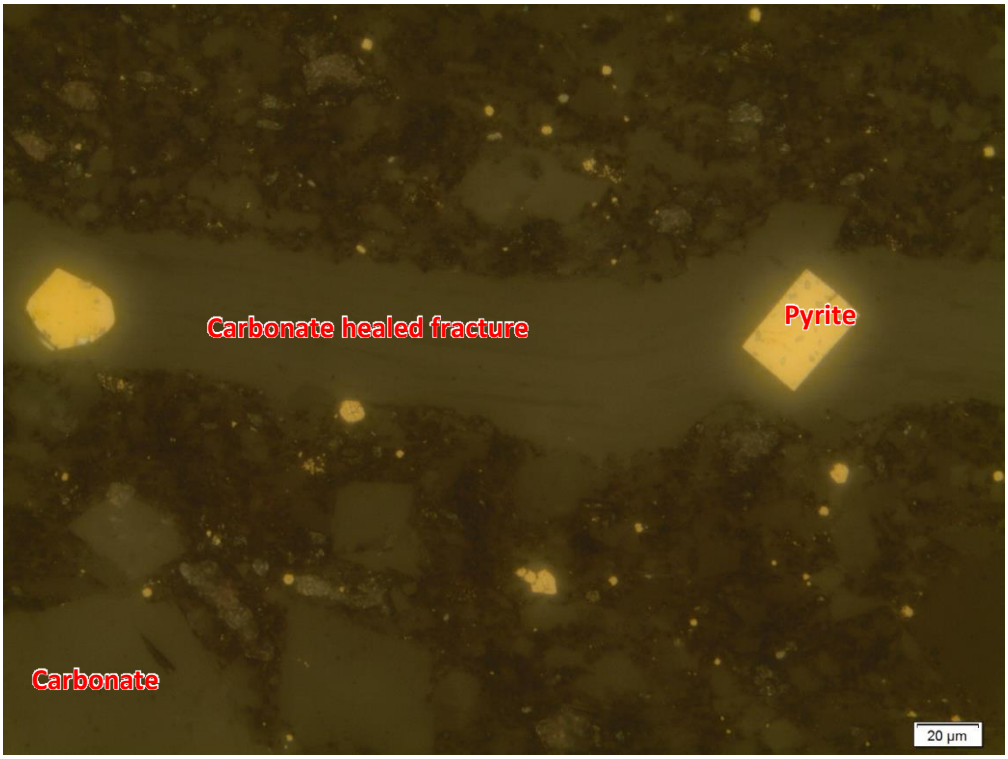

Figure 30- 8605.42 40, 40X reflected light. Carbonate healed fracture with included pyrite, surrounding matrix

6.2 Light and Electron Optical and comparisons

The most common mineral assemblages found in all samples are calcite, quartz, pyrite and marcasite, dolomite, muscovite, illite, chlorite, apatite, kaolinite, and albite. Other minerals observed include celestite, zircon, sphalerite, rutile, and gypsum/anhydrite though these are rare. Most commonly, samples are dominated by calcite, quartz, pyrite, and clays.

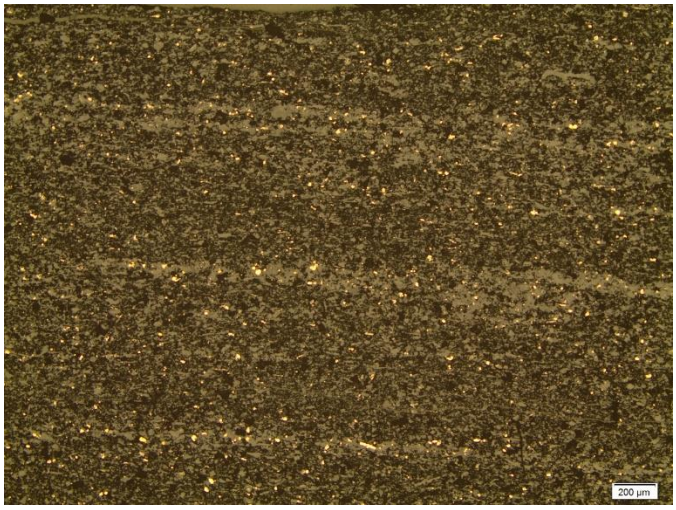

Figure 31- Typical rock fabric, defined by increasing and decreasing carbonate content and grain size. 9B 8555.41 4X, reflected light

Rock fabric is primarily distinguished by the size of calcite and quartz grains within the matrix and the presence of fossiliferous carbonate and phosphates (Figure 31). Matrix calcite and quartz grains are as small as 4 microns (8492.4) to larger than 50 microns (1B 8478.8, 2B 8481.9, and 8B 8549.13) with the significant size variance. Matrix grain size is largely coupled with presence or absence of fossiliferous carbonate, suggesting finer grained matrix was deposited in lower energy environments free from storm surges and largely inhospitable to organisms due to low oxygen.

Calcite is found as irregular grains within the matrix, pellets, and fossils. Quartz is most commonly found as irregular grains within the matrix, but also replaces portions of larger fossiliferous carbonate. Calcite has a moderately negative correlation with quartz, likely due to changes in fossiliferous carbonate influxes, as well as a strong negative

correlation with clay content. While these minerals are found with one another, these correlations are related to abundance rather than strict associations. This is due to carbonate displacing the concentrations of clay and quartz than suggesting they are inversely deposited.

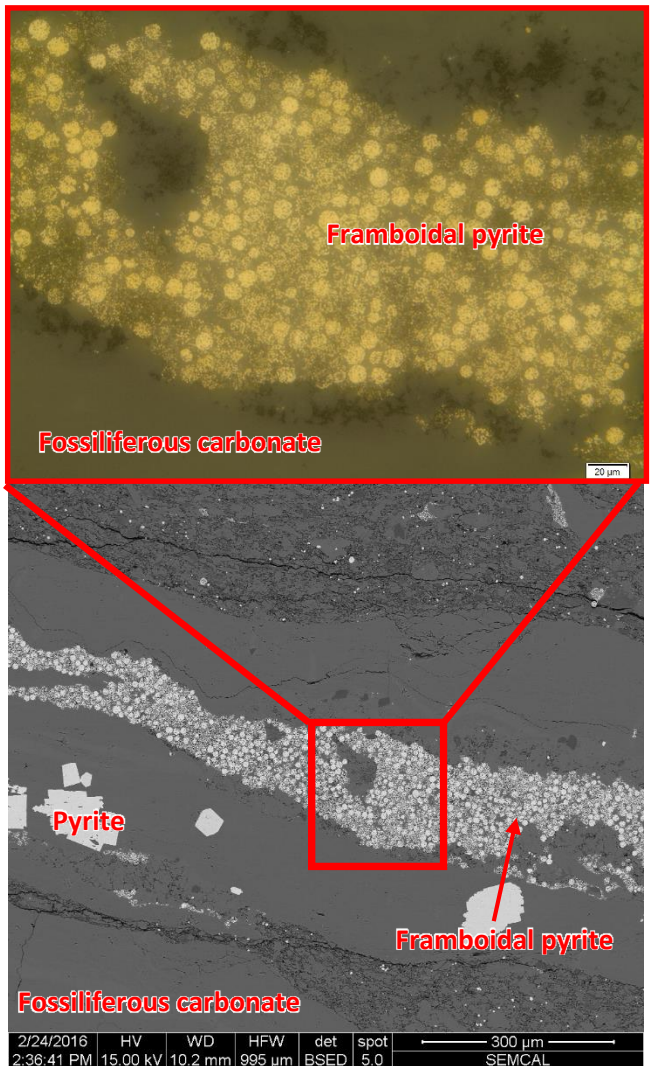

Figure 32- 11B 8585.81 40X reflected light and BSE SEM image. Framboidal pyrite and euhedral pyrite in skeletal carbonate layer.

Pyrite is often found within or near carbonate, suggesting pyrite often replaces carbonate. This is especially true for large euhedral pyrite grains, some of which measure hundreds of microns in dimension. Large (>100 microns) fossils of brachiopods, bivalves, crinoids, and mollusks are often partially replaced by pyrite. Similarly, matrix carbonate grains often have small parts replaced or are almost entirely replaced by pyrite. Framboidal pyrite is often found in large quantities between skeletal carbonate in clay and organic rich regions (Figure 32). These large aggregates contain numerous framboids that extend for hundreds of microns with framboid sizes ranging from hundreds of nanometers to roughly 25 microns in diameter. Framboids are also found within the matrix and in carbonate, both matrix and fossiliferous, but typically

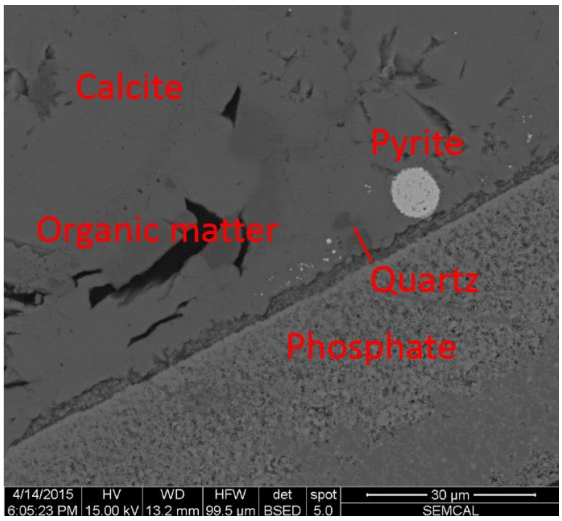

Figure 33- 1B 8478.8 BSE SEM image. Phosphatic clay sized grains.

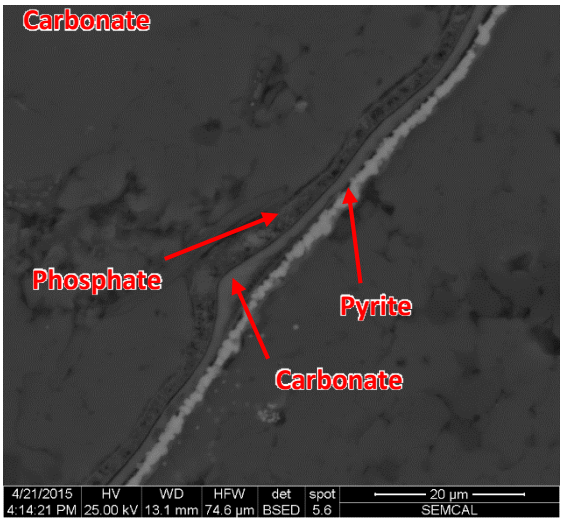

Figure 34- 1B 8478.8 BSE SEM image, carbonate and pyrite replacing skeletal phosphate.

are found individually or in small groups, not large aggregates. Framboids found within the matrix range from 4 microns to 40 microns, whereas framboids found in carbonate ranging from one to 30 microns in diameter. Framboidal pyrite is often present with pyritohedrons of sulfides of similar size. Occasionally marcasite is found along with pyrite displaying a distinguishable white color in reflected light and orthorhombic crystal habit, often found either as irregular crystals of just a few microns across or as small tabular aggregates.

Phosphate is found both as a phosphatic clay to silt sized grains with individual early authigenic phosphate grains (Figure 33 and 34) measuring on the order of nanometers as well as phosphatic fossil debris. Phosphatic silt is found throughout the samples and likely is a result of precipitation, having a “sugary” texture. Phosphatic fossil debris are found in fossiliferous and coarser fabric areas, sometimes associated with calcite and pyrite. Carbonate and pyrite often are found replacing both forms of phosphate.

All clay minerals occur within matrix, often wrapping or lining carbonate, quartz,

or framboidal pyrite, therefore providing evidence of detrital origins for these minerals (Figure 35). Some areas have significantly higher concentrations of clay minerals though this may be interpreted as lacking larger quartz and carbonate minerals rather than an increase in clay minerals. These changes are interpreted as resulting from changes in sedimentation rate and sea level, with the smaller grained matrix sections deposited during highstand.

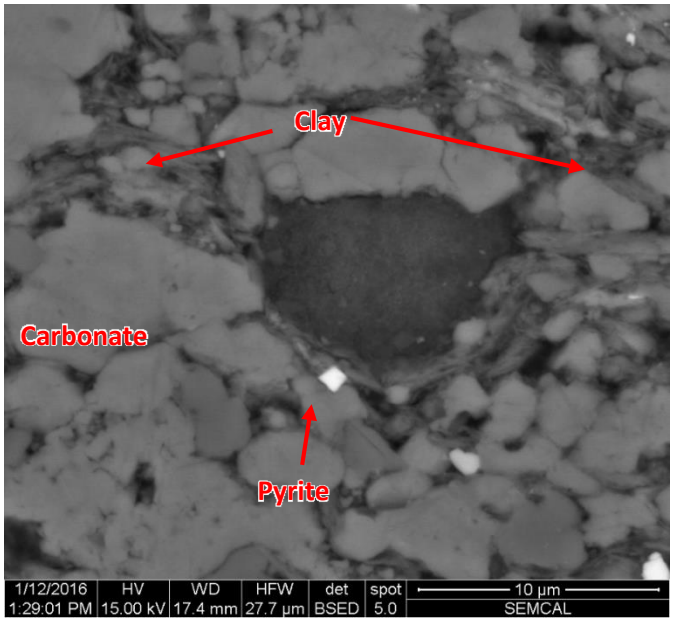

Figure 35- 8492.4 SEM BSE image showing fine grained matrix and clay wrap

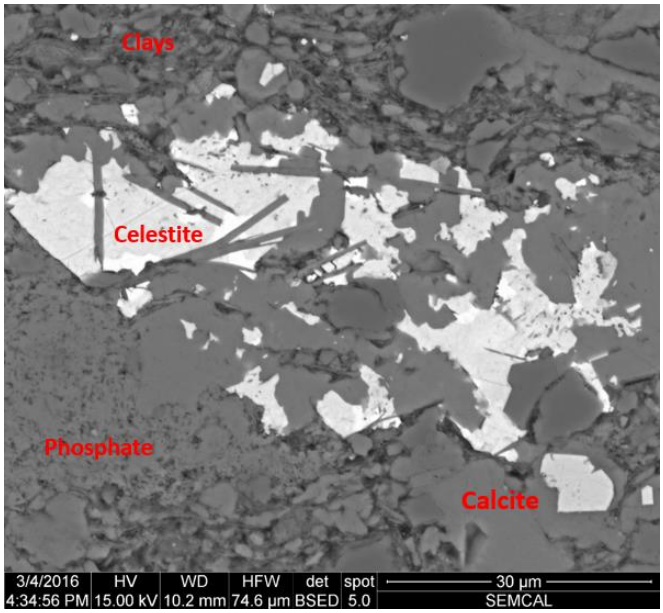

Figure 36- 8528.8 BSE SEM image, celestite replacing carbonate

Much like pyrite, celestite (strontium sulfate) is found replacing carbonate (Figure 36). It takes the form of the previous mineral, often as 10-30 micron euhedral to subhedral grains, with some tabular sections which may be replaced gypsum (Figure 36). The existence of celestite in this rock is significant because it may be the source of strontium in produced

waters although it is only present in trace quantities.

6.3 QEMSCAN

All samples were analyzed with the FEI Quantitative Evaluation of Mineralogy by SCANning Electron Microscopy (QEMSCAN®) analytical platform at least once, although for the purposes of this study the results are only used to observe mineral-fabric relations. The mineral maps provided by QEMSCAN can show in detail the distribution of minerals, their associations, and submillimeter scale variations in fabric (Figures 37 and 38).

While QEMSCAN provides a quantitative calculation of mineral volume, this proved difficult for three main reasons. First, in order to quantify minerals spatial resolution for grain boundaries must be taken into account. This process has a great deal of error as the user must estimate grain boundary relations (e.g. carbonate/illite boundaries may be classified as a significant percent of the matrix, the user must estimate what percentage of the boundary is carbonate and what percentage is illite). This process can be improved by increasing resolution to estimate fractional pixels through using a lower incident beam voltage of 15 keV spot analysis during QEMSCAN and analyzing grain boundaries. This is because interaction volume is inversely proportional to keV. Second, QEMSCAN provides a mineral map of 1.5 mm by 1.5 mm or 3 mm by 3 mm, a tiny subsample of a much larger and complex sample. The size of the mineral map can greatly change the mineral concentration due to changes in fabric so conflation of the subsample to that of bulk mineralogy is negligent. Bulk mineralogy assessments are best obtained by XRD, as this technique allows for more homogenized sampling. Lastly,

QEMSCAN provides a 2-dimensional view of mineral associations and fabric meaning some data are lost in the z direction. QEMSCAN may overestimate or underestimate specific mineral concentrations depending on their orientation in the matrix. For example, clay minerals (e.g. illite) tend to coat and wrap siliciclastic and carbonate grains. On QEMSCAN they appear as thin coatings in 2-dimensions, accounting for a small part of the total area and therefore calculated as a smaller concentration. However, in 3-dimensions, their volume is much greater due to a square-cube law proportion difference.

Despite the complexities of quantification, useful qualitative mineral relations can be observed with QEMSCAN, namely the calcite-pyrite relationship as well as the siliciclastics and matrix carbonate relation with illite. Pyrite is seen replacing calcite and appearing as framboids in matrix. Illite is observed surrounding siliciclastic and carbonate grains in matrix, as well as forming longer thin laminae. Fossiliferous carbonate and microfabric exhibit distinct bedding. Additionally, it allows for minerals indistinguishable in light optical microscopy to be identified.

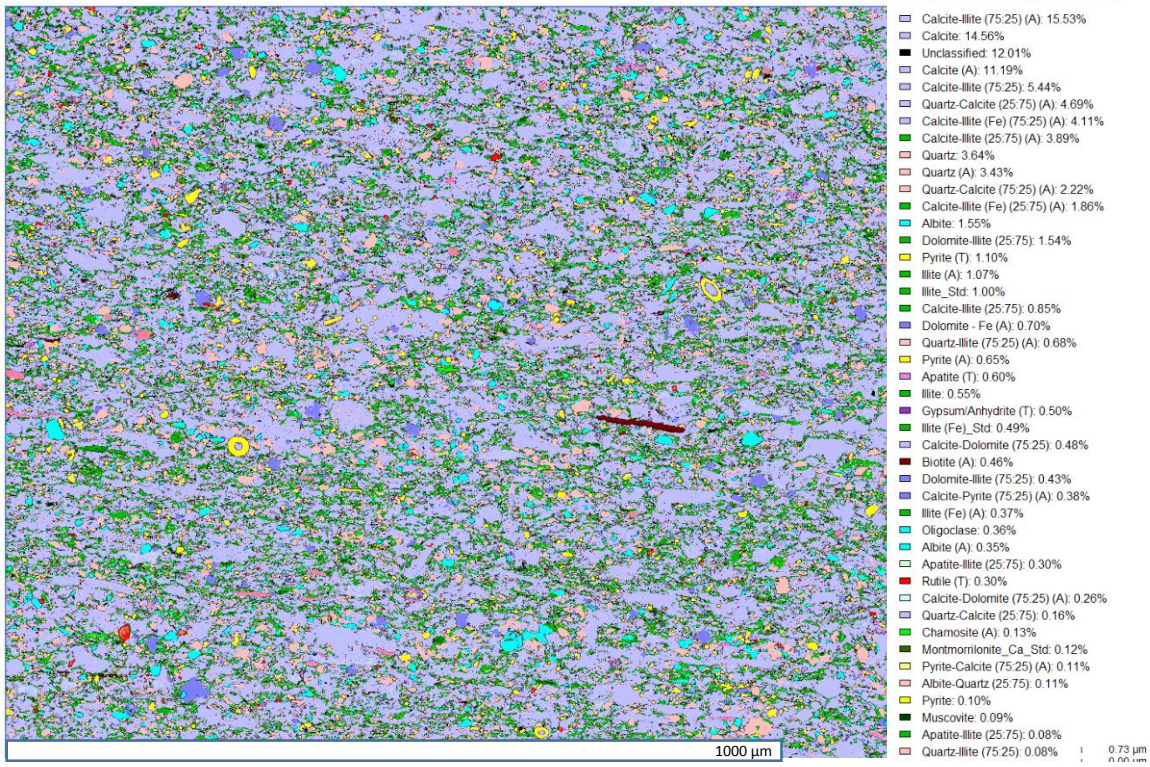

Figure 37- 8492.2 QEMSCAN, mineral key and percentages

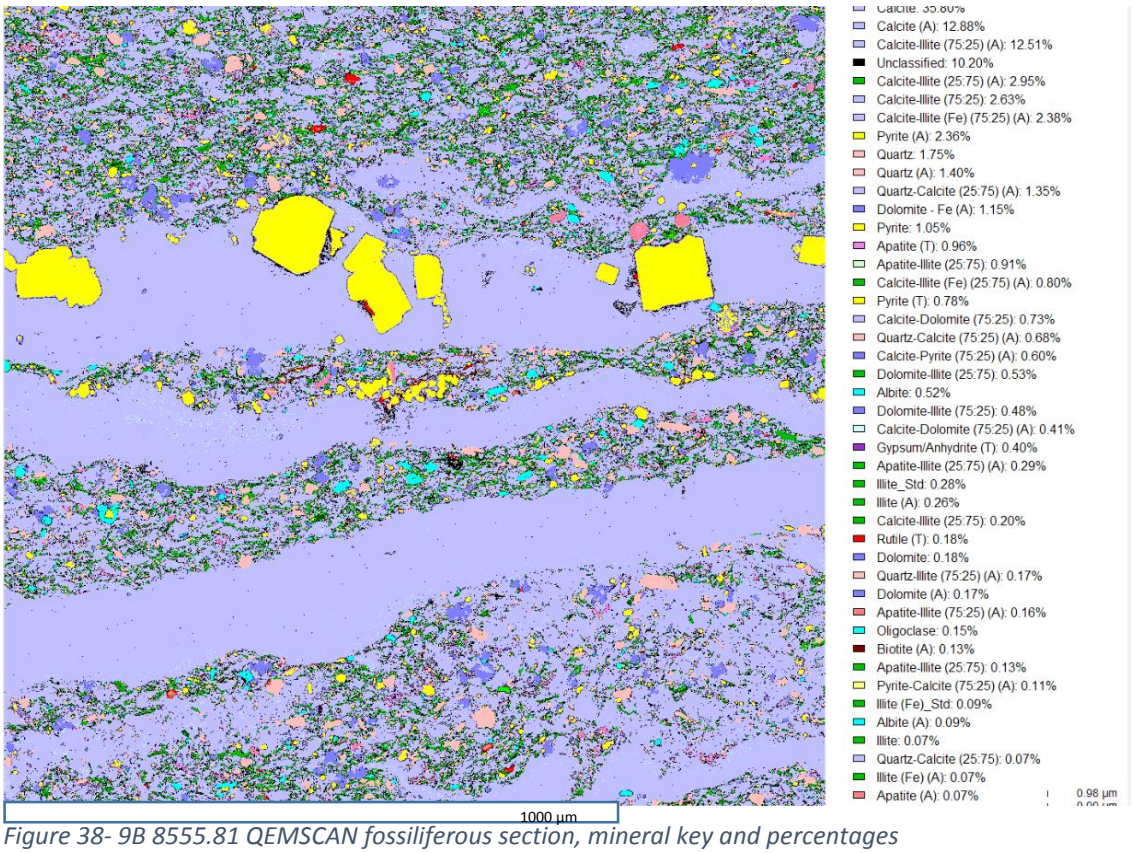

Figure 38- 9B 8555.81 QEMSCAN fossiliferous section, mineral key and percentages

6.4 XRD

Minerals identified by XRD analysis include calcite, quartz, muscovite, illite, pyrite, dolomite, albite, chlorite, amesite, and fluorapatite (Figure 39). All samples contain a detectable quantities of calcite, quartz, muscovite/illite, dolomite, albite, and pyrite. Amesite was detected in 1B 8478.8 carbonate subsample and 2B 8481.8 carbonate subsample, although this is possibly a chlorite, chamosite, or kaolinite fraction that is yielding an amesite signal due to the random orientation of the minerals to the beam. Fluorapatite is only detected in 9B 8555.4 (approximately 3 mass percent). Calcite concentrations relate inversely with clay concentrations.

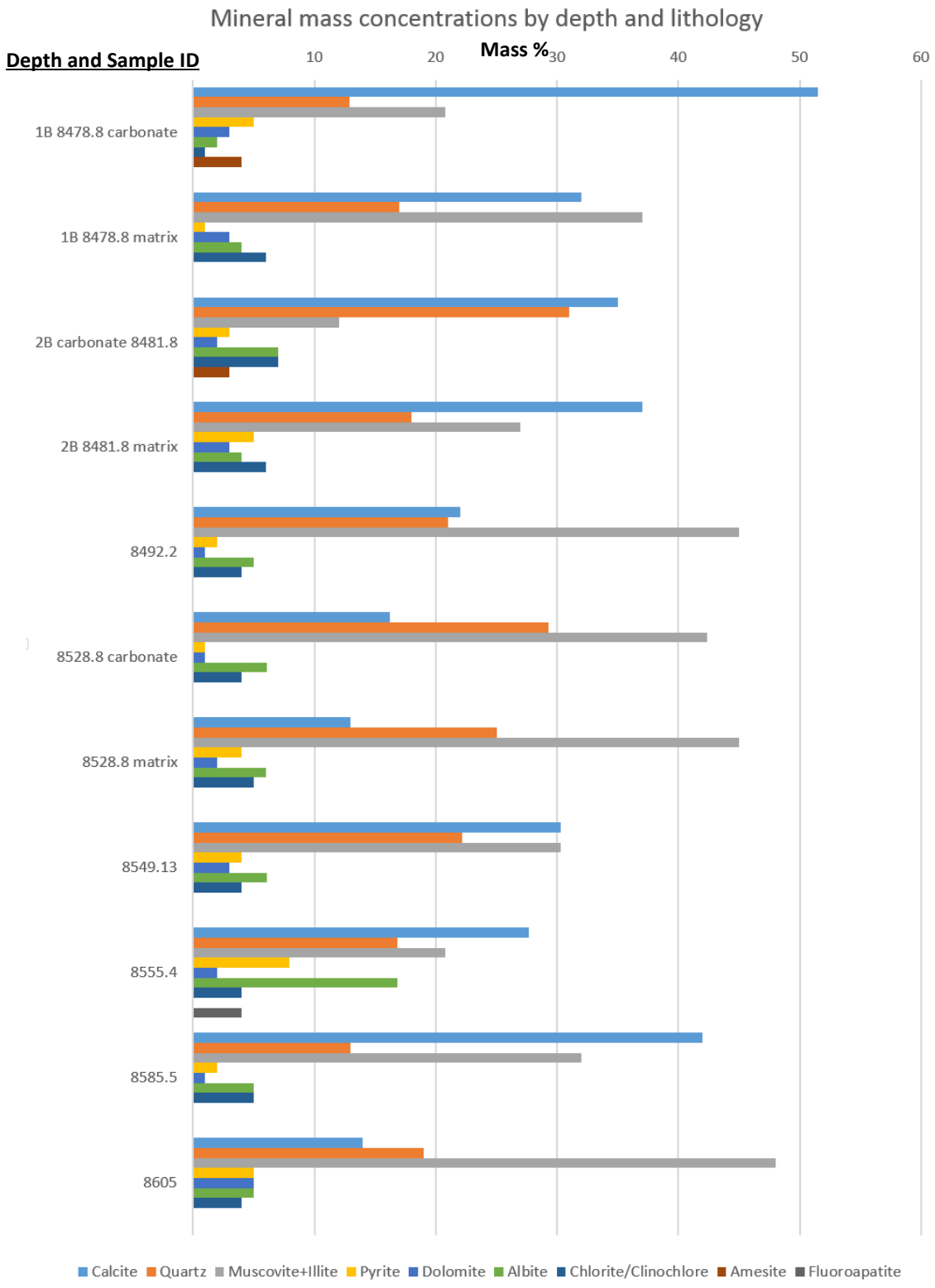

Figure 39- Mineral concentrations by depth and lithology

6.5 XRF

Cobalt (Co), Chromium (Cr), Copper (Cu), Vanadium (V), Zinc (Zn), and Uranium (U) were selected as redox sensitive elements. These elements show lower to average concentrations compared to the average organic shale (Wedepohl, 1971). Concentrations of redox sensitive elements show variability with depth (Figure 41). Because trace elements in shales have both detrital and authigenic sources and we are interested in redox variations in the water column and sediments which are only controlled by authigenic sources, a normalizing procedure is necessary. The method used in this study is to normalize elements to aluminum which is detrital in origin and concentration of which unaffected during diagenesis (Algeo and Maynard, 2004). In order to determine that Al comes from siliciclastic flux, and that Al enrichment is not over or under estimated it is compared to another detrital origin element. To accomplish this Al is plotted compared to Th which showed a strong positive correlation (R^2 = 0.9512, n = 8) suggesting Al and Th came from common siliciclastic flux and were not under or over-estimated (Figure 40). Redox sensitive elements were measured confidently well above the lower limit of detection (LLD) for the XRF. LLD averaged 2.77% of concentration, with a minimum of 0.6% (Th) and a maximum of 7% (Co) LLD for the elements were 1.175 for Ni, 0.0354 for Th, 1.041 for Co, 2.026 for Cr, 1.207 for Cu, 2.175 for V, 0.80196 for Zn, and 0.0121 for U. Details on LLD for each sample, run, and element can be found in the Appendix.

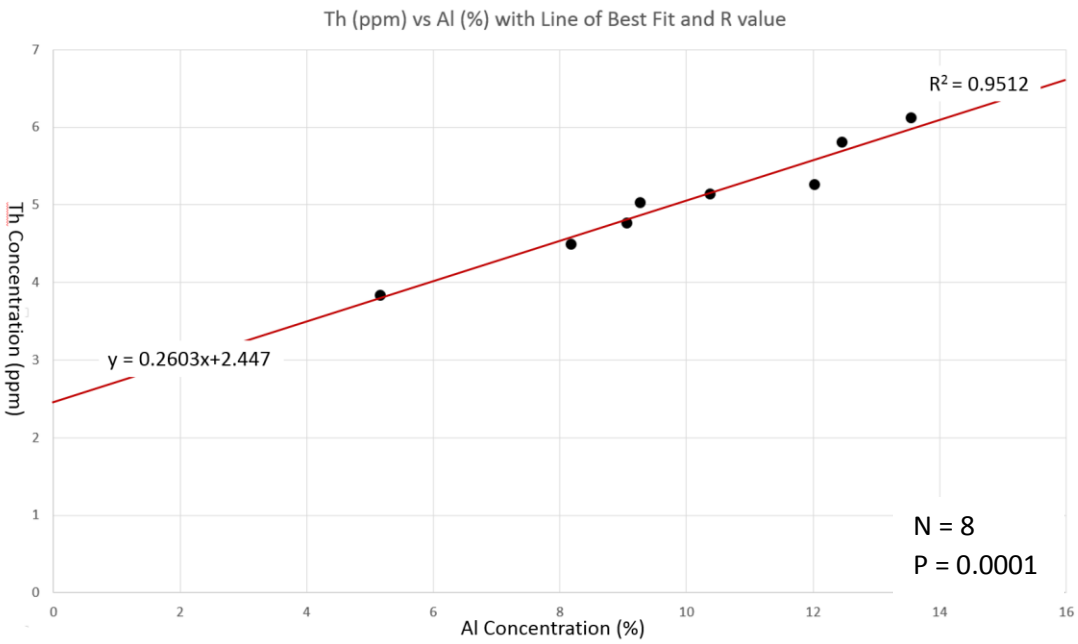

Figure 40- Aluminum vs Thorium concentrations with linear regression and coefficient of determination

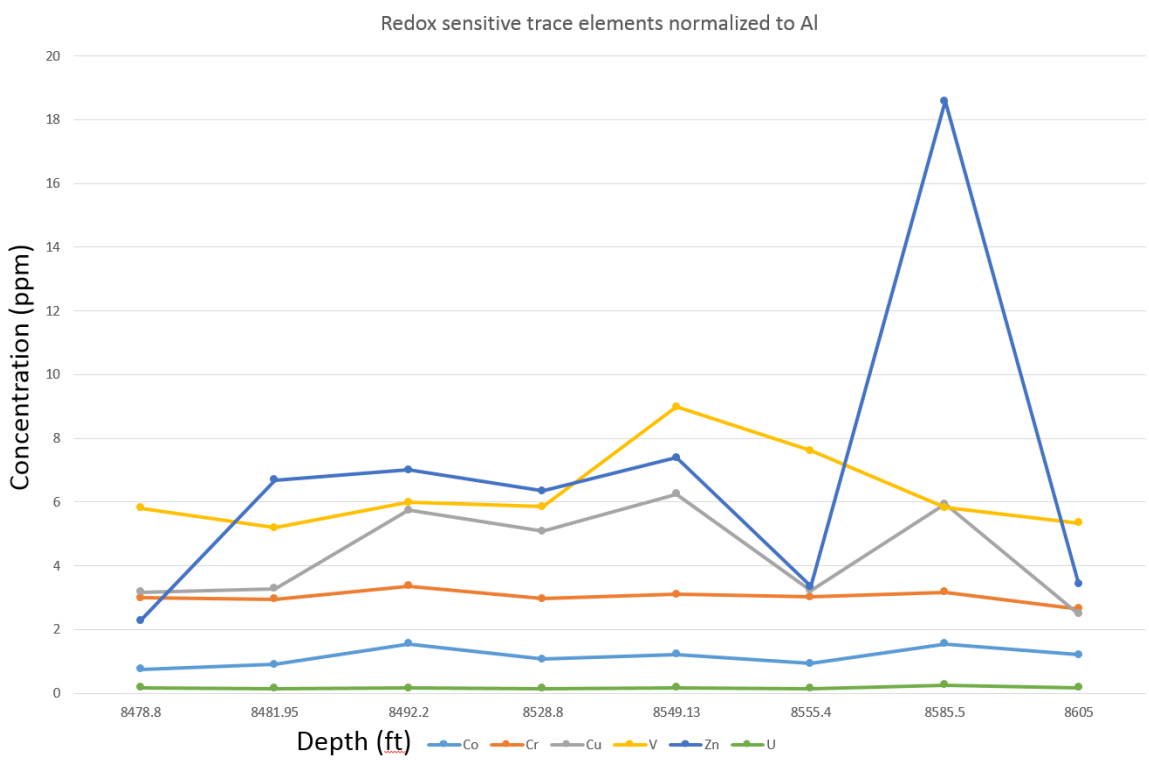

Figure 41- Redox sensitive trace elements normalized to Al, ppm

6.6 SIMS

Secondary ion mass spectroscopy (SIMS, or ion microprobe) is used to determine $^{34}S/^{32}S$ ratios on various morphologies of iron sulfides. Morphologies sampled fall into three categories: euhedral (Figure 42), framboidal (Figure 43), or other. Euhedral pyrite grains are present both in the form of individual euhedral crystals (typically cube) and as aggregates of crystals, often as carbonate replacement. Framboidal pyrite (framboids or "frambs") are present in a range of sizes from single microns to forty microns in diameter. Framboids appear in large-grained carbonate and fine-grained matrix, both as individual framboids and as large clusters. Intact framboids as well as possible relict framboids are denoted as "framboidal", meaning partially recrystallized framboids are still labeled "framboidal". "Other"

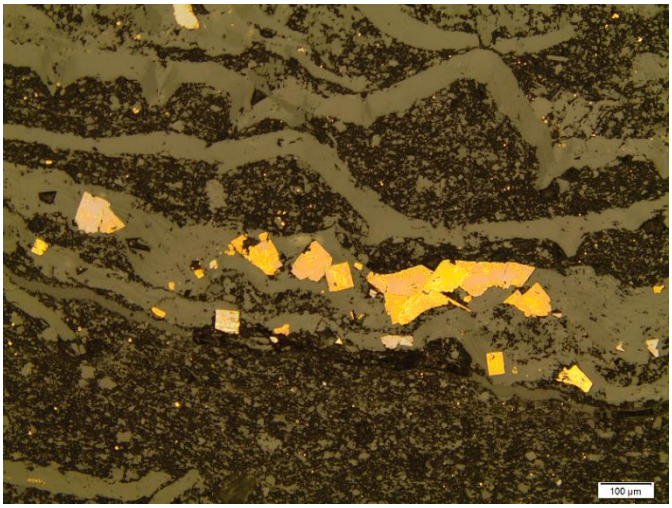

Figure 42- Example of large euhedral pyrite, 8B 8549.13 10X, reflected light

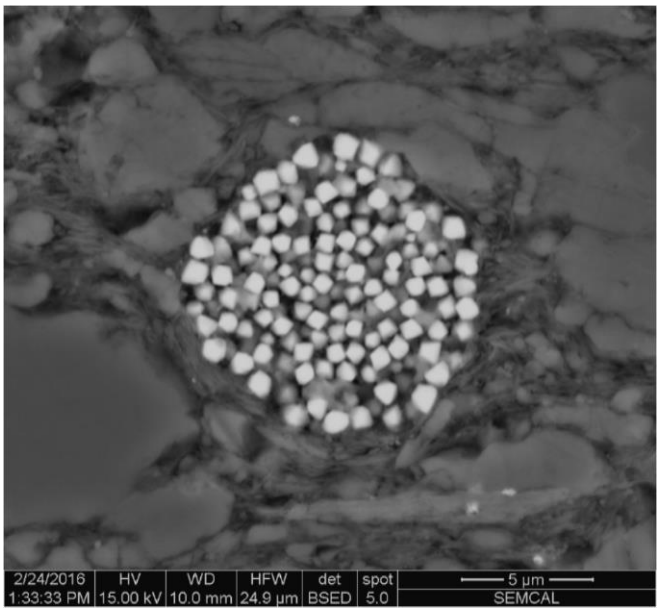

Figure 43- Example of framboidal pyrite, 8B 8549.13 10X, reflected light

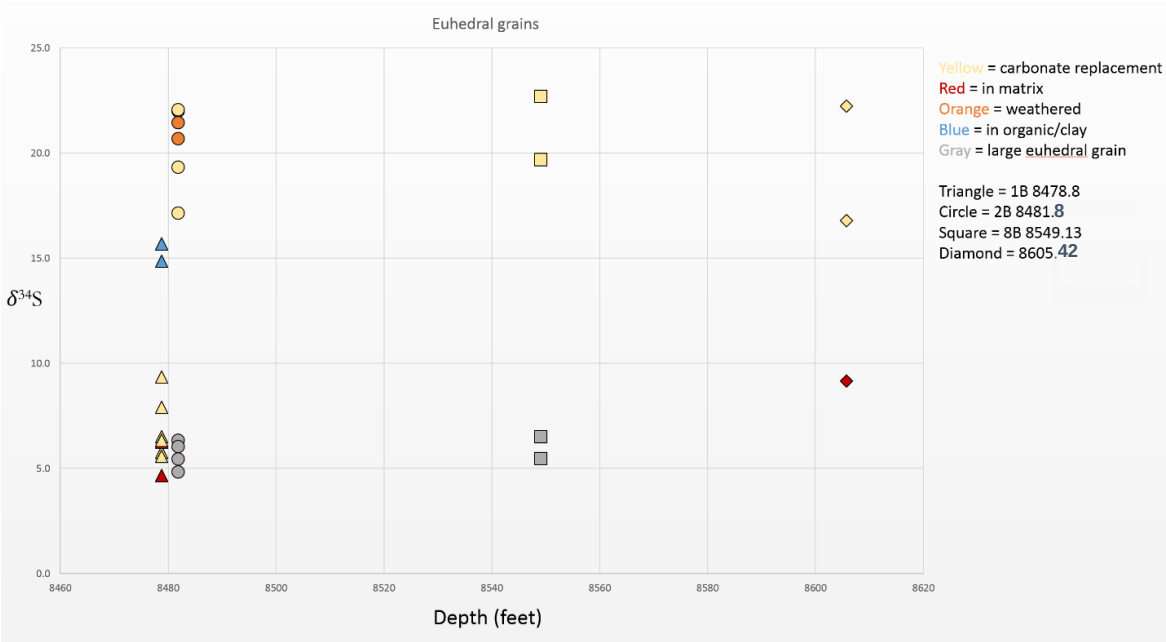

Figure 44- SIMS data by depth and location, Euhedral pyrite. Yellow = carbonate replacement, Red = in matrix, Orange = weathered, Blue = in organic/clay, Gray = large euhedral grain

morphologies include irregular aggregates of small pyrite grains, spherical concentric pyrite (dubbed "snowball"), and aggregates of small pyrite grains that form long strings in what appear to be fluid conduits.

Samples interrogated with ion microprobe include 1B 8478.8, 2B 8481.9, 8B 8549.13, and 8605.42 for a total of 35 points analyzed. 27 points are euhedral, six are framboidal, and two are classified as "other." The overall average δ^{34}S is 9.81, with spot-to-spot reproducibility on the pyrite standard (1σ [‰]) of 0.3‰ to 0.4‰. Overall euhedral grains average δ^{34}S of 12.24. Overall framboidal pyrite average δ^{34}S of -3.05. The two "other" grains average δ^{34}S of 15.55 but are highly variable, the two values being 6.4 (1B 8478.8, spherical "snowball" grain) and 24.7 (8605.42, aggregate of small grains). 1B 8478.8 spherical "snowball" grain is in matrix and not replacing carbonate, while 8605.42 aggregate of small grains is in matrix but within a larger carbonate grain.

Variations in location and morphology appear to have a significant correlation to δ^{34}S in the euhedral pyrite (Figure 44). In all samples, euhedral pyrite grains in the finer grained matrix and large (>60 micron) cubic, cohesive, non-weathered euhedral grains have lower δ^{34}S values (4.8 to 6.5) while pyrite crystals that replaced carbonate, are altered, or are in organic and clay-rich pockets all have significantly higher δ^{34}S (5.6 to 22.7). 2B 8481.9, 8B 8549.13, and 8605.42 all have similar averages (δ^{34}S = 11.5, 14.2, and 12.6, respectively) and distributions of δ^{34}S values for each morphology and location. Sulfur isotope values for sample 1B 8478.8 have a lower average overall (δ^{34}S = 5.4), especially for carbonate replacement pyrite (δ^{34}S = 6.88 for 1B 8478.8 vs 19.98 for 2B, 8B, 8605.42 average). The highest average δ^{34}S is obtained from highly weathered pyrite, with an average of δ^{34}S 21.37. All three highly weathered pyrite points are on 2B 8481.9. The average δ^{34}S value for pyrite replaced carbonate for 2B, 8B, and 8605.8 is 19.98. Two points on 1B 8478.8 are in organic and clay rich pockets, with an average δ^{34}S of 15.2. Large euhedral grains and euhedral grains in matrix have significantly lower values, with δ^{34}S of 5.75 and 6.67 respectively. With the exception of pyrite-replaced carbonate in 1B 8478.8, all locations and morphologies are +/- 10% of the average value for each classification. These observations seem consistent for each pyrite location and morphological classification.

While the average δ^{34}S value for framboidal pyrite is -3.05, the six points show significant variance ranging from -18.7 (2B 8478.8, framboid in matrix) to 16.6 (8B 8549.13, large aggregate of framboids). 1B 8478.8 framboids have an average δ^{34}S of -9.4, all values being negative. The slightly deeper 2B 8481.9 single point having a value

of -18.7. 8B 8549.13's only point is a large aggregate of framboids in a clay and organic-rich region between skeletal carbonate and has a high value of 16.6. Finally, two carbonate-bound framboids in 8605.8 have δ^{34}S values of 1.9 and 0.7, for an average δ^{34}S of 1.3 (Figure 46).

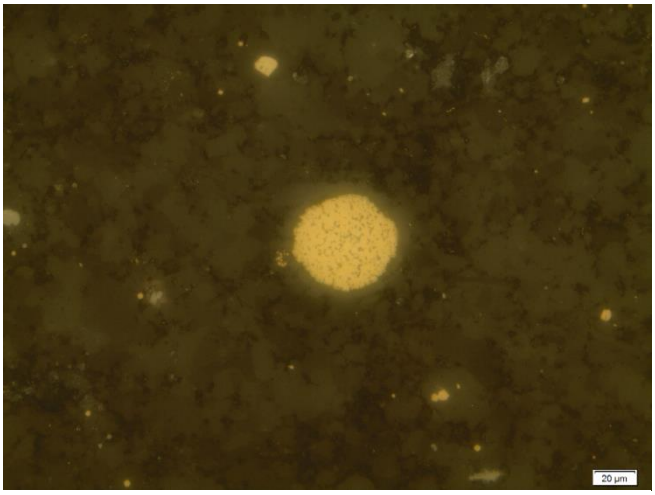

Figure 45- Interpreted framboid in carbonate in 8605.12, 40X reflected light

It is possible that the "framboids" from 8605.42 aren't really framboids at all, but rather, are a form of radial carbonate replacement by pyrite that have subsequently been weathered to resemble a framboid, thereby explaining the positive nature of the δ^{34}S in those grains (Figure 45).

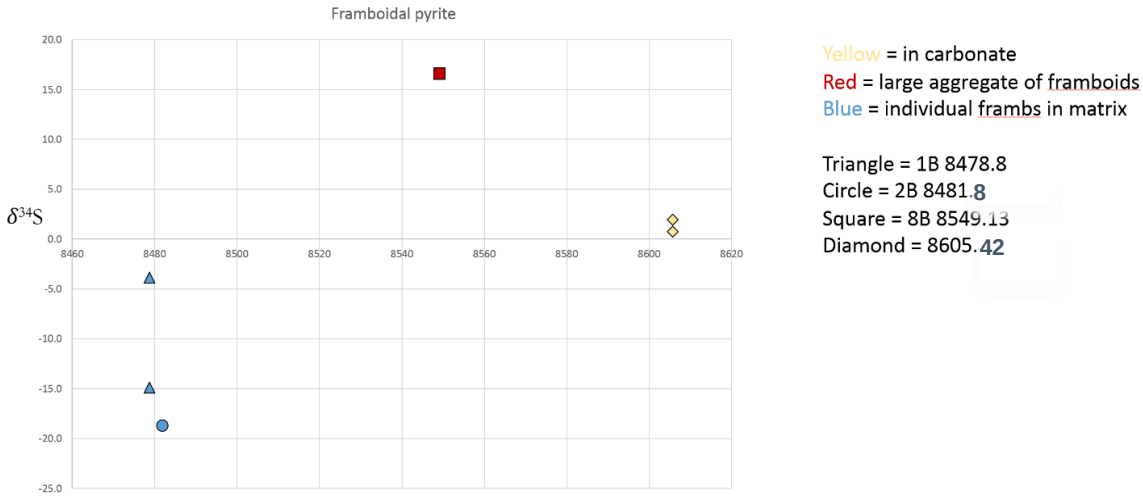

Figure 46- SIMS data by depth and location, Framboidal pyrite. Yellow = in carbonate, Red = large aggregate of framboids, Blue = individual framboids in matrix

Although not part of this study, additional samples from a separate Utica well also were analyzed. In these samples, “traditional” framboids (both in matrix and large-carbonate) have negative values (ranging from -7.5 to -15.7), all points being taken at a lower depth than the samples analyzed for this study, at just over 4000 feet. In addition, one other point was sampled at a depth of more than 10000 feet. This spot analysis was obtained on a large aggregate of framboids in an organic and clay rich region similar to the grain measured in 8B 8549.13. It also has a high δ^{34}S value of 10.7.

Regarding the large aggregates of framboids, both in 8B 8549.13 and the separate 10000 foot sample, nearby (within 500 microns) euhedral pyrite grains that have replaced carbonate show similar δ^{34}S values. In 8B 8549.13, the δ^{34}S values are 22.7 and 19.7 for an average of 21.2 while the δ^{34}S value for the large aggregate of framboids is 16.6. In the 10000 foot sample, two euhedral grains of pyrite that have replaced carbonate located a mere 100s of microns from the large aggregate of framboids have δ^{34}S values of 11.3 and 12.3 (average of 11.8). Compared to the δ^{34}S value for the large aggregate of framboids of 10.7, these values suggest the framboids likely were formed from similar grains due to the similarities in δ^{34}S values. Despite the small sampling, large aggregates appear to show higher δ^{34}S than individual framboids and similar to the δ^{34}S of the surrounding euhedral pyrite grains.

Classified “other” morphologies have positive values, but are highly variable. Samples previously mentioned from separate Utica wells show similar results, with numerous positive values and a single negative value. One apparent pattern is aggregated euhedral or tabular pyrite grains, typically found in clay and organic-rich regions and

forming long strings of pyrite grains, all have positive $\delta^{34}S$ values averaging 15.46. These values often are similar to nearby euhedral pyrite-replaced carbonate grains, and similar to analyses of the large aggregates of framboids.

6.7 MICP

Nine samples were run for MICP: 1B carbonate, 1B matrix, 2B, 8492, 8528, 8B, 9B carbonate, 11B, and 8605. 1B carbonate and 9B carbonate were specifically selected as highly fossiliferous carbonate regions and each have similar total cumulative connected porosities, 2.16% and 2.15%. The remaining samples have connected porosities ranging from 3.66% to 6.59%. Pore throats for the 1B and 9B carbonate samples show approximately six times less connected pore volume for pores with pore diameters less than 10 nanometers (Figure 47). This is interpreted as a result of decreasing clay content. For all samples the majority of porosity is the result of pores with diameters less than one micron. Data for all samples is ignored for pore throats higher than 100 microns as any increase in pore volume was likely due to a shrink-wrap

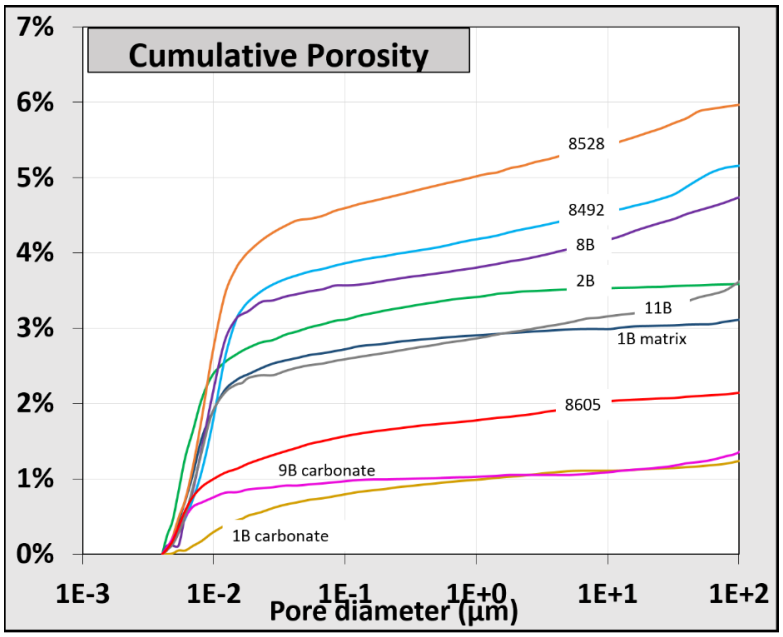

Figure 47- Cumulative porosity by pore diameter

effect of mercury on the surface of the sample.

Porosity decreases with increasing carbonate content with a coefficient of determination of $R^2 = 0.8475$ (Figure 48). For every mass percent decrease in carbonate concentration porosity decreases by 0.1%. The opposite holds true for clay content and porosity (Figure 49). Porosity increases with clay (sum of phyllosilicate, illite, and chlorite) concentrations with a coefficient of determination of $R^2 = 0.7658$. For every mass percent increase in clay concentration, porosity increases by 0.12%.

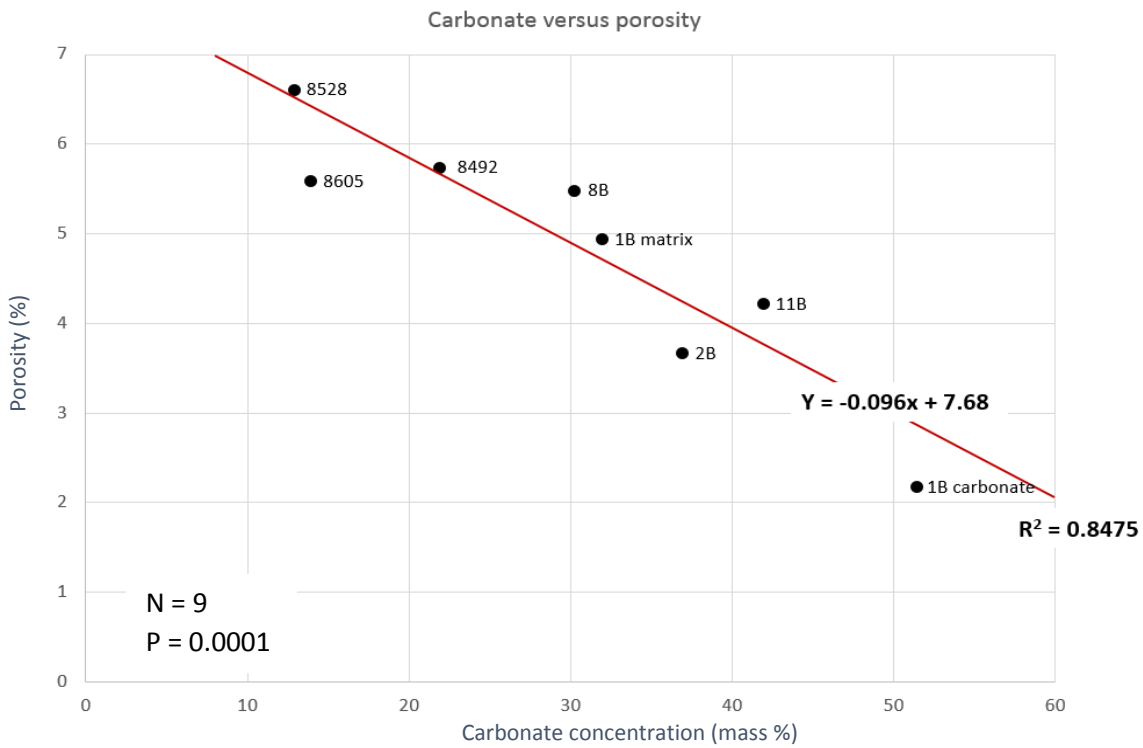

Figure 48- Carbonate content vs porosity

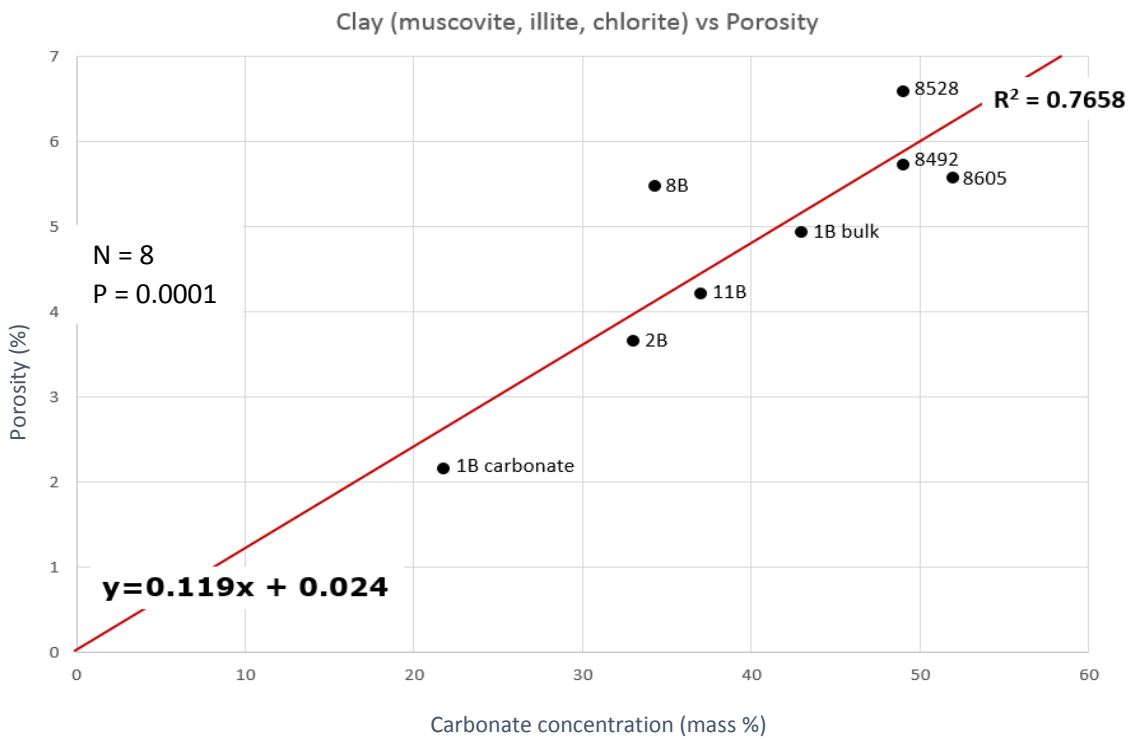

Figure 49- Clay content vs porosity

6.8 XCT

Samples show variation in density on the millimeter scale. Some samples, such as 1B 8478.8, exhibit less layering and more bioturbation due to high fossiliferous carbonate content throughout the sample. Other samples, such as 11B 8585.5, show discrete layering due to carbonate rich layers and matrix dominated layers. Although clay minerals and carbonate minerals have similar densities (2.6-2.8 g/cm^3 and 2.71-2.83 g/cm^3 respectively) the matrix rich layers exhibit lower densities due to the increase in pore space and potentially increased organic content while the carbonate rich layers show lower density due to the decrease in porosity (Figure 50). Resolution is too low (650 microns) to identify individual fossils or porosity but gradual changes in density due to millimeters-scale changes in mineralogy and porosity are visible.

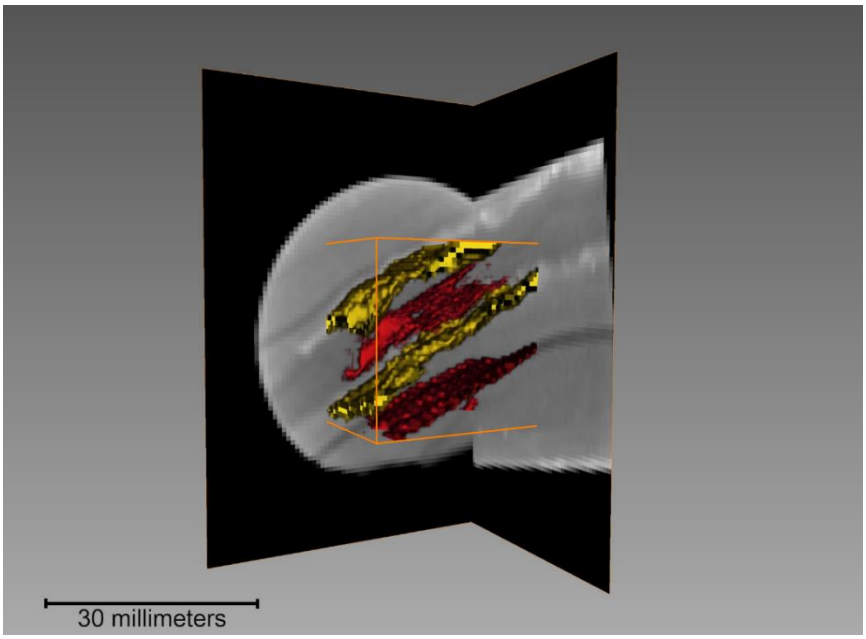

Figure 50- XCT of 11B 8585.51, yellow is higher density (carbonate), red is lower density (clays, organics, fracture)

6.9 TOC

TOC obtained from mass spectrometry gave values ranging from 0.486% to 3.382%. TOC is highly variable with no correlation to depth. TOC correlates moderately well with porosity ($R^2 = 0.7942$, $y = 1.114x + 2.33$) with every percent increase in TOC porosity increases by 1.1 %. TOC correlates with clay content ($R^2 = 0.7827$, $y = 7.51x + 23.7$) with every percent increase in TOC increasing clay content by 7.5%. Trace elements show weak or no correlation with TOC concentration.

It is possible TOC values have too large of an error to draw significant conclusions from the data. Additional samples should be run to back up these conclusions made using this TOC data.

Data from XRF loss on ignition (LOI) process was used to calculate TOC based on the mass change before and after burning off organic carbon. However, the results were suspiciously high and therefore were disregarded. The organic carbon mass-loss from LOI was likely overstated as some water may have been lost from the samples as well, increasing the interpreted TOC concentration.

7. Discussion

7.1 Mineralogy

The mineralogical composition of this suite of mudrocks is attributed to a number of factors. Available elements, sediment source, biological (including microbial) activity, fluid flux, and diagenesis are among the variables that could influence the mineralogy and abundance in a shale. All samples are comprised of a few dominating minerals: calcite, quartz, muscovite/illite, dolomite, pyrite, albite, and chlorite.

Calcite is present in the form of clastic grains, cement, and fossils. Much of the calcite, especially the fossiliferous carbonate, formed in oxic or slightly suboxic conditions with significant nutrient and sediment influx into the basin. Warm water carbonates associated with the epeiric sea during the Ordovician formed in subtropical to tropical conditions in the shallow sea or on the Trenton shelf. Changes in currents across this shelf, along with eustatic sea level and subsidence of the basin, all could have affected nutrient level and redox and therefore biogenic production of carbonate. Large layers of fossiliferous carbonate can be interpreted as periods of nutrient-rich oxic

conditions whereas the lack of fossiliferous carbonate can be seen as dysoxic to euxinic conditions or deeper water conditions. The rapid sequencing from large fossils and carbonate to argillaceous matrix suggests large storm surges in the sub-basin created rapid influx of material and oxygen during subsidence of the Lexington platform sequenced with periods of anoxia and reduction during basin isolation. Authigenic calcite, occuring both in fractures and as cement, likely was due to the transformation of smectite to illite, a process that produces abundant calcium and water (van de Kamp, 2008). Calcite filled fractures can be distinguished from epoxy filled fracture by noting irregular lamination within the fracture caused by carbonate mineralization or by the presence of replacement minerals in the fracture (Figure 51) (e.g., pyrite replacing carbonate). Fossiliferous carbonate typically is distinguishable from carbonate filled fractures as it tends to be less than a few millimeters in length, has distinct morphologies in larger

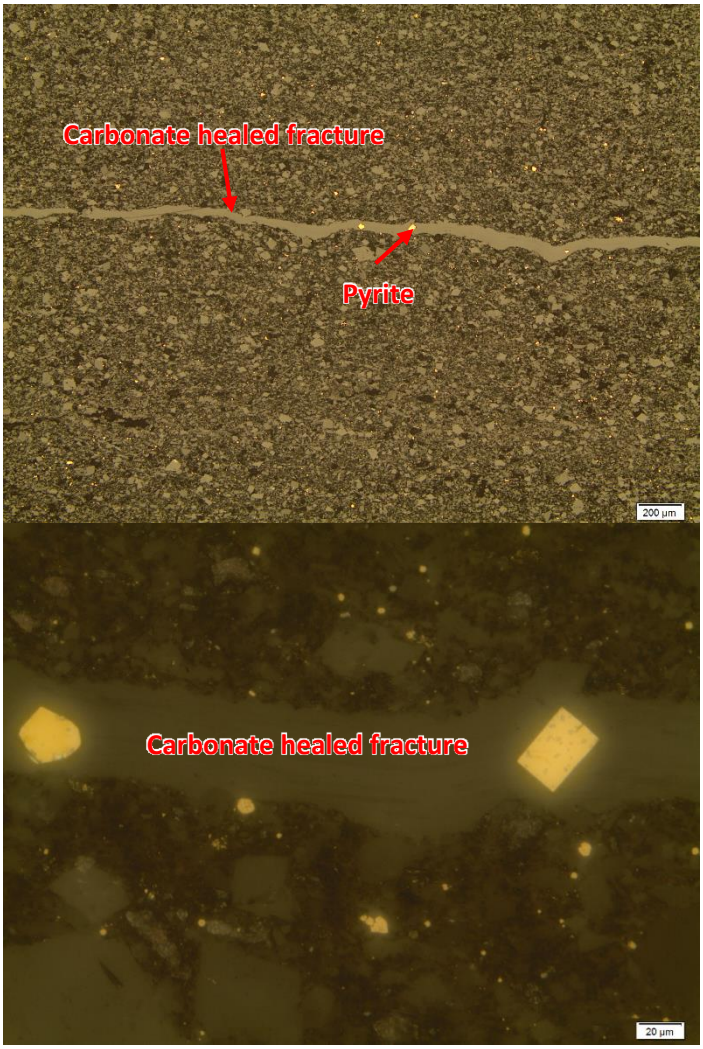

Figure 51- 8605.42 4X and 40X, reflected light. Carbonate filled fracture with pyrite replacing carbonate

fossils, and tends to have regular width. Fractures typically span the entirety of the thick section, about 2 cm, have no distinct morphologies that could be misconstrued as biological, and often have irregular widths presumably due to compaction and stress changes.

Quartz is sourced both from terrigenous fluvial input and authigenic formation from silica produced by the smectite to illite transformation. The reaction of smectite to illite in porous networks of rocks releases micron-scale sub-spherical grains of quartz that fill in pores and clay networks, cementing the mudstone (Jahren et. al., 2009) Quartz also often replaces fossiliferous calcite, possibly due to the partial dissolution of the carbonate and replacement with quartz due at higher pore water silica concentrations. Quartz growth is also known to increase Gibbs free energy and solubility of calcite by exerting pressure on carbonate during growth (Maliva, 1988).

Illite is the dominant clay mineral, with some evidence of muscovite in the XRD data, and rarely some clinochlore (Mg-rich chlorite). The clays transformed from smectite to illite and illite to muscovite, releasing SiO_2 in the process.

Smectite (montmorillonite) to Illite

$1.308[(Al_{3.15}Mg_{0.85})(Si_{8.00})O_{20}(OH)_4(Na_{0.85})2H2O + (0.06Fe_2O_3 + 0.56K_2O + 0.02CaO)]$

$\rightarrow(Al_{4.12}Fe_{0.1}Mg_{0.56})(Si_{7.17})O_{20}(OH)_4(K_{1.47}Na_{0.01}Ca_{0.03}) + 3.29SiO_2 + 0.56Na_2O +$

$0.55MgO + \quad 3.23H_2O$

Illite to Muscovite

$1.456[(Al_{4.12}Fe_{0.1}Mg_{0.56})(Si_{7.17})O_{20}(OH)_4(K_{1.47}Na_{0.01}Ca_{0.03})] \rightarrow$

$K_2Al_4(Si_6Al_2O_{20})(OH)_4 + 4.44SiO_2 + 0.14Fe_2O_3 + 0.81MgO + 0.02Na_2O + 0.05CaO +$

$0.9H_2O$

(adapted from van de Kamp, 2008)

The smectite to illite transformation occurs between 60˚C to 100˚C (Jahren et. al., 2009) and the illite to muscovite transformation begins as low as 100˚C. These samples are in the condensate-gas window meaning they likely did not reach a temperature sufficient to transform all illite to muscovite-mica, resulting in some leftover illite. They also could have not had sufficient time to allow for complete transformation. Some muscovite may be of detrital origin as well.

Phosphates, often found in the form of fluoroapatite fossils and microcrystalline phosphate oozes, were likely formed in higher pH and oxic conditions. Decaying organic matter or phosphate-rich tissue, often mitigated by sulfur oxidizing bacteria, leads to phosphatization (Klug, 2005). Phosphates often are replaced by carbonates. 9B 8555.84 is the most phosphate-rich sample. This is interpreted as being the result of increasing nutrient flux due to changing currents. The currents would have carried warm, nutrient-rich waters into the cooler and deeper basin, increasing phosphatization (Nothholt et. al.,

2005).

Celestite is interpreted as a late diagenetic mineral caused by brine-rock interaction at depth (Figure 52). As brine interacted with evaporates (likely gypsum and/or anhydrite) in the sediment, increased Sr was released into the fluid. Once this fluid was reintroduced to carbonate and sulfate-rich phases of rock it precipitated and replaced gypsum and carbonate (Ehya et. al., 2013).

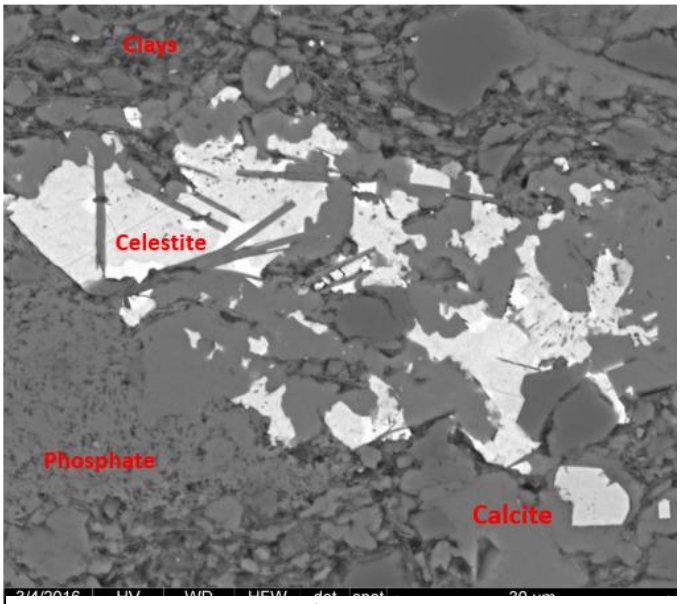

Figure 52- BSE SEM image of 8528.83 showing celestite replacing carbonate with phosphate and clay in matrix.

Pyrite was formed through a number of processes often mitigated by bacterial reduction of sulfate and anaerobic methane oxidation, and is covered in the next section.

7.2 Sulfides and S isotopes

$^{34}S/^{32}S$ ratios exhibit an interesting distribution trend both in regard to morphology and location. Euhedral pyrite, as expected, had positive $\delta^{34}S$ while framboidal pyrite has lower, sometimes negative, $\delta^{34}S$. Within the euhedral grains sampled, another pattern in $\delta^{34}S$ was evident. Weathered pyrite, carbonate replacement pyrite, and pyrite in organic all had significantly higher $\delta^{34}S$ compared to pyrite both carbonate in matrix and as large euhedral grains. These differences in $\delta^{34}S$ within the

same samples is likely due to timing and mechanism of formation of these euhedral sulfides.

While not all pyrite is formed biotically, sulfate reduction by bacteria to form H_2S can be critical to the precipitation of pyrite (Kohn et al., 1998). Bacteria prefer the lighter ^{32}S during this process due to it needing less energy to separate the sulfur from oxygen than ^{34}S, thereby fractionating $^{34}S/^{32}S$ and reducing the $\delta^{34}S$ in H_2S. The amount of sulfate, and therefore sulfur, being limited for the bacteria to utilize means the process can be described by Rayleigh distillation processes. Rayleigh distillation can be described by the equation:

$$R = R_o f^{(\alpha-1)}$$

where R_o is the initial isotopic ratio, R is the isotopic ratio when fraction (f) of the starting amount remains, and α is the fractionation factor (Seal II, 2006) When we use the equation for $\delta^{34}S$ the equation can be expressed as:

$$\delta^{34}S = (\delta^{34}S_o+1000)f^{(\alpha-1)}-1000$$

with $\alpha>1.0$, bacterial sulfate reduction will preferentially use ^{32}S causing an increase in $\delta^{34}S$ leading to pyrite formation with an increased $\delta^{34}S$. In the case of pyrite formed from weathered sulfides, $\delta^{34}S$ is equal to that of the $\delta^{34}S$ of the initial pyrite or sulfate from which it formed .This is because oxidative weathering of sulfides produces negligible sulfur isotope fractionation (Rye et. al., 1992).

Due to these processes we can reasonably assume that negative or significantly lower $\delta^{34}S$ was at least in part driven biotically. Euhedral grains of pyrite that show very low values likely were formed, at least in part, by low $\delta^{34}S$ framboids created by sulfate

reducing bacteria. These framboids, possibly along with other sulfides, were likely dissolved and subsequently reprecipitated in the form of large euhedral grains or euhedral grains in matrix. It is expected that matrix euhedral pyrite would be formed from precursor sulfides because the more clay-rich matrix has the connected porosity necessary to transport S-bearing fluids from which the pyrite may precipitate.

Similarly, euhedral grains that have high $\delta^{34}S$ values may have formed after sulfate reducing bacteria lowered the available ^{32}S in the system, leaving excess ^{34}S in H_2S for the formation of the euhedral grains. Pyrite replaces carbonate under reducing conditions (Swanson, 1960), with H_2S likely being the primary reducing agent in this case. Sulfate reducing bacteria produced enough H_2S to cause pyrite replacement of carbonate but due to the depletion of ^{32}S in the system, the pyrite that formed had higher ^{34}S.

Framboidal pyrite showed a generally negative or lower $\delta^{34}S$ with a single exception. This points towards bacterial reduction of sulfate that leads to the fractionation of sulfur isotopes. During the reduction of sulfates, bacteria have been known to make greigite that aggregates into small bundles, much like framboids, due to its ferrimagnetism at small particle sizes (Wilkin and Barnes, 1997; Bazylinski and Moskowitz, 1997) which may later form into pyrite. Or the framboids could simply precipitate (due to the highly reducing H_2S, containing low $\delta^{34}S$) in the initial pore waters just below the sediment-water interface immediately after deposition. Additionally microbial degradation of organic matter distributed in the matrix near the framboids could explain the low $\delta^{34}S$. Bacteria require a carbon source and open space, and the clay and organic rich matrix

would have both.

The large aggregate of framboidal pyrite was likely sourced from weathered larger euhedral pyrite crystals that formed in ^{32}S-depeleted conditions in the sediment. A large influx of O_2 could have restored oxic or slightly-dysoxic conditions due to increased bottom water currents or the opening of the basin to additional nutrients. In turn these conditions could weather the large euhedral grains of pyrite, creating iron oxides and sulfate concentrations in bottom and pore waters. After some time, dysoxic to euxinic conditions were restored in the sediment causing the framboidal pyrite to precipitate. Many areas in which large aggregates of framboidal pyrite are present appear to be clay and organic rich zones between fossiliferous carbonate or near fractures, making fluid flux relatively easy and giving the framboids enough space in which to form (Figure 53).

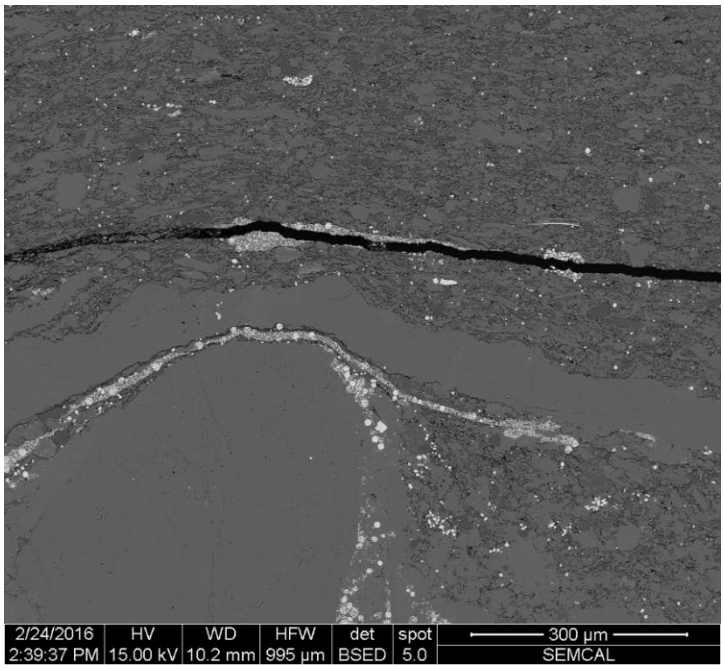

Figure 53- BSE SEM image of 11B 8585.51 showing framboidal pyrite (white) beween fossiliferous carbonate and along a fracture.

An alternative explanation is precipitation of framboidal pyrite out of sulfate-bearing ^{32}S-depleted seawater by anaerobic oxidation of methane. During this process, methanogens deeper in the sediment consume organic matter during sulfate reduction.

This methane diffuses upward to sulfate reducing bacteria that consume the methane along with sulfate from seawater in a process called anaerobic oxidation of methane (Lash, 2015). This process is governed by sedimentation rate, methane flux, and sulfate flux. If sedimentation stops, δ^{34}S rich H_2S diffuses downward to form δ^{34}S rich pyrite and authigenic calcium carbonate (Lash, 2015).

Lastly, they could simply be the product of sulfate reducing bacteria much like the other framboids. The high δ^{34}S in this scenario is due to ^{32}S-depleted conditions caused by their use of ^{32}S in previous sulfate reduction or due to the release of sulfur with a positive δ^{34}S from decomposing organic matter at moderate temperatures (50-80˚C).

These processes also could explain the high δ^{34}S "other" categories of pyrite. The large aggregates of euhedrons that often seem to fill higher permeability areas likely are reworked framboidal pyrite formed in a similar manner as the large aggregate of framboids. The clusters of tabular pyrite or marcasite likely replaced sulfate (likely barite) which replaced gypsum, anhydrite, or organic matter. Reducing fluids then caused the replacement of the sulfate with sulfide. The spherical "snowball" pyrite sampled from 1B 8478.8 was likely formed from gas bubble, calcite cyst, or Liesegang fluid mixing (Schieber and Baird, 2001) that precipitated a mineral that eventually was replaced by pyrite. The gas bubble could provide a surface on which mineralization could occur, especially if the fluid in the bubble influenced precipitation. The mineral precipitated likely would be calcite, the gas being methane or some other reducing fluid to precipitate the carbonate. Pyrite then replaces the carbonate. As a calcite cyst, the pyrite could simply replace the carbonate. Lastly Leisegang fluid mixing can explain the concentric

and round nature of the “snowball” pyrite. In this process, supersaturated fluid containing the ions necessary to precipitate the mineral cause the nucleation of pyrite, thereby depleting the fluid below supersaturation. This cycle of supersaturation, nucleation, and depletion is repeated, creating concentric rings of mineral.

7.3 Trace elements, XRF, and TOC

While trace element concentrations and TOC showed little to no correlation, their respective values lead to some conclusions. As previously mentioned, Al showed a very strong positive correlation with Th suggesting Al and Th both were sourced from common siliciclastic-dominated sediment and could therefore be used to normalize trace elements. Al also showed a positive relationship with Rb, U, Cr, Ti, V, Y, Fe, and, to a lesser degree, Co. These elements can be considered as Al-group (detrital) elements.

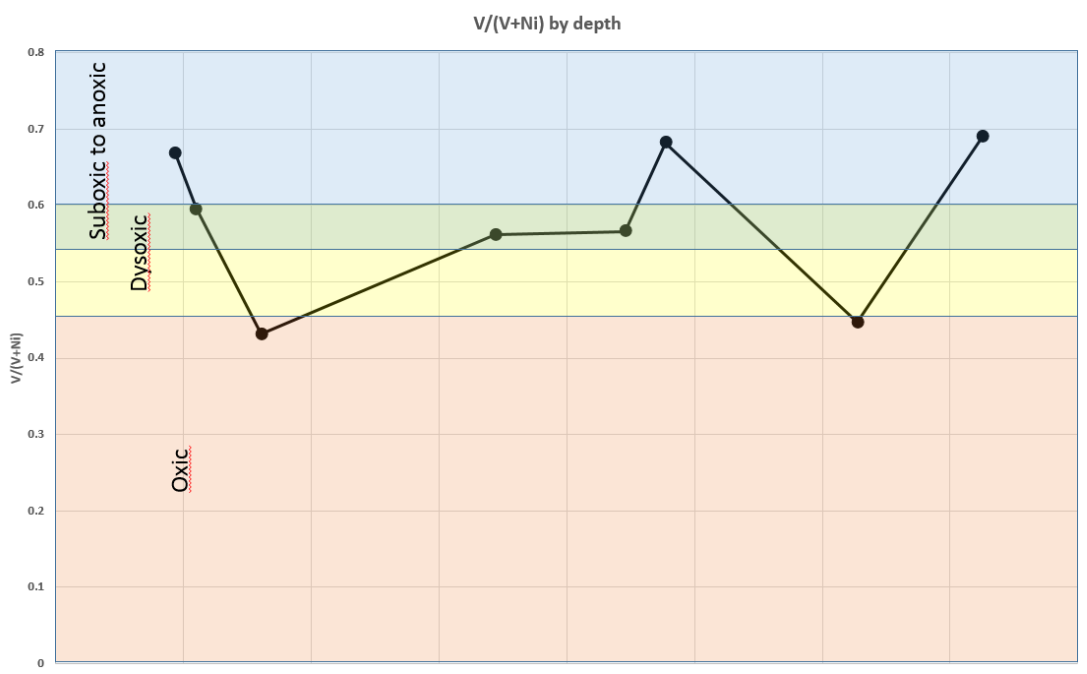

Figure 54- V(V+Ni) by depth showing estimated redox conditions at time of deposition.

By using V/(V+Ni) the redox conditions can be explored. Values of V/(V+Ni) >0.84 represent euxinic conditions, 0.82-0.54 represent anoxic conditions, and 0.60-0.46 represent dysoxic conditions (Rimmer, 2004). V/(V+Ni) ratios in the samples interrogated range from 0.43 to 0.69, suggesting that they formed in oxic to sub/anoxic conditions (Figure 54). While U does not correlate with this redox proxy, Zn, Cr, Cu, and Co all have strong negative correlations with V/(V+Ni) as would be expected. Low V/(V+Ni) values suggest increased oxic conditions that would quickly oxidize metal-bearing minerals in the sediment freeing these elements to concentrate. U does not necessarily correlate with redox conditions and TOC due to a number of reasons. First, if the basin experienced frequent changes in oxygen penetration depth or bottom water oxygen abundance, U signals can be erased through remobilization of U and migration to overlying sediments or the water column (Tribovillard et. al., 2006). Similarly, short anoxic episodes can limit the amount of U stored in organic matter and/or longer periods

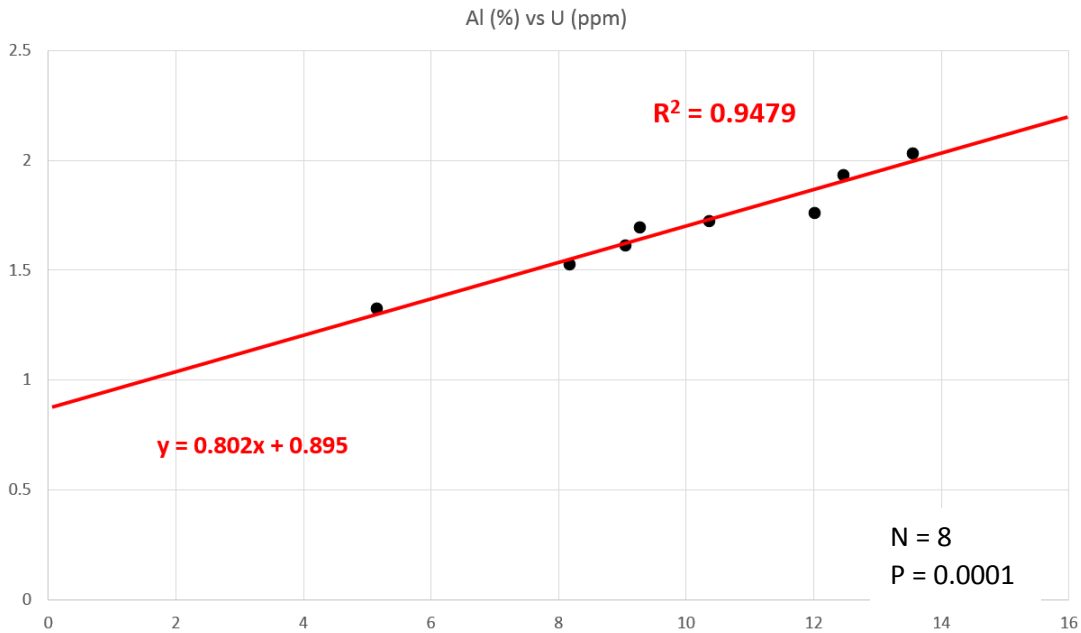

Figure 55- Al (%) to U (ppm) correlation with coefficient of determination.

of higher sedimentation can limit U ability to be stored in significant concentrations.

While TOC does not correlate with any of the trace elements, this can be expected due to the correlation of many of the trace metals with S, suggesting the trace elements are more readily fixed to sulfides than organic matter. Additionally, U shows a very strong positive correlation with Al (Figure 55) suggesting U was deposited at or taken up at a rate similar to siliciclastic flux and is linked to the clay fraction of the samples (Figure 56). Significant portions of the organic matter may have been cooked during diagenesis, producing hydrocarbons. This would increase U/TOC ratios beyond their original depositional condition. Lastly, U tends to positively correlate with TOC in clean shales but these samples have significant quartz and carbonate concentrations making U ineffective as an indicator of TOC.

One possible explanation for why trace elements pair well with Al and silicate

concentrations is by grain-selective sorting of sediment by deposit feeders. These organisms selectively weathering minerals and amorphize trace element hosts altering their concentrations (Harazim et. al. 2015). These trace elements are in turn incorporated into silicates in the absence of organic matter or reactive pyrite. If true, this would further highlight the frequent presence of oxygen at the sediment-water interface, resulting in the oxidation of minerals and trace elements, and the introduction of organisms causing bioturbation.

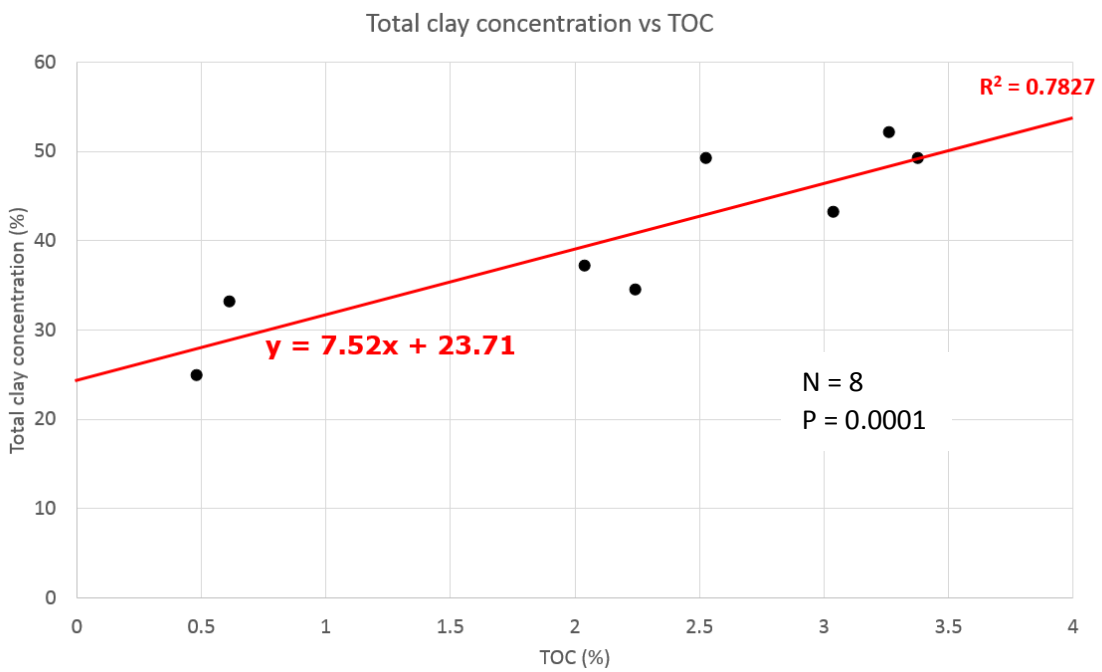

Figure 56- Clay concentration vs TOC with coefficient of determination.

7.4 MICP

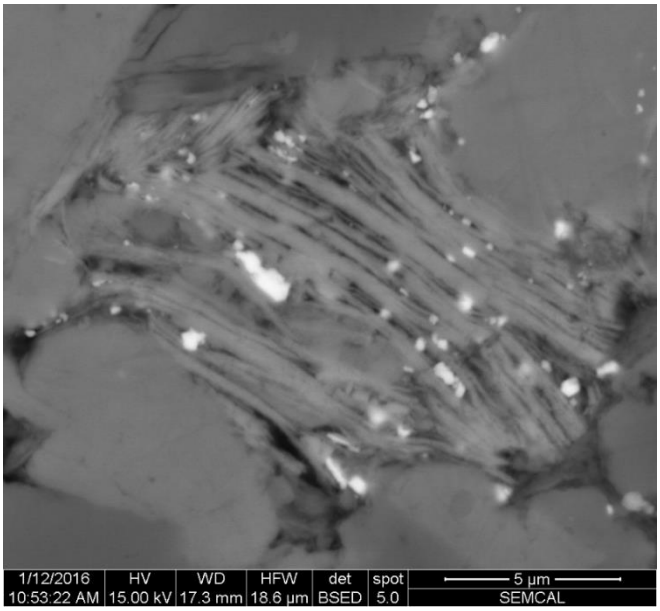

Figure 57- SEM BSE 8492.4 showing clay nanoporosity.

Porosity is a critical variable that impacts the viability of a gas shale. Connected porosity affects permeability, i.e. the ability of the rock to hold and transmit fluids. Hydrocarbon recovery is dependent on the pores, both in terms of quantity and size. Porosity is largely determined by lithology and partially by diagenesis. Larger clastic lithologies result in larger pores and wider pore throats while fine grained clastics, such as shales, tend to have smaller pores and pore throats dominated by clay-bound nanoporosity. These pores exist on the submicron scale between silicate clay minerals, often forming very narrow pores and pore throats (Figure 57).

The eight samples' exhibit strong positive correlations between porosity and clay content and TOC, and moderate positive correlations with quartz content (Figure 58). Porosity also shows a strong negative correlation with carbonate content. This suggests that porosity is mostly a result of clay transformation from smectite and kaolinite to illite and lesser amounts of muscovite and generation of hydrocarbons from organic matter. Conversely, porosity can be isolated by the presence of carbonate, especially large fossiliferous carbonate. The relationship between pore diameter and cumulative porosity reveals that samples with higher TOC and clay concentrations have porosities comprised

of smaller, <100 nm diameter, pores. Samples with higher carbonate content have a smaller portion of porosity being the result of <100 nm diameter pores.

Clay mineral transformation can increase porosity in a number of ways. First, when feldspar is weathered to produce kaolinite, porosity is created due to the reduction in crystal size. Also, the transformation from smectite to illite can create water and acid that can dissolve grains and remove reaction products (Jiang et. al. 2010). These processes create increased secondary porosity.

Clays may add to porosity in other ways as well. Clays tend to coat or wrap other grains, and in the cases of quartz and carbonate, can prevent further cementation and reduction of porosity and permeability. Additionally, the clays themselves may help create micropores, especially during hydrocarbon generation.

Kerogen is known to not only have its own pores but the pore volumes tend to increase with maturation. Organic matter is believed to host the majority of porosity in organic-rich mudstones (Loucks et. al., 2012), and this is especially true with more mature mudstones where organic matter has advanced from kerogen, bitumen, oil, gas, and pyrobitumen. This expulsion of fluid and degradation of organic material creates a secondary porosity on the nanometer scale that has the potential to host extensive oil and gas. Additionally, the presence of oil or gas can prevent further porosity loss through compaction by resisting compression of overburden through overpressuring of the reservoir. Similar to the smectite to illite transition of clays, the breakdown of organic matter creates oxidizing fluids that can create secondary porosity through mineral dissolution. These reasons explain the strong correlation between porosity, clay, and TOC.

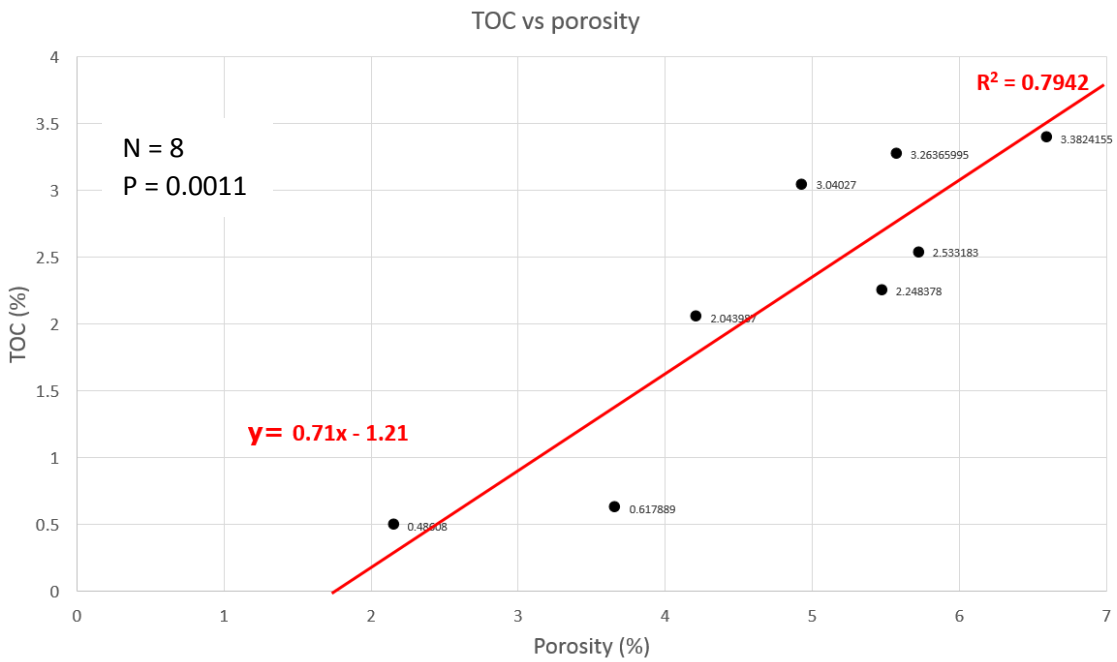

Figure 58- TOC vs porosity suggesting organics contain a portion of porosity.

8. Future work

This study provides new insight into the PPLT petrophysical, geochemical, and mineralogical character. It is limited both in accuracy and regional extent, however. Additional samples from the Utica and adjacent formations from separate wells should be sampled and analyzed using similar methods to provide a basin-wide picture of these formations that include lateral as well as vertical observations.

In this study, XRD was run on subsamples and bulk samples for each depth, but were only run once per depth. Additional samples from the same depths could be run to improve confidence in the results. Additionally, semi-quantitative analysis from XRD data only gives an estimation of mineral concentrations with limited accuracy. Using a method called Rietveld refinement, more accurate mineral concentrations can be obtained. Lastly, the mounts used in this study were random orientation mounts meaning clay minerals were more difficult to characterize and quantify. Using oriented mounts by glycolating samples ensures x-rays analyze clays in the 001 direction, providing more accurate identification of clay minerals by artificially increasing the intensity of the diffraction peaks. This can be especially useful in determining the smectite-illite-muscovite ratios, as well as determining the presence of chlorite and kaolinite.

XRF was run only on bulk samples, without additional subsampling of lithologies. XRF analysis on subsampled rock to distinguish variations in redox sensitive

element concentrations across smaller changes in depth and changes in lithology could demonstrate shorter changes in redox conditions and the effect on mineralogy. Analyzing TOC using the same subsamples could inform on the nature of organic burial as it relates to redox and mineralogy.

XCT provides large density contrasts for vertical core plugs but beyond centimeter scale variations, little information could be interpreted from the data. Analyzing core using micro computed tomography (micro XCT) can provide density and porosity information on the micron scale, making micro XCT a suitable tool for exploring connected porosity, porosity geometry, organic distribution, and clay-sized mineralogical features.

Lastly, while the data from SIMS are convincing with regard to the connections among pyrite morphology, bacterial reduction of sulfate, and redox conditions after deposition, not enough points were sampled of sulfide texture-types as a function of location in the fairway. This is especially true for framboidal pyrite. Additional sulfides should be tested to support the findings of this study.

9. Conclusion

Calcite, clay, and TOC are the controlling factors on porosity and rock fabric. Matrix is dominated by calcite, quartz, illitic-clays, pyrite, albite, chlorite, and phosphate. Calcite and clay show highly negative correlations with one another. Illite and muscovite were originally transformed from smectite, releasing SiO_2, water, and oxidizing fluids that further altered mineral grains and fabric.

Pyrite is found in a number of forms, namely euhedral grains replacing carbonate, large euhedral grains in skeletal carbonate, euhedral tabular and cubic grains in matrix, framboids in matrix, large aggregates of framboids, and reworked framboids. These morphologies show a partition of δ34S values with euhedral having high values for carbonate replacement pyrite and organic bound pyrite. Large euhedral pyrite and matrix bound grains have low δ^{34}S in comparison. Similarly, matrix and carbonate bound framboids have lower δ^{34}S than large aggregates of pyrite. These δ^{34}S values are determined to be partially mediated by sulfate reducing bacteria selectively processing ^{32}S. Matrix euhedral pyrite and large euhedral formed from precursor framboidal pyrite that was easily weathered and oxidized, reforming as a result of fluid migration through connected pores in the matrix. Additionally, δ^{34}S differences can be explained by timing of formation of the pyrite, with later diagenetic changes such as oxidative weathering contributing to the difference.

Redox sensitive trace elements do not correlate well with TOC, although they do correlate well with Al and moderately with clay content and sulfur. This suggests trace elements are fixed to the clay fraction and may have been stripped through oxygenated bottom waters during deposition as well as being fixed to sulfides rather than organic matter.

Connected porosity is dominated by small, <100 nm diameter pores that are interpreted as secondary porosity in clay and organics. The transformation of smectite to illite causing acidic dissolution of mineral grains as well as the maturation of kerogen increased secondary porosity even as primary intergranular porosity was lost due to compaction and overburden.

These factors suggest samples formed under variable redox conditions, with bottom waters that frequently contained significant oxygen followed by numerous abrupt reducing, anoxic episodes. These changes in redox conditions are interpreted as due to changing bottom water currents, changes in sea level due to subsidence and build up of the Trenton limestone platform, and changes in sedimentation and organic rain rate. While the conventional model for organic rich gas shales being the product of anoxia may still be true, this study suggests that euxenia/anoxia may be less of a requirement for the preservation of organic material and formation of a source rock than previously thought.

References

Algeo, T. J., Maynard, B. “Trace-element behavior and redox facies in core shales of Upper Pennsylvanian Kansas-type cyclothems” Chemical Geology 206 (2004) 289 – 318. 2003.

Boyer, C.; Clark, B.; Jochen, V.; Lewis, R.; “Shale Gas: A Global Resource” *Oilfield Review*, 23, no. 3. Schlumberger. 2011.

Bazylinski, D.A. and Moskowitz, B.M. “Microbial biomineralization of magnetic iron minerals: microbiology, magnetism and environmental significance.” Mineralogical Society of America Reviews in Mineralogy, 35, 181–223. 1997.

Chatellier, J. D., Moslow, T. F., Haverslew, B.,. “The use of X-Ray Fluorescence for Sequence Stratigraphy and Geomechanics of Shale” Datapages/Search and Discovery Article #90224 GeoConvention © 2014, FOCUS - Adapt, Refine, Sustain Calgary, Alberta, Canada, May 12-16, 2014

Croudace, I/ W., Rothwell, R. G. *Micro-XRF Studies of Sediment Cores: Applications of a non-destructive tool for the environmental sciences*. 2015.

Ehya, F.; Shakouri, B.; Rafi, M. “Geology, mineralogy, and isotope (Sr, S) geochemistry of the Likak celestite deposit, SW Iran” *Carbonates and Evaporites*, Volume 28, Issue 4, pp 419-431. 2013.

Glombitza, C.; Stockhecke, M.; Schubert, C. J.; Vetter, A.; Kallmeyer, J. “Sulfate reduction controlled by organic matter availability in deep sediment cores from the saline, alkaline Lake Van (Eastern Anatolia, Turkey.” Frontiers in Microbiology 4:209. 2013.

Harazim, D.; McIlroy, D.; Edwards, N. P.; Wogelius, R. A.; Manning, P. L.; Poduska, K. M.; Layne, G. D.; Sokaras, D.; Alonso-Mori, R.; Bergmann, U. “Bioturbating animals control the mobility of redox-sensitive trace elements in organic-rich mudstone” *Geology* v. 44 no. 4. 2015.

Hawkins, S.; Rimmer, S. “Pyrite framboid size and size distribution: Indicators of anoxia” 18th Annual Meeting Abstracts and Program. The Society for Organic Petrology (TSOP). 2001

Jahren, J.; Thyberg, B.; Marcussen, Ø.; Winje, T.; Bjørlykke, K.; Faleide, J. “From Mud to Shale: the Role of Microquartz Cementation” American Association of Petroleum Geologists, Search and Discovery Article #50206, 2009.

Jiang, S., Wang, H., Cai, D.,et al., “The secondary porosity and permeability characteristics of Tertiary strata and their origins, Liaodong Bay Basin, China”. Energy, Exploration & Exploitation. 28(4): 207-222. 2010.

Jørgensen B. B. (1977) The sulfur cycle of a coastal marine sediment (Limfjorden, Denmark). *Limnol. Oceanogr.* 22 814–83210.4319/lo.1977.22.5.0814

Judd, A.; Hovland, M. *Seabed Fluid Flow: The Impact on Geology, Biology and the Marine Environment*. Cambridge University Press. 2009.

Klug, C.; Hagdorn, H.; Montenari, M. “Phosphatized Soft-Tissue in Triassic Bivalves” Palaeontology 48: 833. 2005.

Kohn, M. J; Riciputi, L. R.; Stakes, D.; Orange, D. L. “Sulfur isotope variability in biogenic pyrite: Reflections of heterogeneous bacterial colonization?” American Mineralogist, Volume 83, p. 1454-1468. 1998.

Krajewski, K. P. “Organic matter- apatite-pyrite relationships in the Botneheia Formation (Middle Triassic of eastern Svalbard: Relevance to the formation of petroleum source rocks in the NW Barents Sea shelf” Marine and Petroleum Geology 45, p. 69-105. 2013

Lash, G. G. “Pyritization induced by anaerobic oxidation of methane (AOM)- An example from the upper Devonian shale succession, western New York, USA” Marine and Petroleum Geology 2015, http://dx.doi.org/10.1016/j.marpetgeo.2015.10.002

Loucks, R.G.; Reed, R.M.; Ruppel, S.C.; Hammes, U. “Spectrum of pore types and networks in mudrocks and a descriptive classification for matrix-related mudrock pores” American Association of Petroleum Geologists Bulletin, 96, pp. 1071–1098. 2012.

Maliva, Robert G. and Siever, Raymond. “Mechanism and Controls of Silicification of Fossils in Limestones” The Journal of Geology, Volume 96, Number 4. p. 387-398

Marin-Carbonn, J.; Rollion-Bard, C.; Bekker, A.; Rouxel, O.; Agangi, A.; Cavalazzi, B.; Wohlgemuth-Ueberwasser, C. C.; Axel, H.; McKeegan, K. D. “Coupled Fe and S isotope variations in pyrite nodules from Archean shale” Earth and Planetary Science Letters 392 (2014) 67-79.

Morris, K. A., Sheppard, C. M. “The Role of Clay Minerals in Influencing Porosity and Permeability Characteristics in the Bridport Sands of Wytch Farm, Dorset” *Clay Minerals.* The Mineralogical Society. 1982. 17, 41-54.

Nishizawa1, M.; Maruyama, S.; Urabe, T.; Takahata, N.; and Sano, Y. “Micro-scale (1.5mm) sulphur isotope analysis of contemporary and early Archean pyrite” Rapid Communications in Mass Spectrometry. 2010; 24: 1397–1404. 2010.

Notholt, A. J. G.; Sheldon, R. P.; Davidson, D. F.; *Phosphate Deposits of the World: Volume 2, Phosphate Rock Reserouces*. Cambridge University Press. p. 8. 2005.

Patchen, Douglas G., John B. Hickman, David C. Harris, James A. Drahozval, Paul D. Lake, Langorne B. Smith, Richard Nyahay, Rose Schulze, Ronald A. Riley, Mark T. Baranoski, Larry H. Wickstrom, Christopher D. Laughrey, Jaime Kostelnik, John A. Harper, Katharine L. Avary, John Bocan, Michael E. Hohn, and Ronald McDowell. *A Geologic Play Book for Trenton-Black River Appalachian Basin Exploration*. Rep. Morgantown: West Virginia University Research Corporation, 2006. Print.

Pi,D.-H.,etal.,Trace and rare earth element geochemistry of black shale and kerogen in the early Cambrian Niutitang Formation in Guizhou province, South China: Constraints for redox environments and origin of metal enrichments.PrecambrianRes. 2011
Roy, David C.,Skehan, James William. “The Acadian Orogeny: Recent Studies in New England, Maritime Canada, and the Autochthonous Foreland”, Issue 275. Geological Society of America. 1993. Print.

Rimmer, S. “Geochemical paleoredox indicators in Devonian-Mississippian black shales, Central Appalachian Basin (USA)”. Chemical Geology, 373-391. 2004.

Rye RO, Bethke PM, Wasserman MD The stable isotope geochemistry of acid sulfate alteration. Econ Geol 87:225-262, 1992.

Sageman, Bradley B; Murphy, Adam E.; Wernec, Josef P.;Ver Straetend, Charles A.; Hollander, David J.; Lyons, Timothy W. “A tale of shales: the relative roles of production, decomposition,
and dilution in the accumulation of organic-rich strata, Middle–Upper Devonian, Appalachian basin” Chemical Geology 195 (2003) 229 – 273. 2002.

Schumacher, B.A. “Methods for the Determination of Total Organic Carbon (TOC) in Soils and Sediments”, EPA/600/R-02/069 (NTIS PB2003-100822), U.S. Environmental Protection Agency, Washington, DC, 2002.

Schumacher, G., Mott, B., Angle, M., 2013, Ohio’s Geology in Core and Outcrop —A Field Guide for Citizens and Environmental and Geotechnical Investigators, State of Ohio Department of Natural Resources, Division of Geologic Survey, Information Circular 63, Columbus, OH, USA.

Seal II, Robert R., "Sulfur Isotope Geochemistry of Sulfide Minerals" (2006). USGS Staff -- Published Research. Paper 345. http://digitalcommons.unl.edu/usgsstaffpub/345

Schieber, Jürgen and Baird, Gordon. “On the Origin and Significance of Pyrite Spheres in Devonian Black Shales of North America.” Journal of Sedimentary Research, Vol. 71, No. 1, p. 155-166. 2001.

Sondergeld, C. H., R. J. Ambrose, C. S. Rai, and J. Moncrieff, Microstructural studies of gas shales: Presented at SPE Unconventional Gas Conference, SPE 131771. 2010

Swanson, Vernon E. *Oil Yield and Uranium Content of Black Shales* U.S. Geological Survey Professional Paper 356-A p. 90-91.

Tribovillard, N., Algeo, T.J., Lyons, T., and Riboulleau, A. “Trace metals as paleoredox and paleoproductivity proxies: an update.” Chemical Geology 232 p.12-32. 2006.

Tyson, R. V. *Sedimentary Organic Matter: Organic facies and palynofacies*. p.122-124, Springer Science & Business Media. 1995.

van de Kamp, Peter C. “Smectite-Illite-Muscovite Transformations, Quartz Dissolution, and Silica Release in Shales.” Clays and Clay Minerals, Volume 56, Number 1, pp. 66-81(16). 2008.

Webb, Paul A. “An Introduction To The Physical Characterization of Materials by Mercury Intrusion Porosimetry with Emphasis On Reduction And Presentation of Experimental Data” Micromeritics Instrument Corp. January 2001.

Wedepohl, K.H., “Environmental influences on the chemical composition of shales and clays.” Phys. Chem. Earth 8, p. 307 – 331. 1971.

Wedepohl, K.H. *Handbook of Geochemistry* Springer. Verlag, Berlin. 1978.

Wickstrom, Larry; Perry, Chris; Erenpreiss, Matthew; Riley, Ron. “The Marcellus and Utica Shale Plays in Ohio” Ohio Oil & Shale Association Meeting, 2011.

Wilkin, R.T. and Barnes, H.L. “Formation processes of framboidal pyrite.” Geochimica et Cosmochimica Acta, 61, 323–339. 1997.

Willan, Christopher., McCallum, Scott., Warner, Travis. “Regional Interpretation of the Middle-Upper Ordovician Utica Shale Play in the Appalachian Basin” American Association of Petroleum Geologists, Article #80239. 2012.

Appendix: Additional Figures

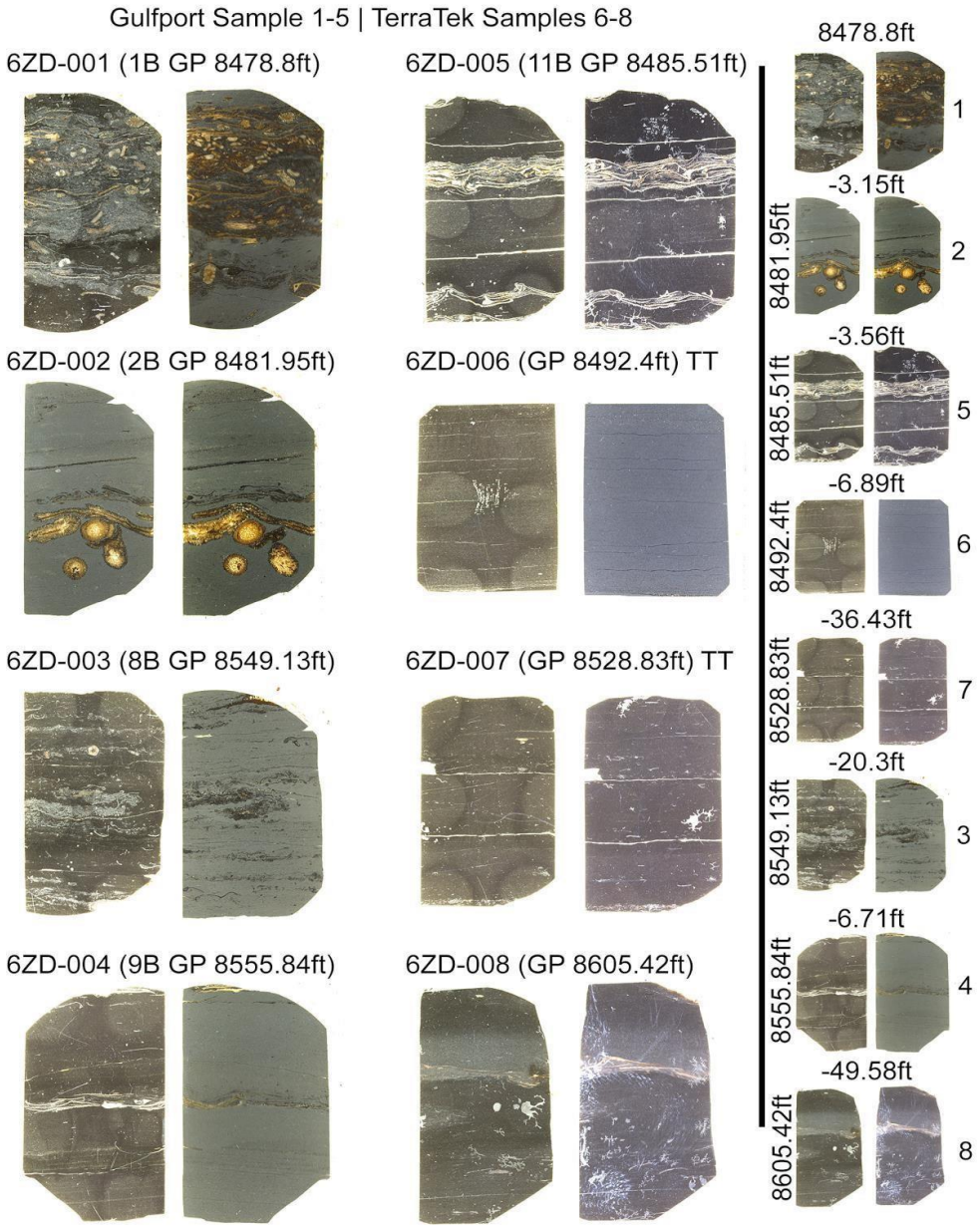

Figure 59- All eight Gulfport thick sections and depths, Leica optical microscope.

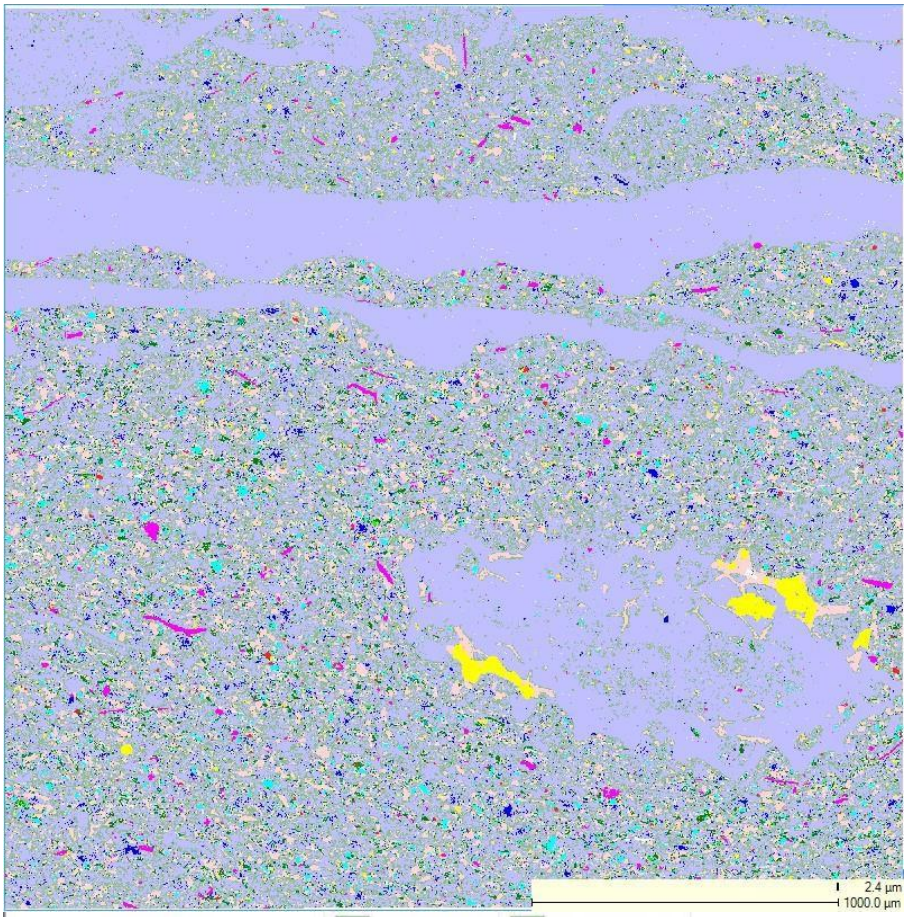

Mineral Name	area(Mineral)	area percent
Background	23148	1.63385614188884
Quartz	138677	9.78824383051319
K_Feldspar	4115	0.29044919750616
Feldspar_Albite	17164	1.21148724811561
illite/muscovite	38551	2.72104666173997
K Mg Fe Phyllosilicate	1132	0.0798999979530919
Chlorite	1382	0.0975457572183507
Apatite	10948	0.772743089744214
Dolomite	21017	1.48344368991178
Calcite	866197	61.1388149531576
Pyrite	15513	1.09495465392784
Other Silicates	2134	0.150624201088249
Others	1579	0.111450615519375
Rutile/Anatase	2263	0.159729412869123
Trap Definitions	828	0.0584427546865372
Kaolinite	583	0.0411499106065836
CaCO3 - Si Boundary 1	272976	19.2674751247732
CaCO3 - Si Boundary 2	21712	1.5324989006692

Figure 60- QEMSCAN, Gulfport 1-B, with mineral legend. Noticeable features include bryozoan fossil in bottom right corner (calcite and pyrite), large calcitic mollusk fossils spanning the top half of the field, and quartz/clay/calcite matrix with noticeable 30 micron round pyrite in bottom left corner.

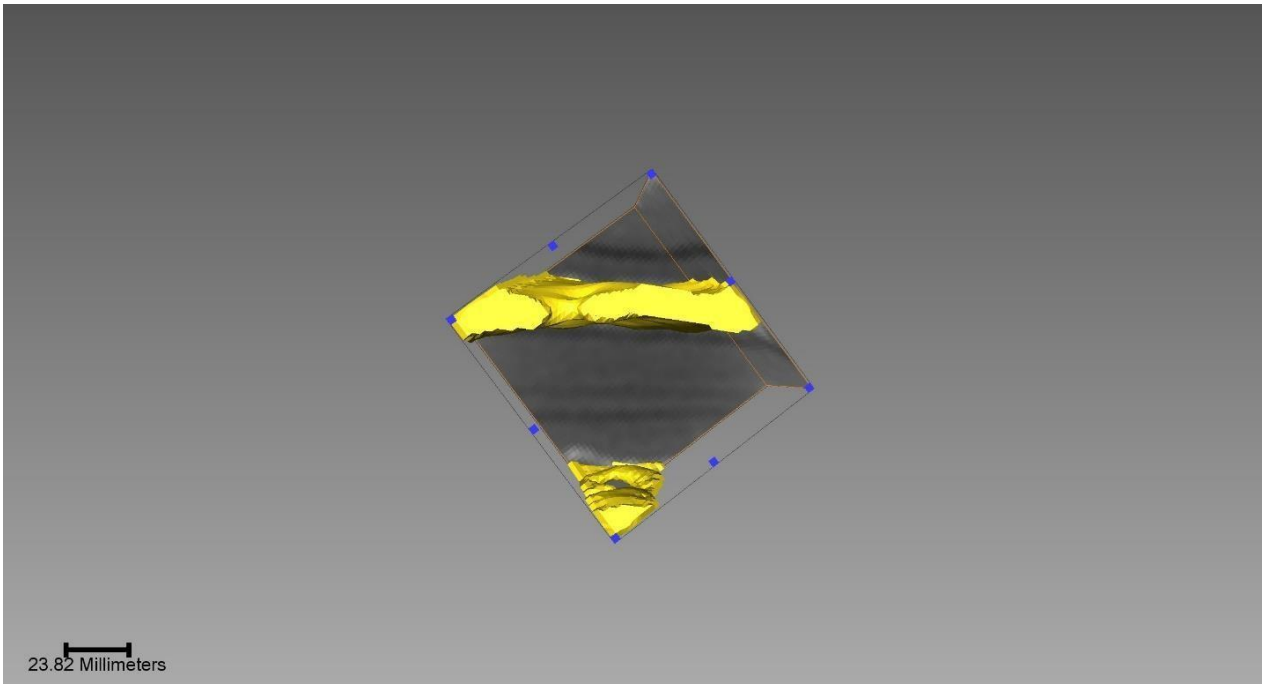

Figure 61- 11B Highlighted in yellow is a high density hummocky band that is likely fossiliferous and carbonate in origin, indicating a change in the depositional conditions across this zone.

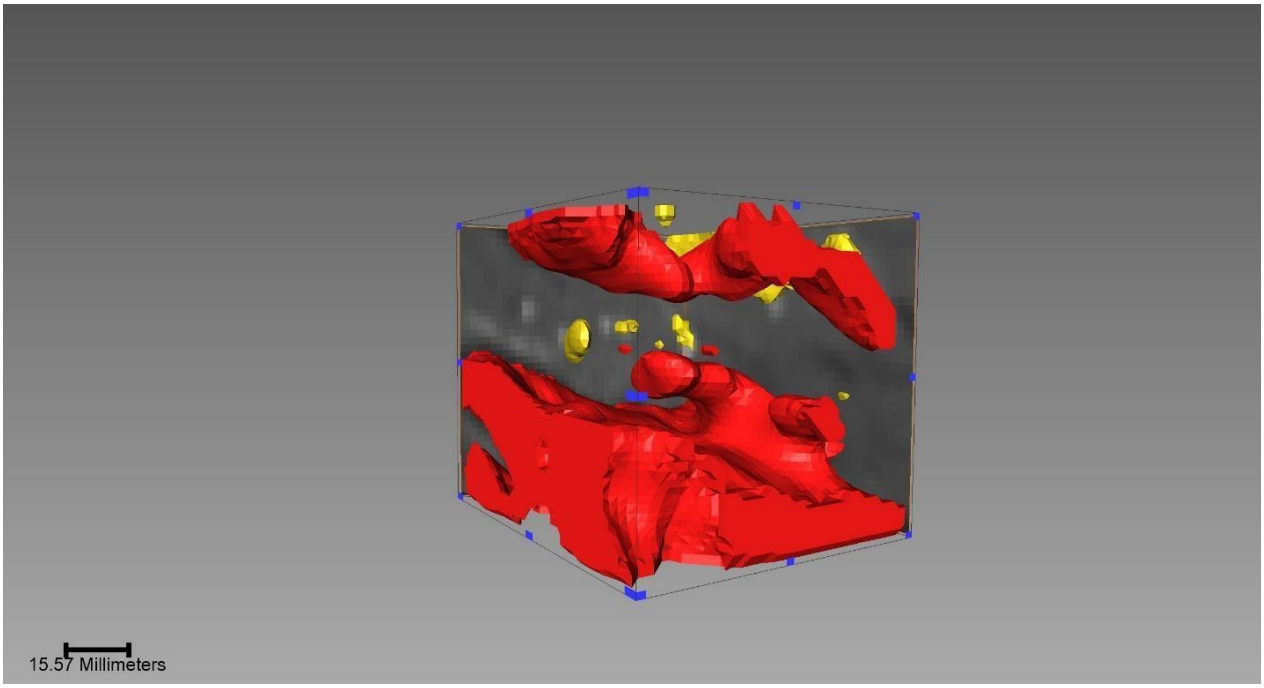

Figure 62- 1B showing irregular clay and organic layers (red) and high density minerals (yellow)

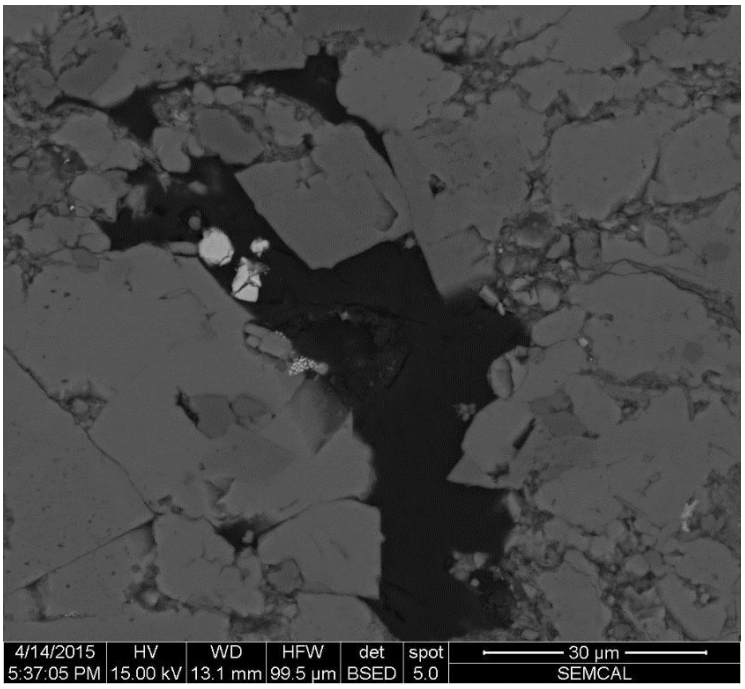

Figure 63- SEM BSE. Framboidal pyrite in organic, calcite and quartz matrix, Gulfport 1B.

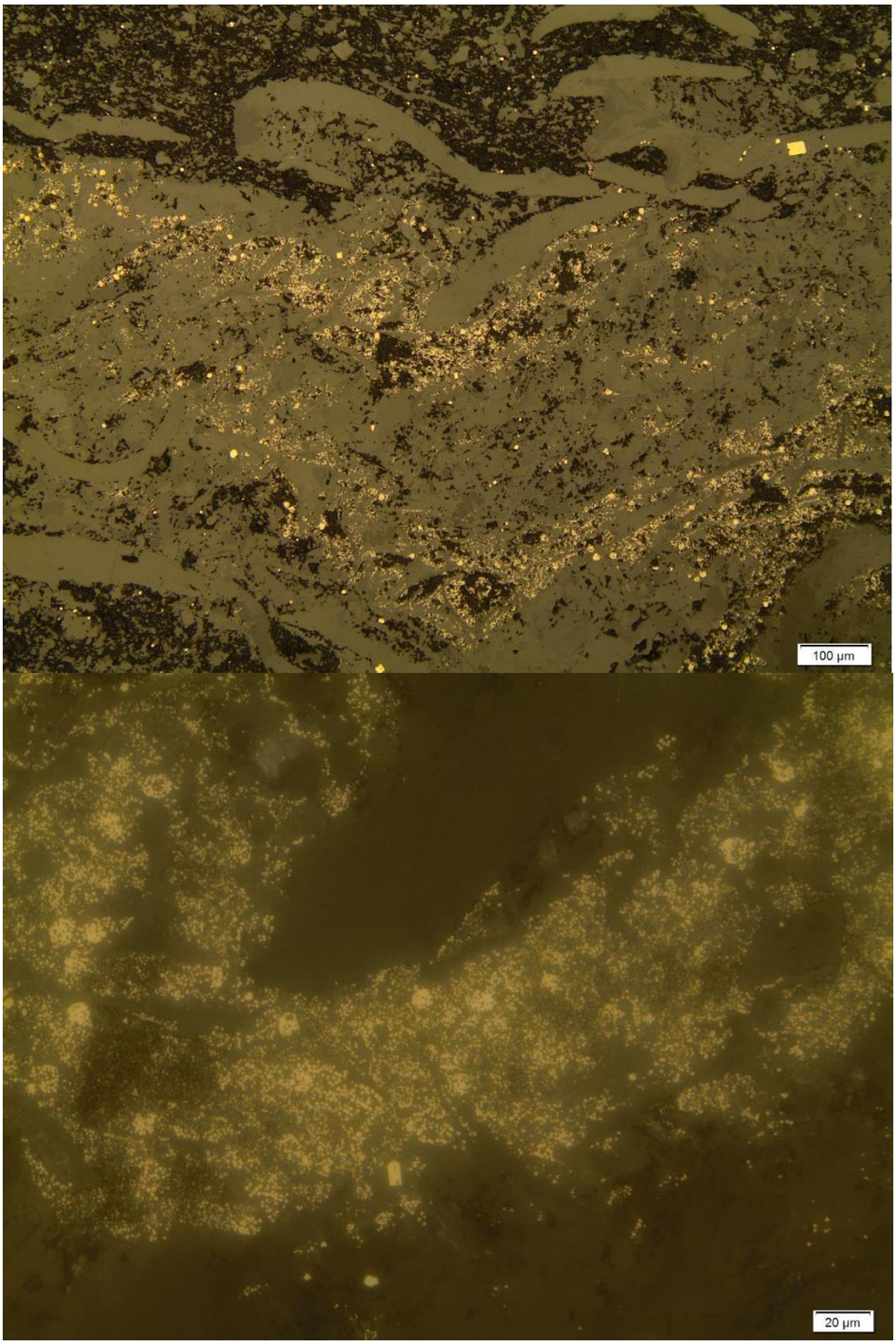

Figure 64- Framboidal pyrite in organic matter between fossiliferous carbonate, Gulfport 8B 8549.13, Leica optical microscope, reflected light, 10X and 40X.

SIMS data				1= Euhedral			
				2= framboidal			
				3= other			
Sample	**Mineral**	**δ34S**	**1σ (‰)**	**Morphology**	**Depth**	**Other morph description**	**+/- avg**
1B-0-1	Pyrite	-14.9	0.3	2.0	8478.8	frambs	-20.3
1B-1-1	Pyrite	5.7	0.3	1.0	8478.8	carbonate replacement bryozoan	0.3
1B-1-2	Pyrite	6.4	0.3	3.0	8478.8	SNOWBALL	1.0
1B-3-1	Pyrite	7.9	0.3	1.0	8478.8	carb replacement	2.5
1B-3-2	Pyrite	9.3	0.3	1.0	8478.8	carb replacement	3.9
1B-4-1	Pyrite	4.6	0.3	1.0	8478.8	thin carb matrix replacement	-0.8
1B-5-1	Pyrite	14.8	0.3	1.0	8478.8	tabular in clay matrix	9.4
1B-9-1	Pyrite	6.2	0.3	1.0	8478.8	small in matrix	0.8
1B-10-1	Pyrite	15.7	0.3	1.0	8478.8	heavily weathered in clay/org	10.3
1B-11-1	Pyrite	-3.9	0.3	2.0	8478.8	framb	-9.3
1B-12-1	Pyrite	5.6	0.3	1.0	8478.8	bryozoan carb replace	0.1
1B-12-2	Pyrite	6.5	0.3	1.0	8478.8	bryozoan carb replace	1.1
1B-12-3	Pyrite	6.3	0.3	1.0	8478.8	bryozoan carb replace	0.9
	AVERAGE	5.4					
	Euhedral avg	8.3					
	framb average	-9.4					
	other average	6.4					

Continued

Figure 65- Raw SIMS data

Figure 65: Continued

8B-01-01	Pyrite	19.7	0.3	1.0	8549.13	in crinoid	5.48855053952559
8B-02-01	Pyrite	22.7	0.3	**1**.0	8549.13	cluster	8.49192365451880
8B-03-01	Pyrite	6.5	0.3	1.0	8549.13	looks more like marcasite	-7.68851960882198
8B-04-01	Pyrite	5.5	0.3	1.0	8549.13	looks more like marcasite	-8.72058775944682
8B-05-01	Pyrite	16.6	0.3	2.0	8549.13	large aggregate	2.42863317422439
	AVERAGE	14.2					
	Euhedral avg	13.6					
	framb average	16.6					
	other average	na					
S8606-01-01	Pyrite	1.9	0.3	2.0	8605.8		-10.6444800308627
S8606-02-01	Pyrite	16.8	0.3	1.0	8605.8	in fracture	4.1730653691243
S8606-02-02	Pyrite	9.1	0.3	1.0	8605.8	in matrix	-3.4483088136799
S8606-03-01	Pyrite	22.2	0.3	1.0	8605.8	fracture	9.6217008152728
S8606-04-01	Pyrite	24.7	0.3	3.0	8605.8	cluster	12.1411726849683
S8606-05-01	Pyrite	0.7	0.3	2.0	8605.8	large framb	-11.8431500248228
	AVERAGE	12.6					
	Euhedral avg	16.0					
	framb average	1.3					
	other average	24.7					
Spot-to-spot reproducibility on the pyrite standard = 0.4‰							
2B-10-01	Pyrite	4.8	0.3	1.0	8481.9	euh carb replace	-6.67885502049253

Continued

Figure 65: Continued

2B-10-02	Pyrite	5.4	0.3	1.0	8481.9	euh carb replace	-6.06050696579967
2B-6-01	Pyrite	-18.7	0.3	2.0	8481.9	clustered, relict framb	################
2B-8-01	Pyrite	20.7	0.3	1.0	8481.9	weathered carb replace	9.17803378751165
2B-7-01	Pyrite	22.0	0.3	1.0	8481.9	weathered round carb replace	10.48765375958090
2B-9-01	Pyrite	21.4	0.3	1.0	8481.9	weathered round carb replace	9.92972833396883
2B-4-01	Pyrite	6.3	0.3	1.0	8481.9	large euhedral	-5.16666876319076
2B-4-02	Pyrite	6.0	0.3	1.0	8481.9	large euhedral	-5.47387500376611
2B-2-01	Pyrite	17.1	0.3	1.0	8481.9	euh carb replace, crinoid	5.62272925170555
2B-3-01	Pyrite	19.3	0.3	1.0	8481.9	carb replace, pellet	7.81215826422905
2B-1-01	Pyrite	22.1	0.3	1.0	8481.9	euh carb replace, crinoid	10.55270647518100
	AVERAGE	11.5					
	Euhedral avg	14.5					
	framb average	-18.7					
	other average	na					
Sample Average	9.80857						
euhedral	12.237						
framb	-3.05						
other	15.55						

SIMS spot location images

1B locations

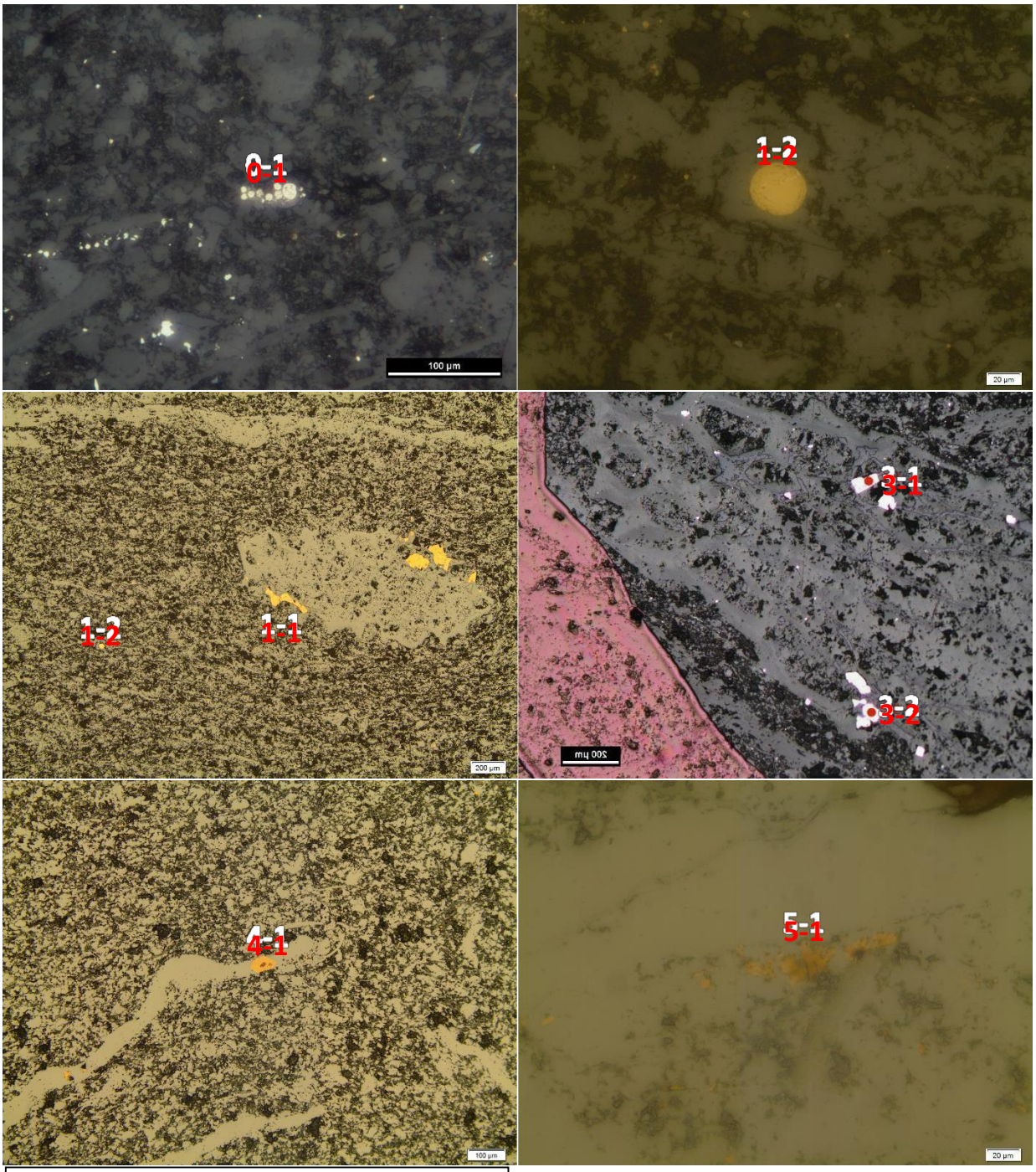

Figure 66- 1B SIMS spot locations

Continued

Figure 66: Continued

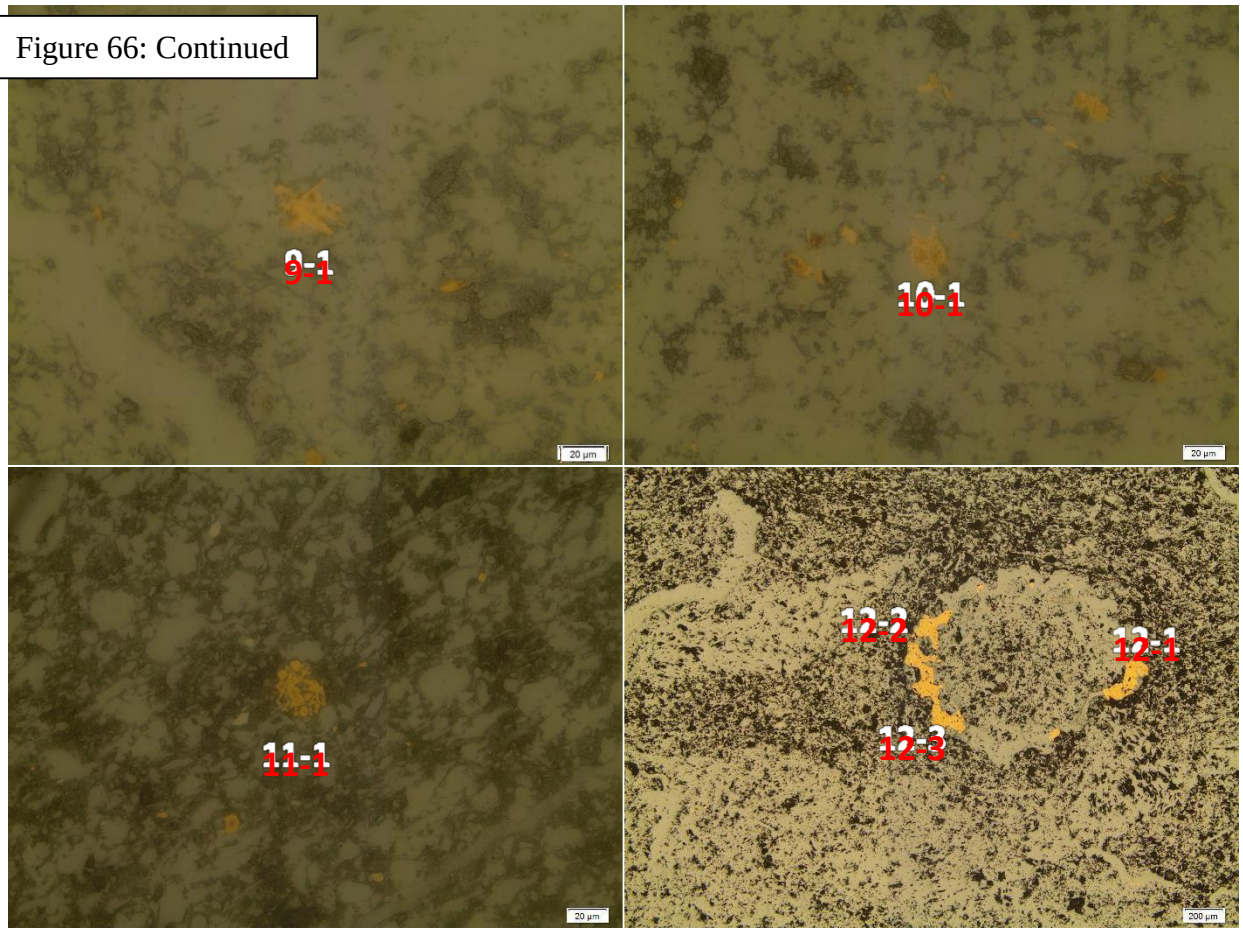

8B locations

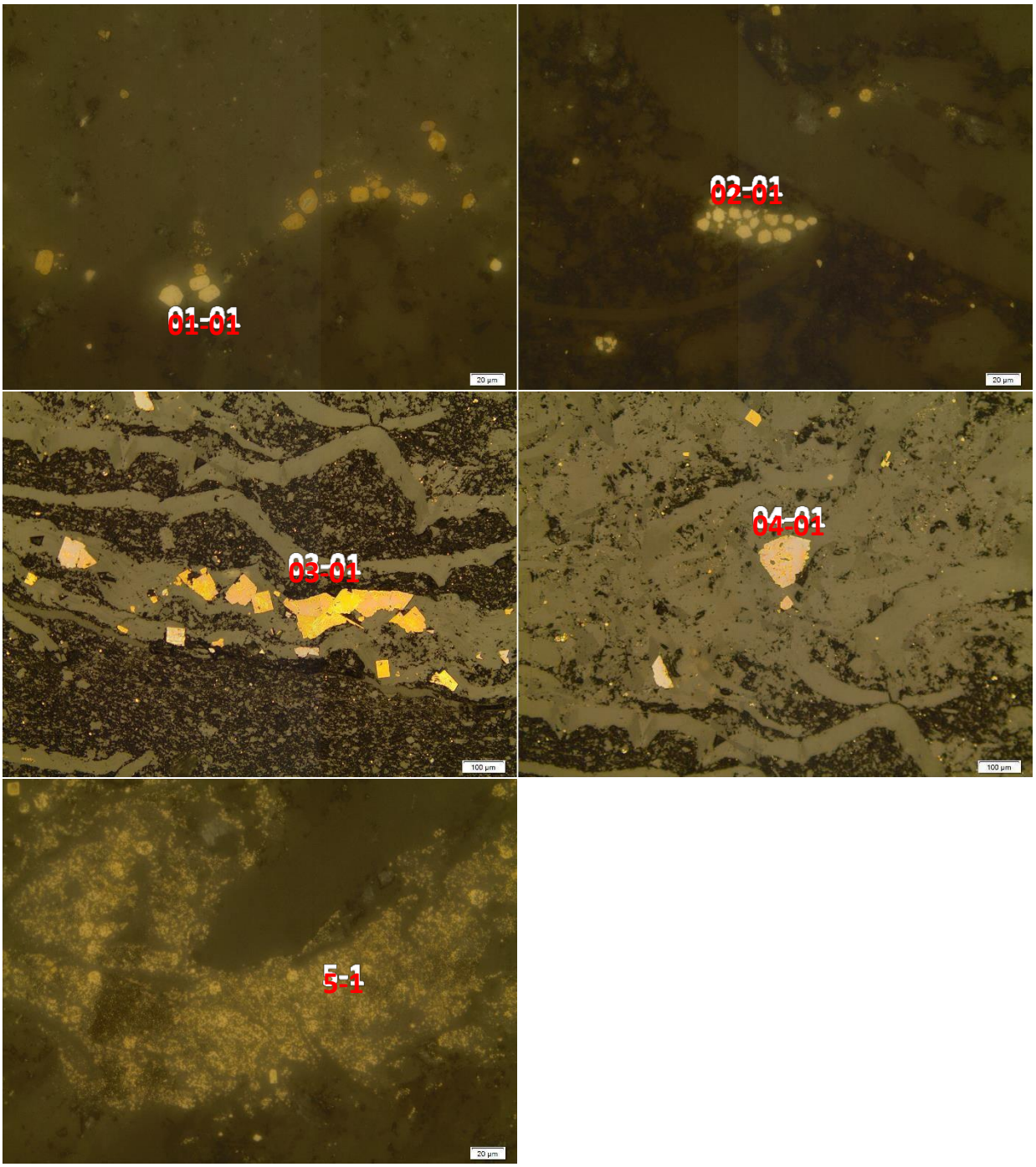

Figure 67- 8B SIMS spot locations

8605 locations

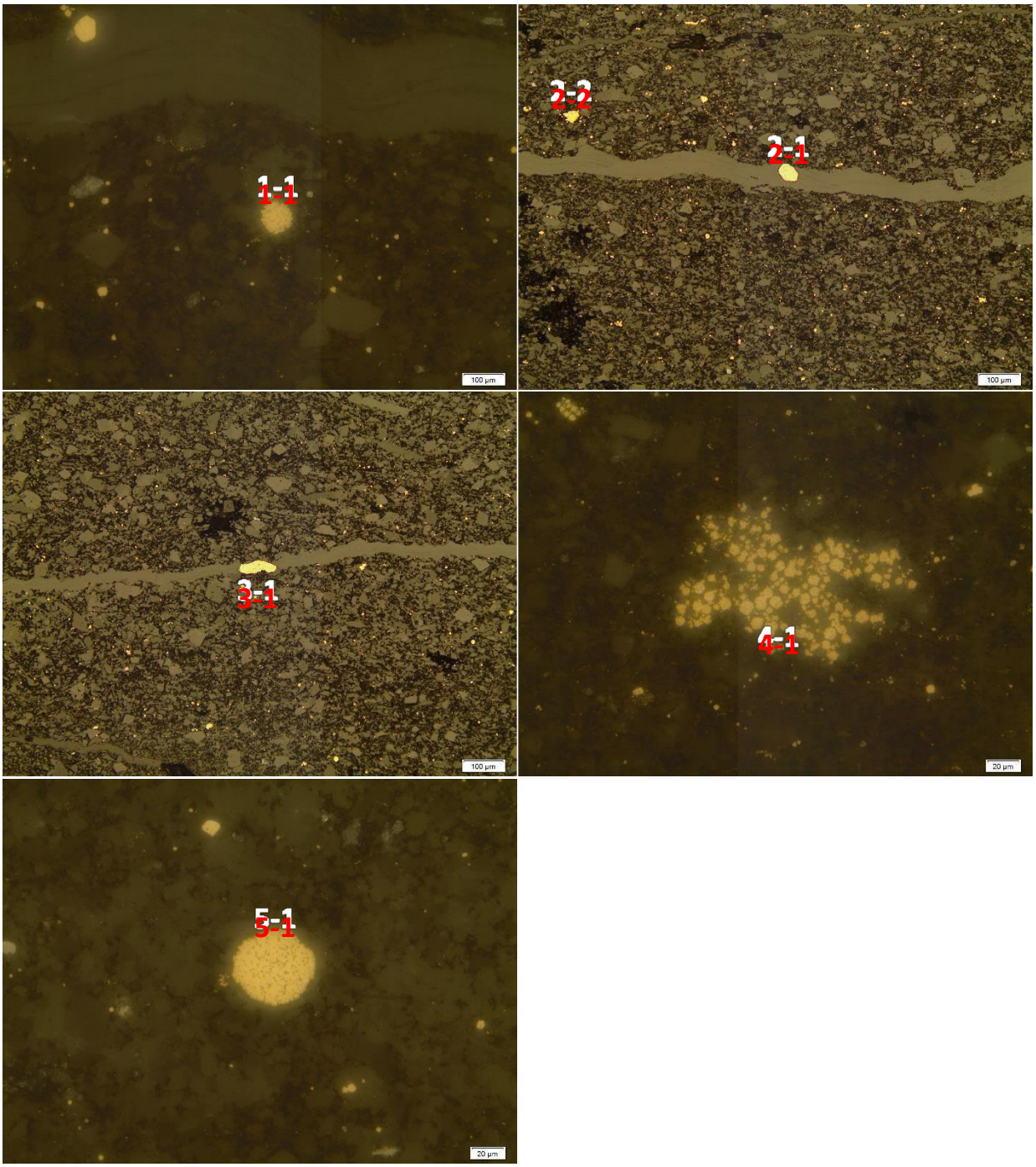

Figure 68- 8605 SIMS spot locations

2B locations

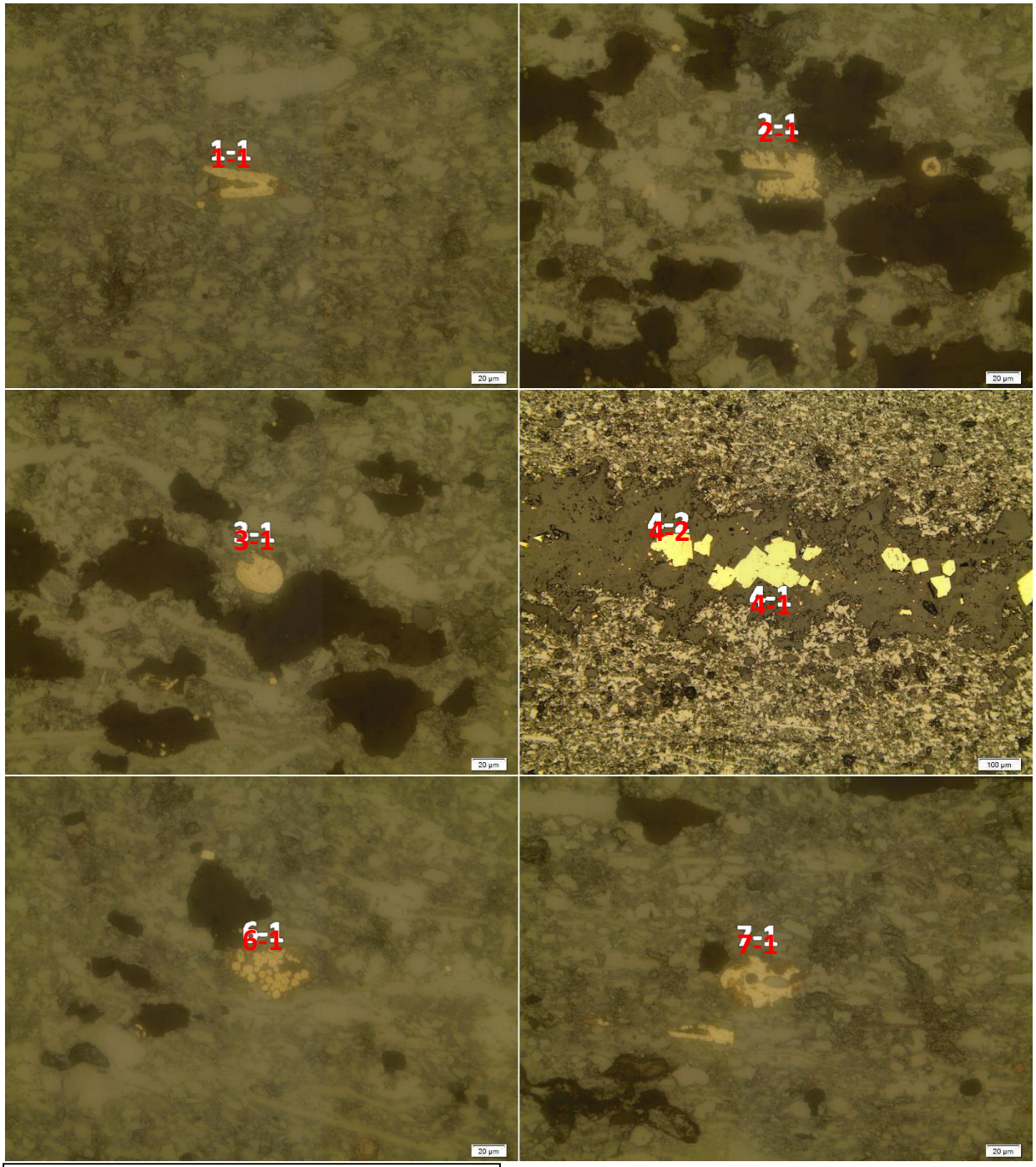

Figure 69- 2B SIMS spot locations

Continued

Figure 69: Continued

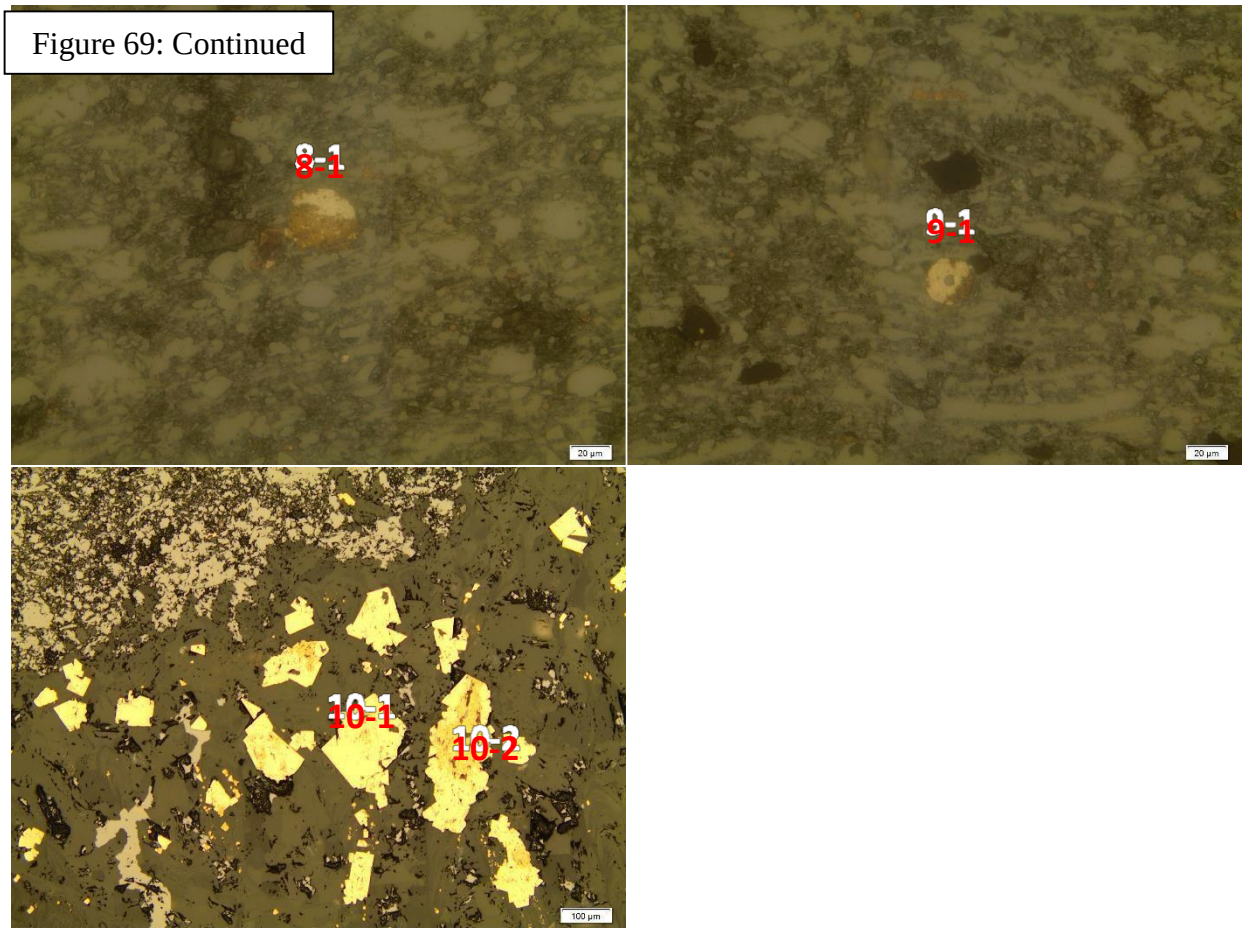

Raw XRF data

sample id	Depth		Al	Si	Fe	Ca	Ti	Mg	Mn	K	Na	P	Ba	Co	Cr	Cu	Ni	Rb	S	Sr	V	Zn	Zr	Th	Ge	Y	Nb	Ta	U
			%	%	%	%	%	%	%	%	%	%	ppm	ppm	ppm	ppm	ppm	ppm	ppm	ppm	ppm	ppm	ppm	ppm	ppm	ppm	ppm	ppm	ppm
1B	8478.8	Concentration	9.287	40.255	3.184	41.057	0.497	3.136	0.074	1.857	0.807	0.384	218.274	6.929	27.473	29.275	26.006	83.101	4064.004	1544.666	54.63	20.344	5.096	5.016	-0.526	21.715	21.04	3.108	1.693
1B	8478.8	Concentration	9.264	40.282	3.181	41.06	0.494	3.136	0.074	1.854	0.814	0.384	213.081	7.037	26.924	29.845	27.751	83.147	4076.706	1546.747	54.029	21.839	5.834	5.037	-0.534	21.357	21.084	3.123	1.698
1B	8478.8	Concentration	9.267	40.234	3.178	40.943	0.494	3.13	0.074	1.853	0.814	0.384	199.863	7.128	28.965	29.182	26.959	83.288	4060.595	1541.361	53.258	21.344	6.054	5.032	-0.548	21.608	21.231	3.126	1.692
2B	8481.95	Concentration	13.569	48.841	4.112	25.636	0.722	2.513	0.061	2.866	0.958	0.486	205.808	11.784	38.455	45.209	47.928	122.392	4583.713	1154.152	71.529	91.731	61.655	6.118	-0.597	27.329	28.457	2.294	2.034
2B	8481.95	Concentration	13.586	48.859	4.102	25.615	0.723	2.503	0.06	2.857	0.953	0.485	203.042	12.856	40.255	44.43	47.775	121.296	4579.453	1156.293	70.738	90.497	61.167	6.109	-0.601	27.375	28.28	2.264	2.027
2B	8481.95	Concentration	13.518	48.809	4.089	25.508	0.717	2.493	0.06	2.846	0.954	0.487	210.308	12.075	41.406	44.207	47.635	120.777	4554.774	1148.043	69.082	89.94	62.477	6.11	-0.616	28.343	28.3	2.296	2.03
8492	8492.2	Concentration	10.313	38.691	4.976	39.204	0.505	1.824	0.066	1.957	0.83	0.705	218.219	14.875	31.859	58.694	81.175	89.768	5726.33	1524.466	60.101	72.184	2.745	5.118	-0.459	24.618	19.455	2.206	1.723
8492	8492.2	Concentration	10.362	38.804	4.993	39.386	0.509	1.916	0.067	1.97	0.826	0.705	218.33	16.844	34.781	59.551	81.064	89.75	5767.698	1523.692	63.436	73.328	1.023	5.157	-0.476	24.258	19.302	2.21	1.719
8492	8492.2	Concentration	10.441	39.079	5.048	39.693	0.531	1.854	0.067	2.015	0.836	0.719	270.923	16.758	38.062	60.634	83.26	90.536	5873.496	1536.906	62.922	72.766	0.53	5.14	-0.483	25.315	19.36	2.196	1.721
8528.83	8528.8	Concentration	12.504	48.976	4.077	27.349	0.623	2.18	0.055	2.522	1.09	0.401	202.552	13.627	37.163	63.518	56.786	108.059	3420.583	1156.294	73.438	78.884	41.386	5.796	-0.711	24.552	22.48	1.696	1.929
8528.83	8528.8	Concentration	12.449	48.778	4.067	27.254	0.621	1.89	0.055	2.508	1.082	0.4	221.257	12.334	37.489	63.194	57.349	109.603	3407.764	1155.9	71.946	79.235	41.858	5.811	-0.726	23.345	22.42	1.658	1.924
8528.83	8528.8	Concentration	12.418	48.817	4.066	27.288	0.621	2.045	0.055	2.514	1.083	0.401	206.505	14.148	36.072	63.324	57	108.988	3419.013	1154.566	73.4	79.16	41.295	5.817	-0.744	24.085	22.578	1.698	1.928
8B	8549.13	Concentration	8.159	30.975	2.724	52.512	0.386	2.861	0.053	1.208	0.677	0.548	189.966	9.994	24.414	51.304	55.993	61.773	-69.404	2524.654	49.905	60.466	-67.368	4.488	-0.454	18.494	27.579	2.6	1.527
8B	8549.13	Concentration	8.162	31.007	2.73	52.593	0.386	2.866	0.054	1.209	0.671	0.55	197.403	10.148	26.506	51.417	56.276	61.082	-75.366	2530.119	49.284	60.354	-69.144	4.495	-0.461	18.763	27.546	2.643	1.527
8B	8549.13	Concentration	8.236	31.068	2.739	52.785	0.39	2.873	0.054	1.216	0.676	0.552	205.963	9.891	25.525	50.803	57.114	61.147	-70.022	2535.856	47.981	60.748	-69.073	4.481	-0.479	18.468	27.705	2.6	1.521
9B	8555.4	Concentration	12.067	34.637	3.521	43.389	0.488	2.613	0.085	2.098	0.805	1.323	271.867	11.18	36.922	39.487	43.243	96.387	1390.191	1744.047	60.672	41.014	-18.809	5.265	-0.559	22.39	21.116	2.823	1.76
9B	8555.4	Concentration	11.989	34.59	3.513	43.359	0.489	2.609	0.084	2.094	0.805	1.327	278.042	10.909	35.207	38.544	43.011	97.029	1390.711	1742.634	60.205	40.241	-17.071	5.254	-0.558	21.884	21.051	2.865	1.755
9B	8555.4	Concentration	12.032	34.631	3.516	43.309	0.488	2.6	0.084	2.099	0.803	1.322	258.115	11.8	36.901	38.604	42.31	96.359	1383.997	1737.764	62.368	39.945	-17.752	5.244	-0.581	22.257	21.101	2.876	1.756
11B	8585.5	Concentration	5.161	19.667	2.388	63.314	0.225	1.609	0.099	0.562	0.508	1.069	160.154	7.771	14.265	30.862	36.846	29.08	6655.883	2540.099	30.786	95.762	-72.475	3.847	-0.345	15.731	21.099	3.395	1.32
11B	8585.5	Concentration	5.139	19.626	2.388	63.308	0.225	1.609	0.099	0.563	0.513	1.069	156.914	7.546	17.636	30.399	37.612	27.791	6635.302	2539.16	29.446	95.579	-72.673	3.833	-0.353	16.368	21.155	3.322	1.319
11B	8585.5	Concentration	5.185	19.696	2.413	63.924	0.23	1.619	0.099	0.568	0.517	1.08	169.816	8.824	17.21	30.585	37.234	29.389	6679.413	2551.739	29.962	96.333	-75.886	3.814	-0.354	15.847	21.001	3.362	1.325
8605	8605	Concentration	8.957	32.083	3.6	50.21	0.481	2.648	0.2	1.765	0.638	0.837	211.625	10.4	22.538	22.915	21.619	76.683	11565.61	1046.116	49.438	31.102	30.125	4.763	-0.601	18.497	9.946	3.504	1.609
8605	8605	Concentration	8.99	32.107	3.607	50.291	0.482	2.642	0.2	1.771	0.643	0.836	208.467	10.933	24.762	22.606	21.11	77.379	11560.34	1047.918	47.747	30.116	29.119	4.775	-0.613	18.172	10.06	3.479	1.616
8605	8605	Concentration	9.251	32.302	3.635	50.669	0.486	2.67	0.203	1.79	0.64	0.844	215.179	11.713	24.91	22.32	22.813	77.008	11655.86	1053.731	48.051	31.812	30.168	4.753	-0.623	18.474	10.011	3.46	1.607

Figure 70- Raw XRF, TOC, Porosity, and XRD data

XRD, porosity, TOC

Sample	depth	% Pyrite	Carbonate	Muscovite+Illite	Dolomite	Albite	Quartz	Chlorite/Clinochlore	Total clay	porosity	TOC
1B	8479	3	32	37	3	4	17	6	43	4.93	3.04027
2B	8482	4	37	27	3	4	18	6	33	3.66	0.617889
8492	8492	2	22	45	3	5	21	4	49	5.72	2.533183
8528.8	8529	2.5	13	45	2	6	25	4	49	6.59	3.382416
8B	8549	4	30.3	30.3	3	6.1	22.2	4	34.3	5.47	2.248378
9	8555	7.9	27.7	20.8	2	16.8	16.8	4	24.8	2.15	0.48608
11B	8586	2	42	32	1	5	13	5	37	4.21	2.043987
8605	8605	5	14	48	5	5	19	4	52	5.57	3.26366

XRF averaged and normalized to Al

Sample		% Al	% Fe	% Ti	% Mn	% Ni/Co	% v/cr	ppm v/v+u	ppm Co	ppm Cr	ppm Cu	ppm Ni	ppm Rb	ppm S	ppm Sr	ppm V	ppm Zn	ppm Th	ppm U/Th	ppm U
1B	8478.8	9.272666667	0.3431	0.053	0.008	3.826	1.942	0.667	0.758	2.997	3.174	2.901575	8.970307	438.6119	166.5387	5.8206	2.28367	0.542274786	0.336957	0.182723
2B	8481.95	13.55766667	0.3025	0.053	0.0045	3.904	1.76	0.596	0.903	2.953	3.291	3.524156	8.960859	337.2739	85.03154	5.1963	6.69161	0.450839623	0.33217	0.149755
8492	8492.2	10.372	0.4826	0.05	0.0064	5.064	1.781	0.432	1.558	3.365	5.749	7.889799	8.678943	558.1541	147.3539	5.9924	7.01498	0.495404294	0.334934	0.165927
8528.8	8528.8	12.457	0.3267	0.05	0.0044	4.267	1.976	0.561	1.073	2.963	5.085	4.579353	8.740735	274.2062	92.76605	5.8544	6.34928	0.466243879	0.331784	0.154692
8B	8549.13	8.185666667	0.3336	0.047	0.0066	5.64	2.888	0.566	1.223	3.113	6.252	6.897544	7.492853	-8.74667	309.1025	8.9895	7.39374	0.548275441	0.339795	0.186301
9B	8555.4	12.02933333	0.2923	0.041	0.007	3.794	2.521	0.681	0.939	3.021	3.232	3.562514	8.029677	115.4095	144.7696	7.6166	3.35846	0.436793394	0.334391	0.14606
11B	8585.5	5.161666667	0.4643	0.044	0.0192	4.627	1.837	0.447	1.559	3.172	5.931	7.212916	5.570552	1289.674	492.7994	5.8246	18.5776	0.74226671	0.344876	0.25599
8605	8605	9.066	0.3986	0.053	0.0222	1.983	2.011	0.689	1.215	2.655	2.494	2.40981	8.495845	1278.837	115.7352	5.34	3.42047	0.525443047	0.338115	0.17766

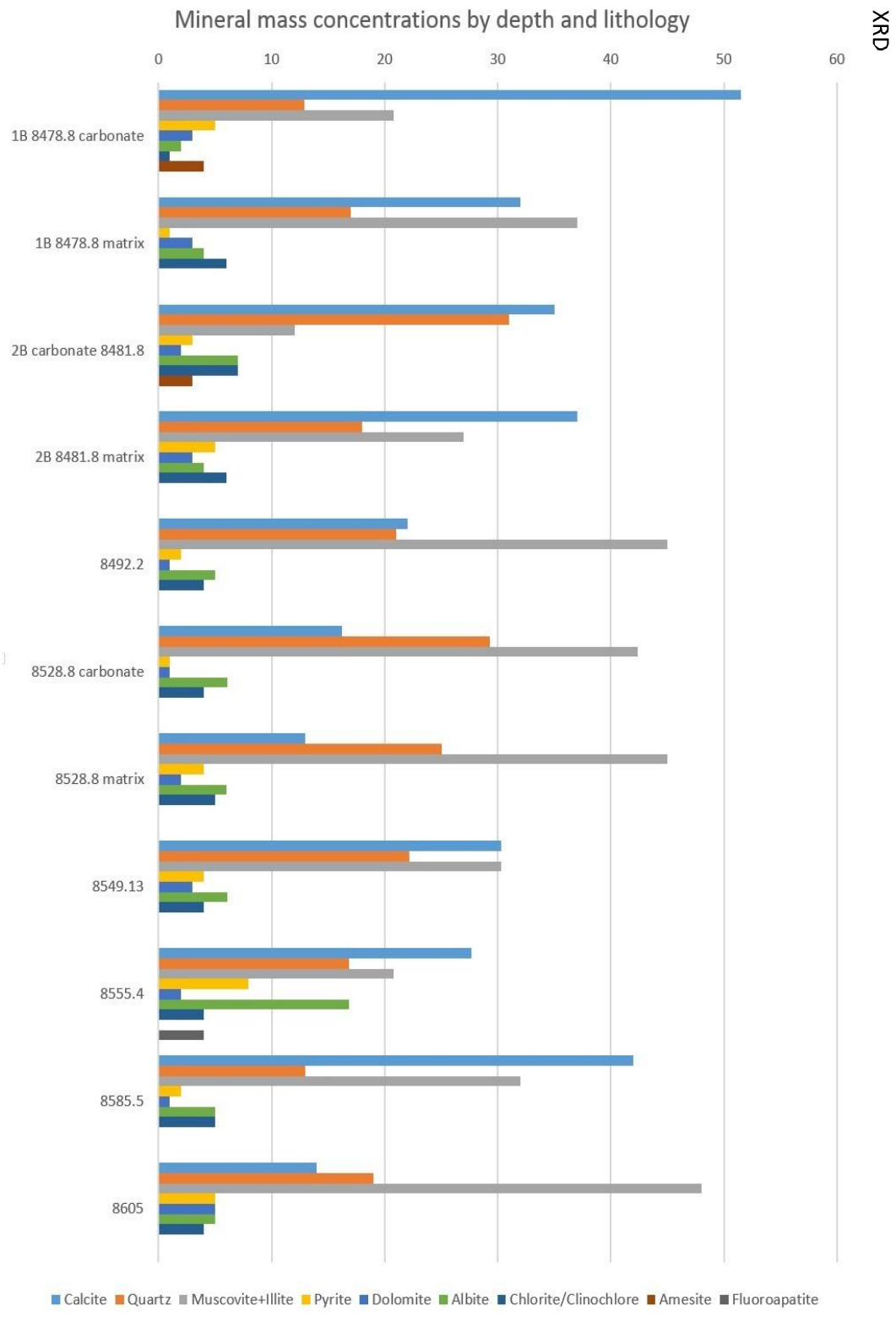

Figure 71- Mineral concentrations by depth

Figure 72: Raw TOC data

	mass (g)			depth					signal	area	
STANDARD	0.537	Sample	acetanilide 1		48		N2_CO2 sample.met		6.134		
STANDARD	0.662	Sample	acetanilide 2		49		N2_CO2 sample.met		8.269		
-	0	Sample	tin		0		N2_CO2 sample.met				
-	0	Sample	silver		1		N2_CO2 sample.met				
bad signal	7.192	Sample	1 BC	8478.8	2		N2_CO2 sample.met				
-	2.13	Sample	1 BC	8478.8	3		N2_CO2 sample.met		2.65	84	0.030403
-	8.306	Sample	1 BM	8478.8	4		N2_CO2 sample.met		6.327	310	0.04109
bad signal	2.085	Sample	1 BM	8478.8	5		N2_CO2 sample.met				
-	7.51	Sample	2 BC	8481.9	6		N2_CO2 sample.met		2.086	69	0.006179
bad signal	2.325	Sample	2 BC	8481.9	7		N2_CO2 sample.met				
-	7.826	Sample	2 BM	8481.9	8		N2_CO2 sample.met		3.578	111	0.012496
bad signal	2.087	Sample	2 BM	8481.9	9		N2_CO2 sample.met				
-	9.159	Sample	8 BC	8549.13	10		N2_CO2 sample.met		5.909	75	0.005868
bad signal	2.049	Sample	8 BC	8549.13	11		N2_CO2 sample.met				
-	7.234	Sample	8 BM	8549.13	12		N2_CO2 sample.met		5.453	164	0.022484
bad signal	1.983	Sample	8 BM	8549.13	13		N2_CO2 sample.met		1.683		
-	9.043	Sample	9 B	8555.4	14		N2_CO2 sample.met		5.575	67	0.004861
bad signal	2.049	Sample	9 B	8555.4	15		N2_CO2 sample.met				
-	7.239	Sample	11 B	8585.5	16		N2_CO2 sample.met		4.936	152	0.02044
bad signal	2.34	Sample	11 B	8585.5	17		N2_CO2 sample.met	2.223	75	0.022968	2.296804
-	9.174	Sample	8492	8492.2	18		N2_CO2 sample.met		7.324	221	0.025332
bad signal	2.054	Sample	8492	8492.2	19		N2_CO2 sample.met		1.696		
-	7.811	Sample	8528	8528.8	20		N2_CO2 sample.met		8.539	264	0.036488
bad signal	2.628	Sample	8528	8528.8	21		N2_CO2 sample.met				
bad prep	9.18	Sample	8605	8605	22		N2_CO2 sample.met				
bad prep	2.464	Sample	8605	8605	23		N2_CO2 sample.met				
-	7.862	Sample		8605	24		N2_CO2 sample.met		8.243	256	0.035006
bad signal	2.22	Sample		8605	25		N2_CO2 sample.met	2.555	86	0.030273	3.027255
-	1.346	Sample	HOCC C3		26		N2_CO2 sample.met		4.744		
STANDARD	0.729	Sample	ACET		27		N2_CO2 sample.met		11.384		
STANDARD	0.553	Sample	ACET		28		N2_CO2 sample.met		15.6		
STANDARD	0.489	Sample	ACET		29		N2_CO2 sample.met		10.329		
STANDARD	0.193	Sample	ACET		30		N2_CO2 sample.met		4.647		
STANDARD	0.666	Sample	ATROPINE		31		N2_CO2 sample.met		16.968		

Continued

TOC raw data

Figure 72: Continued

		TOC %	
307	0.046945	4.694463	
		3.040273	
		4.109038	
151	0.070379	7.037917	
		0.617889	
333	0.158899	15.88989	
		1.249625	
359	0.192264	19.22636	
		0.586802	
394	0.216731	21.67306	
		2.248378	
59	0.01723	1.723007	
		0.48608	
432	0.239423	23.94235	
		2.043987	
		2.533183	
60	0.01723	1.723021	
		3.648829	
2.955	98	0.03116	3.116002
9.739	488	0.060904	6.090432
9.952	492	0.228895	22.88945
		3.500649	